学位論文

Development of a Frequency Modulation Observing Method for Millimeter and Submillimeter Wave Spectroscopy Based on Correlated Noise Removal

（相関雑音除去に基づくミリ波サブミリ波
分光のための周波数変調観測手法の開発）

平成 29 年 12 月　博士（理学）申請

東京大学大学院　理学系研究科

天文学専攻

谷口　暁星

Development of a Frequency Modulation Observing Method for Millimeter and Submillimeter Wave Spectroscopy Based on Correlated Noise Removal

Abstract

Revealing the star formation history of the universe is one of the main goals of astronomy. Molecular and atomic line emissions at (sub-)millimeter wavelength are the unique probes to know both distance and star formation rate of galaxies, and it is now important to offer efficient and sensitive spectroscopic observations in large single-dish telescopes and develop such techniques. However conventional observing methods such as position switching (PSW) or frequency switching (FSW) methods need to obtain reference spectra in order to cancel emission from Earth's atmosphere and other instrumental components, which causes not only additional noises and baseline ripples onto a spectrum but also drops the efficiency of observation, and finally prevents us from detecting such faint and broad spectra.

In this thesis, we propose and develop a new observing method for (sub-)millimeter spectroscopy with a frequency-modulating local oscillator (FMLO). It is an application of the observing method of a multi-pixel continuum camera for a radio telescope: We focus on the behavior of background emission that they are fluctuated slowly ($\lesssim$1 Hz) in time and correlated in frequency (correlated noises). The FMLO method obtains time series spectra (timestream) of a target (ON-point) at a sampling rate of 10 Hz. Meanwhile astronomical signals are frequency-modulated (FM), which is realized by changing the frequency of local oscillator (LO) of a heterodyne receiver one after another. Since astronomical signals are now modulated at high time frequcy of 10 Hz in a timestream, only correlated noises are in-situ estimated and then removed from the timestream by principal component analysis (PCA) without obtaining reference spectra (OFF-point).

The objective of this thesis is to achieve a new spectroscopy based on correlated noise removal for high observation efficiency and less baseline repples realized by in-situ estimation of OFF-point without observing it, and thus develop a new method of timestream-based observation (FMLO method) to which correlated noise removal is applicable. First of all, we show that we can introduce the concept of correlated noise removal into spectroscopy with the FMLO method by mathmatical expressions (chapter 1–2). We describe minimum requisites for an implementation of the FMLO system, and actual implementation and commissioning it at Nobeyama 45 m and ASTE 10 m telescopes (chapter 3). Then we develop signal processing of the FMLO method (chapter 4). We express the observation equations of the FMLO method, and propose a signal processing to estimate and correct for gain (bandpass) depending on changing LO frequnecy (FM gain). We also propose a new correlated component removal method under strong and broader spectral line emission of the atmosphere such as ozone molecule. We introduce weighted PCA realized by the EMPCA, whose iterative steps take account of deweighting of atmospheric line existing elements over a timestream.

After the principle and signal processing of the FMLO method are established, we conduct on-site commissioning of the FMLO method at Nobeyama 45 m and ASTE 10 m to verify the FMLO system and signal processing (chapter 5–6). We demonstrate for the first time that correlated noises exist in a timestream data of an FMLO observation, and they are in-situ estimated and then subtracted with correlated noise removal realized by PCA and the EMPCA. This achieves obtaining a spectrum with no OFF-point observaions and thus high observation efficiency of $\eta_{\mathrm{obs}} = 0.92$ in an FMLO observation of a spectral line. We verify the consistency between a spectrum of PSW method and one observed from FMLO method and then reduced with the signal processing, by simulation of observation and reduction with an artificial spectral line model embedded to timestream of blank sky. We demonstrate that Gaussian and rectangular models with several line widths and intensities are reproduced by simulations with the best frequency modulation pattern (FMP). We simultaneously obtain the guide for an optimal FMPs that the total FM width of an FMP should be wider than the line FWHM

width. We also demonstrate that the obtained spectra of several astronomical target with FMLO and PSW or OTF mapping are consistent with each other with using an optimal FMP selected according to that guide. Compared to conventional PSW method on a spectral line observation, we demonstrate that the achieved sensitivity of the FMLO method per unit total observation time is $\sim$1.7 times better than that of PSW. In other words, the achieved efficiency per unit noise level is ~ 3 times better. Also compared to conventional OTF method on a mapping observation, we demonstrate that the achieved sensitivity of the FMLO method per unit total observation time is $\sim$1.1 times better than that of PSW, in other words, the achieved efficiency per unit noise level is ~ 1.2 times better. Although, we consider these values as lower limit because we find that there exists noise contribution from correlated component removal itself as a factor of $\alpha \simeq 1.1$.

Finally we discuss all the results derived in the commissioning and future prospects (chapter 7). As a part of the discussion, we mention the possibility of reducing the noise contribution factor α by smoothing of correlated components in iterative steps of the EMPCA.

Contents

Listing of figures

ix

xi

Listing of tables

To my family and my wife.

Acknowledgments

I would like to express my gratitude to everyone who helped me in my research life as a Ph.D student in the University of Tokyo. First of all, I am deeply grateful to Kotaro Kohno, my supervisor. Actually I became interested in radio astronomy with his observation practice at the Nobeyama when I was an undergraduate student. With his wide-ranging study topics with great knowledge, he let me do exciting studies in both scientific and development fields. I would like to express the deepest appreciation to Yoichi Tamura, the principal investigator of the FMLO. He really knows the importance of studying both science and development, and has lots of ideas about them. I have learned lots of statistical analyses of time-series data from him. He generously shared a large amount of time to discuss various issues related to the signal processing methods in this thesis.

I would particularly like to thank the members of Kohno laboratory in the University of Tokyo: Bunyo Hatsukade, Tatsuya Takekoshi, Hideki Umehata, Yuri Nishimura, Tao Wang, Takuma Izumi, Yuki Yamaguchi, Ryo Ando, Tsuyoshi Ishida, Yui Yamashita, Chen-Feng Lee, Yuki Yoshimura, Shotaro Kikuchihara, Seiji Fujimoto, Shun Ishii, Ryu Makiya, Soh Ikarashi, Kenta Suzuki. I would like to thank the members of the Institute of Astronomy, the University of Tokyo: Kazuma Mitsuda, Masaki Yamaguchi, Masahito Uchiyama, Jian Jiang. I also would like to thank my classmates in the Mitaka campus: Yuta Kato, Minju Lee, Masafusa Onoue, Yutaka Hirai, Haruka Baba, Tsuguru Ryu. They always gave me fruitful comments from view points of their wide and various scientific fields in the laboratory meetings, the institute's coffee time, and daily campus life. I would like to thank the members of Astronomy Laboratory in Nagoya University: Koyo Suzuki, Yuki Urata, Tetsutaro Ueda, Yuya Shimada. Discussing with them was interesting and also their local guide around the university was great helpful to me when I visitied the laboratory.

I have received generous support from Nobeyama and ASTE staffs when

Beautiful is better than ugly.
Explicit is better than implicit.

From the Zen of Python, by Tim Peters

1

Introduction

1.1 Spectrocopy in (sub-)millimeter astronomy

1.1.1 Scientific overview

Revealing how galaxies are formed and evolved over the cosmic history is one of the most important issues in modern astronomy. It is also essential to investigate how nuclear activities in extra galaxies such as active galactic nuclei (AGNs) and starburst (SBs) affect onto host galaxies in terms of galaxy evolution at various ages of the universe. Millimeter and submillimeter wavelengths have an unique and important role in the observation of cold interstellar medium (ISM), which is the reservoir of fuel for AGN as well as the site of star formation: For example, various kinds of emission from different physical processes related to ISM are available at that wavelength such as thermal emission from dust, synchrotron emission from high energy electrons (continuum emission), and rotational and vibrational transition of molecules and recombination of atoms (spectral line emission). Such emission is a unique diagnostic tool for physical and/or chemical conditions of ISM and surrounding environment because different environment has different physical and/or chemical impact onto ISM. Investigating molecular or atomic

gas composition in ISM at (sub-)millimeter wavelength is therefore essential for deriving information on what drives galaxy evolution. Besides (sub-)millimeter wavelengths are suitable to investigate star formation activity obscured by dust. Optical and infrared observations cannot detect such activity properly because of large extinction by dust at that wavelengths.

Recent remarkable progress of radio observation techniques has been revealing galaxy evolution at (sub-)millimeter wavelength, in particular, the finding of submillimeter galaxies (SMGs; Blain et al. (2002)) which are gas-rich star forming galaxies powered by high star formation rate of $\sim 10^3 \mathrm{M}_\odot/\mathrm{yr}$ located at $z = 2 - 3$, the most intense peak of star formation history of the Universe. The number of SMGs ever found has been drastically increased by wide field deep surveys using continuum multi-pixel camera: For example, more than 1000 SMGs were detected in a survey using a 144-pixel bolometer camera, AzTEC (Scott et al., 2012), mounted on the ASTE 10 m. Spectroscopic observations of molecular or atomic line emission of such SMGs are then necessary to know both distances (spectroscopic redshift) and star formation rates, but they are in general difficult to detect because such emission lines are broader (several hundred km/s FWHM) and very faint (peak flux density of $\lesssim 10$ mJy) (Iono et al., 2012). Recent interferometric observations with ALMA has been detecting such line with unprecedented sensitivity (e.g., Vieira et al. (2013)). On the other hand, even ALMA would take huge time to conduct observations of blind redshift search* towards the enomous number of SMGs to determine their redshift, which is not always an effective way. Now it is important to observe them with large single dish telescopes: If an efficient and high sensitivity spectroscopic observation is available with such telescopes, we can construct a large catalogue of SMGs with known spectroscopic redshifts before ALMA observations. An efficient spectroscopy in single dish telescopes is also important in ALMA itself because ALMA uses four single dish antenna (ACA Total Power Array) for the improvement of fidelity of interferometric images. It is therefore one of the issues in (sub-)millimeter astronomy to offer efficient and sensitive spectroscopic observations in large single dish telescopes and develop such

---

*it requires several observations toward an object with changing observing frequencies to search a line until it is detected

techniques.

1.1.2 Instruments of heterodyne receiver

Here we briefly review the instruments and obserbing methods of spectroscopy in (sub-)millimeter single dish telescope. We hereafter express intensity, I_ν (in units of W m^{-2} Hz^{-1} sr^{-1}), as temperature because Rayleigh-Jeans approximation of a black body is realized at (sub-)millimeter wavelength. Given a wavelength or frequency, expression of intensity in temperature, $T_{\rm b}$, is as follows:

$$T_{\rm b} \equiv \frac{\lambda^2}{2k_{\rm B}} I_\nu = \frac{c^2}{2k_{\rm B}\nu^2} I_\nu \qquad (1.1)$$

where $k_{\rm B}$ is Boltzmann constant, c is speed of light in vacuum.

A (sub-)millimeter observation from an astronomical target is to measure an intensity of electromagnetic wave, and a role of a receiver used for such observation is to convert very faint astronomical signal at high frequency to regular electric signal at lower frequecy (easy to handle). First of all, there are roughly two techniques available for (sub-)millimter instruments:

Coherent receivers Receivers which use both amplitde and phase information of electromagnetic wave (capturing it as "wave"). A typical one is heterodyne receiver. Such types of receivers are suitable for spectroscopic observation because it achieves high frequency resolution by heterodyning: it mixes astronomical signal at radio frequency (RF) and artificial reference signal generated from a local oscillator (LO) to obtain downconvert signal at intermediate frequency (IF) which is available as an input for a digital spectrometer. In other words, heterodyne receivers convert RF frequency into lower IF one without losing amplitude and phase information.

Incoherent receivers Receivers which use only amplitde information of electromagnetic wave (capturing it as photon or thermal energy). A typical one is bolometer. Although high frequency resolution for spectroscopy is difficult to be achieved, such types of receivers are suitable for continuum wave observation because it achieves wider observed band width and lower receiver
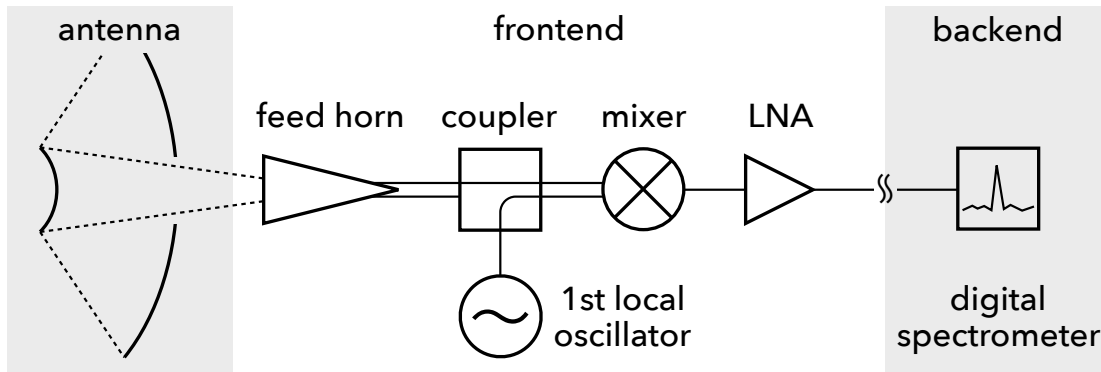
Figure 1.1: Block diagram of a heterodyne receiver (frontend) and a digital spectrometer (backend) for a telescope whose observing frequency of $\gtrsim 100$ GHz.

noise: While a heterodyne receiver has upper limit of obserced band width by IF band width and lower limit of receiver noise temperature due to quantam noise of $h\nu/k_{\mathrm{B}}$, a bolometer has no such limits. Beside it is relatively easy to implement multi-pixel bolometer "camera" (the number of pixel is about $10^2 - 10^4$) because the structure of receiver is simple compared to heterodyne receivers.

We then summarize the instruments used for (sub-)millimeter heterodyne spectroscopic observations of a single dish telescope. Because the intensity of such target is very weak in general ($< 10^{-23}$ W Hz^{-1} even after collecting by an antenna), a strategy of an astronomical observation at (sub-)millimeter wavelength is as follows: (1) collecting electromagnetic wave by a large antenna and introducing it to a waveguide by a feed horn (2) downconverting RF signal to IF one by a coupler and a mixer, (3) amplifying the signal by low-noise amplifier (LNA), and (4) input IF signal to a digital spectrometer to obtain a spectrum[†]. These processes are illustrated in figure 1.1.

[†]this is in the case of $\nu_{\mathrm{obs}} \gtrsim 100$ GHz where a LNA compatible with that frequency is not available. In the case of $\nu_{\mathrm{obs}} \lesssim 100$ GHz, a LNA is placed prior to coupler so that the noise temperature should be suppressed according to equation 1.3

EQUIVALENT NOISE TEMPERATURE AND GAIN

Here we introduce equivalent noise temperature, a quantitative measure of noise from various components, and gain of an amplifier. We suppose an amplifier whose amplification factor of G (gain). If signal is S_input is input to the amplifier, it should yield an output of $S_\text{output} = GS_\text{input} + N$, where N is an additional noise generated within the amplifier. For the convenience, we can rewrite it so that the noise is also an input:

$$S_\text{output} = G(S_\text{input} + N_\text{eq}) = G\left(S_\text{input} + \frac{N}{G}\right) \tag{1.2}$$

where N_eq is a equivalent input noise. The expression of N_eq in temperature is called equivalent input noise temperature, $T_\text{n} = N_\text{eq}/(k_\text{B}\Delta\nu)$, where $\Delta\nu$ is a band width. The equivalent input noise temperature of multiple amplifiers connected in series can be derived by similar deformation above:

$$T_\text{n,total} = \sum_{i=1}^{N} \frac{T_\text{n,i}}{\prod_{j=1}^{i-1} G_j} = T_\text{n,1} + \frac{T_\text{n,2}}{G_1} + \frac{T_\text{n,3}}{G_1 G_2} + \cdots + \frac{T_\text{n,N}}{G_1 G_2 \cdots G_{N-1}} \tag{1.3}$$

where N is the number of amplifiers in a circuit. It suggests that the equivalent input noise temperature of the first amplifier is the most dominant and should be designed to be lower noise temperature. In the case of $\nu_\text{obs} \gtrsim 100$ GHz, the first amplifier corresponds a mixer and its gain is less than unity, which also suggests that the equivalent input noise temperature of the second amplifier (LNA at IF signal) is important. We note that the actual value of such gain is dependent on RF or IF frequency, which will cause gain change in a frequency modulation observation and should be corrected properly. This will be further discussed in chapter 4.

HETERODYNE TECHNIQUE

Here we introduce heterodyne technique and terminology of it. As briefly mentioned above, heterodyne is a signal processing to create a new frequency by mixing

two different frequencies. In (sub-)millimeter spectroscopy, the two different frequencies are RF signal from sky and artificial signal generated by local oscillator (LO), and a new frequency is called intermediate frequency (IF) which is often difference frequency of $|\nu_{\mathrm{RF}} - \nu_{\mathrm{LO}}|$ (downconverting) available as an input for digital spectrometer. Such frequency conversion is conducted by a coupler (combining RF and IF signals) and mixer (mixing RF and IF signals to create IF signal).

The heterodyne technique is based on the following trigonometric identity:

$$\sin(2\pi\nu_1 t)\,\sin(2\pi\nu_2 t) = \frac{1}{2}\cos(2\pi(\nu_1 - \nu_2)t) - \frac{1}{2}\cos(2\pi(\nu_1 + \nu_2)t) \qquad (1.4)$$

where sum and difference frequencies are generated by a product of two signals of different frequencies, ν_1, ν_2. In other hand, if we could process signals including a product operation, we would obtain signals of $\nu_1 + \nu_2$ and/or $\nu_1 - \nu_2$. In (sub-)millimeter spectroscopy, we often use a mixer which has non-linear current-to-voltage $(I - V)$ characteristic to achieve such operation, where V is input voltage of combined signal (RF and LO), and I is output current. For a simple example, if $I - V$ is assumed to be expressed as $I \propto V^{2\ddagger}$ and $\nu_{\mathrm{RF}} > \nu_{\mathrm{LO}}$, the input voltage of RF and LO, and output current are expressed as follows:

$$V_{\mathrm{RF}}(t) = V_{\mathrm{RF},0} \cos(2\pi\nu_{\mathrm{RF}} t + \phi_{\mathrm{RF}}) \qquad (1.5)$$

$$V_{\mathrm{LO}}(t) = V_{\mathrm{LO},0} \cos(2\pi\nu_{\mathrm{LO}} t + \phi_{\mathrm{LO}}) \qquad (1.6)$$

$$\begin{aligned}
I_{\mathrm{output}} &= G\left(V_{\mathrm{RF}}(t) + V_{\mathrm{LO}}(t)\right)^2 \\
&= \frac{1}{2}G(V_{\mathrm{RF},0}^2 + V_{\mathrm{LO},0}^2) \\
&\quad + \frac{1}{2}GV_{\mathrm{RF},0}^2 \cos 2(2\pi\nu_{\mathrm{RF}} t + \phi_{\mathrm{RF}}) \\
&\quad + \frac{1}{2}GV_{\mathrm{LO},0}^2 \cos 2(2\pi\nu_{\mathrm{LO}} t + \phi_{\mathrm{LO}}) \\
&\quad + GV_{\mathrm{RF},0}V_{\mathrm{LO},0} \cos\left(2\pi(\nu_{\mathrm{RF}} + \nu_{\mathrm{LO}})t + (\phi_{\mathrm{RF}} + \phi_{\mathrm{LO}})\right) \\
&\quad + GV_{\mathrm{RF},0}V_{\mathrm{LO},0} \cos\left(2\pi(\nu_{\mathrm{RF}} - \nu_{\mathrm{LO}})t + (\phi_{\mathrm{RF}} - \phi_{\mathrm{LO}})\right) \qquad (1.7)
\end{aligned}$$

where G is gain, $V_{\mathrm{RF},0}$, $V_{\mathrm{LO},0}$ are constant voltages of RF and LO signals at $t = 0$,

---

$\ddagger$such 2nd-order characteristic is common as a result of Taylor expansion of non-linear function

Figure 1.2: Schematic diagram of sidebands in a heterodyne receiver. Once observer configures an LO frequency, then IF frequency is generated like a bottom number line. If observable IF ranges are represented as lightblue and orange boxes, they are called lower sideband (LSB) and upper sideband (USB). Observable IF ranges are constrained by frequency response of a mixer, LNA for IF signal, and also specifications of a spectrometer. The blue and red spike represents spectral lines located at that observed frequencies. The ones of light color represents lines contaminated from each image sideband.

ϕ_{RF}, ϕ_{LO} are phases of RF and LO signals. The last two terms are the signals of sum and difference frequenies, respectively. It is also important that phase information is also preserved as $\phi_{RF} \pm \phi_{LO}$. Because the last term in equation 1.7 is of our interest, other terms (constant or much higher frequency terms) are filtered. In (sub-)millimeter spectroscopy of $\nu_{\mathrm{obs}} \gtrsim 100$ GHz, we often use superconductor-insulator-superconductor (SIS) mixer as a good low noise mixer. The receivers we use in this thesis are all operating with a SIS mixer.

SIDEBANDS

The equation 1.7 assumes $\nu_{\mathrm{RF}} > \nu_{\mathrm{LO}}$, but we can also consider a condition of $\nu_{\mathrm{RF}} < \nu_{\mathrm{LO}}$. In this case, the last term of equation 1.7 is as follows:

$$GV_{\mathrm{RF},0}V_{\mathrm{LO},0} \cos\left(2\pi|\nu_{\mathrm{RF}} - \nu_{\mathrm{LO}}|t - (\phi_{\mathrm{RF}} - \phi_{\mathrm{LO}})\right) \tag{1.8}$$

This means that RF frequency of $\nu_{\mathrm{RF}} = \nu_{\mathrm{LO}} - \nu_{\mathrm{IF}}$ can also be included in the output current with its phase different by π radian. In fact the obtained IF signal

7
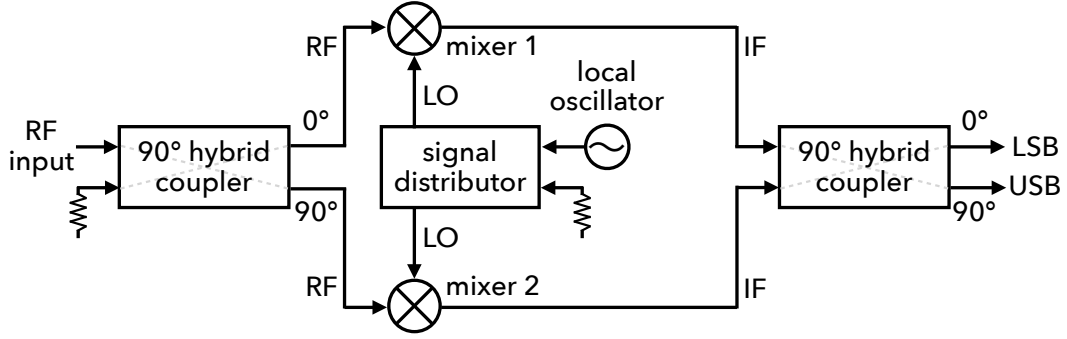
Figure 1.3: Block diagram of a 2SB mixer taken from Nakai et al. (2009) (with some modification by author).

is superposition of two different RF signal:

$$\nu_{RF} = \nu_{LO} \pm \nu_{IF} \tag{1.9}$$

where $\nu_{RF} = \nu_{LO} + \nu_{IF}$ is called upper sideband (USB), and $\nu_{RF} = \nu_{LO} - \nu_{IF}$ is called lower sideband (LSB). This is illustrated in figure 1.2. We also usually call a sideband of interest signal signal sideband, and the others image sideband (for example, if some astronomical spectral line falls in USB, signal sideband is USB and image sideband is LSB). In (sub-)millimeter spectroscopy of $\nu_{obs} \gtrsim 100$ GHz, selecting signal from only signal sideband (sideband separation) is recommended because large power of atmosphric continuum or line emission from image sideband adds noise temperature (noise lebel gets worse).

A mixer which has sensitivity to both USB and LSB but cannot separate two sidebands is called double sideband (DSB) mixer, which is suitable for continuum observation (observed band width is doubled) but not suitable for spectral line observation because of the reason above. On the other hand, a mixer which has sensitivity to both USB and LSB, and is able to separate two sidebands is called two sideband (2SB) mixer. The schematic diagram of the principle of 2SB mixer is illustrated in figure 1.3. Because the phases of USB and LSB are different by π radian, RF signal is split into two path, one of which are phase-shifted by $\pi/2$ radian. Then two signal are separately mixed with LO signal in different

mixers, and phase-shifted signal is again phase-shifted by $\pi/2$ radian. These operations create two IF signals whose USB and LSB are shifted by π radian each other. Finally sum (or subtraction) of two signals yields single USB (or LSB) IF signal. The receivers we use in this thesis are all operating with 2SB mixer.

In actual 2SB mixer, there exists, however, some amount of contamination from image sideband to signal one. As a quantitative measure, we usually use image rejection ratio (IRR) which is a reciprocal of contamination ratio in units of dB[§]. In (sub-)millimeter spectroscopy of $\nu_{\rm obs} \gtrsim 100$ GHz, more than 10 dB of IRR is often required and achieved.

1.1.3 Observations of heterodyne receiver

So far we overview how a astronomical signal are collected, frequency-converted, ampified, and sideband-separated to an IF signal available as an input for digital spectrometer. This, however, includes signals or noises other than astronomical one such as cosmic microwave background (CMB; 2.73 K), atmospheric continuum and/or line emission, noise of receiver and room temperatures[¶]. It also includes several gains which not only amplify a signal but also convert phycical unit (I-to-V, for example). In order to obtain actual temperature of astronomical signal outside the Earth's atmosphere, (exoatmospheric antenna temperature; $T_{\rm A}^*$), we need to calibrate an obtained spectrum to temperature scale and subtract unwanted components with some observing method.

Calibration method

The calibration of a spectrum can be achieved to measure noise sources other than the astronomical signal in order to solve observation equations described below. As one of the most common calibration method, we introduce chopper wheel calibration method (Penzias et al. (1973); also called as R-SKY method or one-load calibration), which is used for all calibration in the following chapters. This

---

[§]If a spectral line of image sideband whose intrinsic peak intensity is 10 K, is detected in signal sideband with intensity of 0.1 K, then the IRR of the receiver is 20 dB

[¶]these noises are observed as (almost) constant offset in a spectrum

method uses two noise sources; (1) a chopper wheel made of black body (absorber) placed in a telescope ($T = T_{\mathrm{room}}$; because its temperature is assumed to be room temperature), and (2) sky itself where no astronomical signal exists ($T = T_{\mathrm{atm}}$), and assumes $T_{\mathrm{room}} = T_{\mathrm{atm}}$. An observation equation is an equation which connects an observable (i.e., spectrum) to unknown variables. Those of astronomical signal (ON-point, hereafter), sky, and chopper wheel (Room, hereafter) are expressed as follows:

$$P_\nu(\mathrm{ON}) = Gk_{\mathrm{B}} \left\{ \eta \left[T_{\mathrm{A}}^* e^{-\tau} + T_{\mathrm{atm}}(1 - e^{-\tau}) \right] + (1 - \eta)T_{\mathrm{room}} + T_{\mathrm{RX}} \right\} \qquad (1.10)$$

$$P_\nu(\mathrm{Sky}) = Gk_{\mathrm{B}} \left\{ \eta \left[0 + T_{\mathrm{atm}}(1 - e^{-\tau}) \right] + (1 - \eta)T_{\mathrm{room}} + T_{\mathrm{RX}} \right\} \qquad (1.11)$$

$$P_\nu(\mathrm{Room}) = Gk_{\mathrm{B}} \left(T_{\mathrm{room}} + T_{\mathrm{RX}} \right) \qquad (1.12)$$

where P_ν ($\propto$ power) are obtained spectrum of each measurement, G is gain, k_{B} is Boltzmann constant, τ is opacity of the atmosphere at the observed wavelength, η is rear spillover, blockage, scattering and ohmic efficiency, and T_{RX} is receiver noise tempereature. We note that we assume the observed zenith angle, Z, is zero. In the case of $Z \neq 0$, the term of τ is corrected as $\tau \sec Z$. We also note that P_ν is as a function of observed frequency, ν, and is actually D-length vector, where D is the number of spectrometer's channels. Although there exist several unknown variables, the following operation with an assumption of $T_{\mathrm{room}} = T_{\mathrm{atm}}$ finally yields T_{A}^*:

$$T_{\mathrm{atm}} \cdot \frac{P_\nu(\mathrm{ON}) - P_\nu(\mathrm{Sky})}{P_\nu(\mathrm{Room}) - P_\nu(\mathrm{Sky})} \simeq T_{\mathrm{A}}^* \qquad (1.13)$$

The advantages of chopper wheel calibration is obviously simple (just measureing two additional sources) but good precision (only 10% of error if $Z \simeq 0$ and $|T_{\mathrm{room}} - T_{\mathrm{atm}}| < 20$ K). We also derive a system noise temperature (T_{sys}; exoatmospheric noise temperature which should be compared to T_{A}^* when discussing signal-to-noise, for example) using these measurements. A system noise temperature is sum of noise contributions from the atmosphere and telescope, which is derived by converting $P_\nu(\mathrm{Sky})$ to one outside the Earth's atmosphere:

$$T_{\mathrm{sys}} \equiv \frac{P_\nu(\mathrm{Sky})e^\tau}{Gk_{\mathrm{B}}\eta} \qquad (1.14)$$
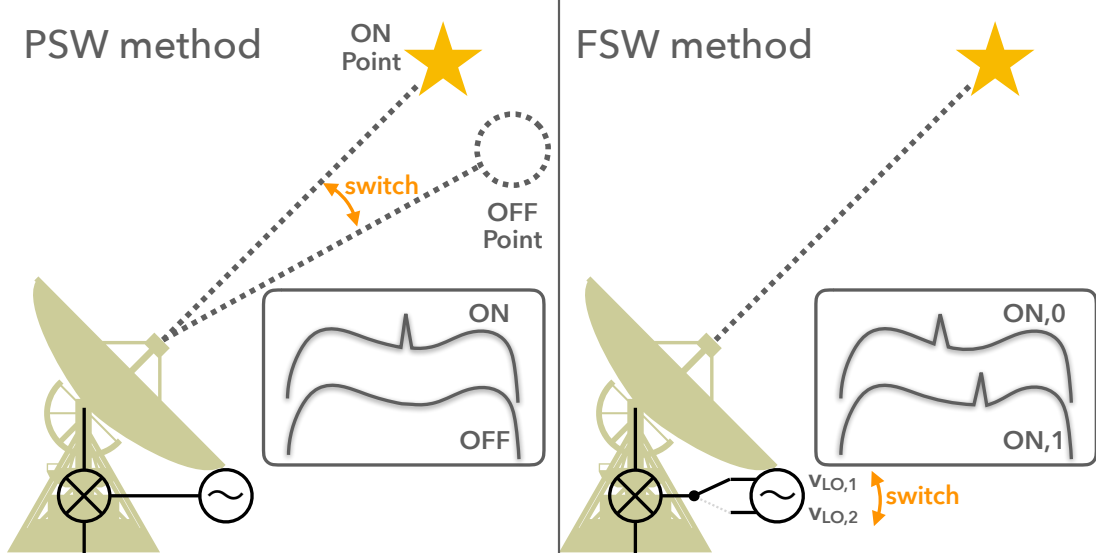
Figure 1.4: Schematic diagram of two switching observing methods. (left) position switching (PSW) method. Observer should switch telescope position between ON and OFF points by turns. (right) frequency switching (FSW) method. Unlike PSW, observer should switch LO frequency between $\nu_{\mathrm{LO},1}$ and $\nu_{\mathrm{LO},2}$ by turns.

Using equation 1.11 and 1.12, this can be expressed as follows:

$$T_{\mathrm{sys}} = \frac{T_{\mathrm{room}}}{P_\nu(\mathrm{room})/P_\nu(\mathrm{Sky}) - 1} = \frac{T_{\mathrm{room}}}{10^{Y/10} - 1} \tag{1.15}$$

where $Y \equiv 10 \log_{10}\left[P_\nu(\mathrm{room})/P_\nu(\mathrm{Sky})\right]$ is often called Y-factor, which is an indicator of observation condition (higher Y indicates less noisy observation).

OBSERVING METHODS

As we overview above, it is necessary to obtain a reference spectrum without astronomical signal in order to derive T_{A}^*. Here we introduce conventional (and still active in most spectroscopic observations) observing methods (Wilson et al., 2012) so called switching ones.

The most commonly used observing method in the world is position switching method (PSW, hereafter), with which an observer obtains spectra of ON-point and the position of no astronomical signal (OFF-point, hereafter) by turns in order

to cancel emission from Earth's atmosphere and other instrumental components. This is illustrated in figure 1.4. Because the observation equation of OFF-point can be expressed as same as the sky, the calibration by chopper wheel method is as follows:

$$T_\mathrm{A}^* = T_\mathrm{atm} \cdot \frac{P_\nu(\mathrm{ON}) - P_\nu(\mathrm{OFF})}{P_\nu(\mathrm{Room}) - P_\nu(\mathrm{Sky})} \qquad (1.16)$$

The advantage of PSW method is that it is simple like chopper wheel calibration and applicable to almost all spectral line observations. On the other hand, obtaining OFF-point spectra always decreases ratio of ON-point observing time over a total observation time (observation efficiency): Conventionally ON and OFF-point observing times should be same, which yields upper limit of observation efficiency of only 50 %. In an actual observation, it is often less than 50 % because of additional overhead time such as telescope slewing time between ON and OFF-positions (this is remarkable in a large telescope).

The other common observing method is frequency switching method (FSW, hereafter), with which an observer obtains only ON-point but with two different center observing frequencies by turns in order to cancel continuum emission from Earth's atmosphere and other instrumental components. The ON-ON′ spectrum contain the same spectral line in two different position and one's sign is inverted, then observer fold the spectrum so that two position is overlapped in a post data reduction to obtain a final spectrum. This is illustrated in figure 1.4. Switching observing frequency can be achieved by changing LO frequency: It is easy to change the frequency if LO signal is generated by a digital signal generator which can be controlled by some programable commands. The advantage of FSW methods is that high observation efficiency is expected because both two different spectra contain line emission (almost 100 % of observation efficiency) and switching between two LO frequency is often operated electrically, which causes almost no additional overheads. On the other hand, baseline fluctuation (ripples) at line-free regions are more likely to be ocuured compared to PSW method because FSW method operates the subtraction of spectra obtained different observed frequency. For the same reason, an observation of broader spectral line observation is difficult because at least wider LO frequency interval than the FWZI (full width at zero

intensity) of a line is required in the subtraction and folding operations. As an improvement of FSW method, it has been recently proposed to obtain spectra with more than two LO frequencies and then directly solve and correct for IF-dependent gain (bandpass shape of a spectrometer) by least-squares fitting (Least-Squares Frequency Switch; LSFS; Heiles (2007)). LSFS is used for a spectroscopy of lower frequency (centimeter wavelength). This approach directly solves the RF spectrum without subtracting different spectra each other, however, it assumes that RF spectrum does not change during several observations, which is not the case with (sub-)millimeter spectroscopy because atmospheric emission is much more dominant than the astronomical signal and variable.

1.2 Correlated noise and their removal

Improving sensitivity of a telescope system is always an important issue in modern observational astronomy. There are many factors which limit the sensitivity of spectroscopic observations with single-dish radio telescopes, while they are not fully explored for sensitivity improvements. The root-mean-square noise level of single-dish spectroscopic observations is expressed as

$$\Delta S = \frac{\sqrt{2}k_{\mathrm{B}}T_{\mathrm{sys}}}{A\eta_{\mathrm{ap}}\sqrt{N_{\mathrm{pix}}\Delta\nu t_{\mathrm{total}}\eta_{\mathrm{obs}}}} \tag{1.17}$$

where k_{B}, T_{sys}, A, η_{ap}, N_{pix}, $\Delta\nu$, t_{total}, and η_{obs} are the Boltzmann constant, system noise temperature, collecting are and aperture efficiency of a primary mirror, number of feeds, band width, total observing time including any overheads, and observation efficiency defined by the fraction of on-source time in the total observing time, $\eta_{\mathrm{obs}} = t_{\mathrm{on}}/t_{\mathrm{total}}$. Generally speaking, improving a system noise temperature T_{sys} and the effective collecting area $A\eta_{\mathrm{ap}}$ of a primary mirror, as well as increasing the number of feeds N_{pix}, require tremendous effort and huge resources. As we overview in the previous section, the issues of observing methods such as OFF-point measurements, large overheads, baseline ripples and other noises and gain fluctuations can also be a source of decreasing effective on-source time, or η_{obs}.

1.2.1 Limitation of conventional switching methods

The conventional methods of PSW and FSW are still widely used in present spectroscopic observations in (sub-)millimeter astronomy. Such switching methods are, however, necessary to estimate and correct for bandpass gain and sky levels based on a comparison of reference spectrum with a major assumption that the condition of telescope (i.e., G or T_{RX}) and atmosphere (i.e., τ) is not variable (or variable is small enough) in time interval (between ON and OFF) or frequency shift (ON and ON$'$ of another freuqency). Observing efficiency offered by PSW methods is therefore not so high ($0.1 \lesssim \eta_{\mathrm{obs}} < 0.5$) because of a need for taking OFF-point spectra and telescope slewing time. Furthermore, subtraction of the OFF-point/frequency spectra is virtually equivalent to addition of noises to the signal spectra, which is why the factor of $\sqrt{2}$ is multiplied to the right side in equation 1.17. A noble method which uses a smoothed OFF-point bandpass (Yamaki et al., 2012) in order to reduce the noises added in the subtraction is a good compromise, although it still needs OFF-point measurements.

Another issue which degrades the observation efficiency is a spectral baseline fluctuation across emission-free channels. The incident sky emission is generally time-variable in the (sub-)millimeter because water vapor emission dominates the flux from the sky. When the switching period between on and OFF positions/frequencies are longer than the typical time-scale of sky variations, unbalance between on- and OFF-point spectra can cause baseline fluctuations in the resulting spectra, because the conventional chopper wheel method does not deal with *in-situ* estimation of bandpass gains and sky levels.

1.2.2 Correlated noise removal in multi-pixel camera

In contrast, there is a method achieving a high efficiency ($\eta_{\mathrm{obs}} \approx 0.9 - 1$), which never needs OFF-point measurements and has been extensively employed in recent deep extragalactic surveys and cosmic microwave background (CMB) experiments on the basis of ground-based facilities using multi-pixel bolometer cameras. The output of a ground-based telescope is always dominated by large atmospheric emission. If a receiver has array detectors (e.g., a multibeam receiver or a spec-
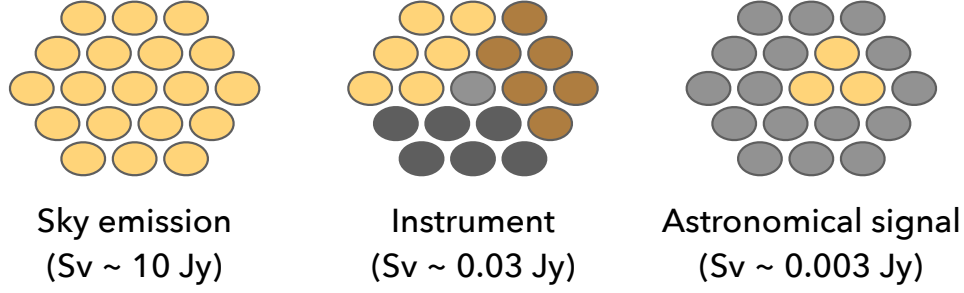
Figure 1.5: Schematic diagram of the concept of correlated noises over a multi-pixel camera. Each oval represents pixel detector of the camera, and color represents strength of input signal (brighter one indicates stronger signal value). (left) most dominating correlated noises from the sky (Earth's atmosphere). (center) correlated noises attributed to readout of local sub-regions. (right) an astronomical signal (expected to be localized, i.e., not correlated).

trometer), the output time-series data (timestream, hereafter) from the detectors are mutually correlated, because the detectors see almost the same part of the troposphere (~ 1 km above the ground). Because these *correlated noises* are known to behave as $1/f$-type noises and have large power at low frequencies ($\lesssim 10$ Hz) in timestream, filtering out the correlate modes of timestream which are common among multiple detector outputs with, for example, principal component analysis (PCA) can estimate *in-situ* and remove the awkward low frequency noises induced mainly by the atmosphere (Laurent et al. (2005), Scott et al. (2008); see also figure 1.5 and 1.6).

It is also important to modulate the astronomical signals involved in timestream into higher frequency domain so as not to filter out the astronomical signals of interest (Kovács, Attila, 2008). In the continuum deep surveys and CMB experiments, this modulation is achieved by fast moving the telescope pointing across the sky.

1.2.3 CORRELATED NOISE REMOVAL IN SPECTROSCOPY

Here we aim to introduce the concept of correlated noises and their removal into (sub-)millimeter spectroscopy and propose a new observing method for *in-situ* esti-
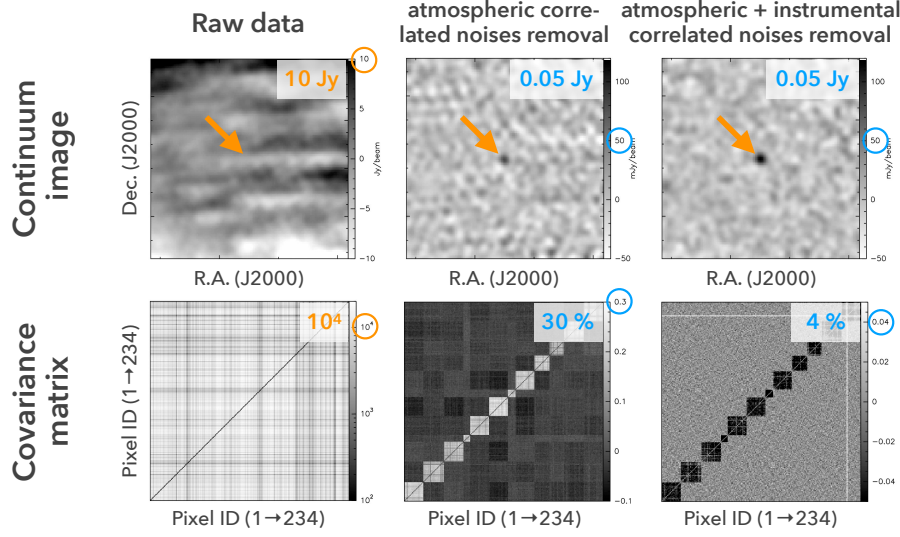
Figure 1.6: An example of correlated noise removal in a multi-pixel camera of LABOCA (Kovács, Attila, 2008). (top) three image of raw data, the one after removing atmospheric correlated noises, and the one after removing atmospheric and instrumental correlated noises (from left to right). As the correlated noise removal proceeds, only white noise and a point source (100 mJy; simulated one) is clearly detected. (bottom) three covariance matrices derived from time-series data which make corresponding images. The horizontal and vertical axes are both pixel ID. As the correlated noise removal proceeds, only diagonal self-correlations remain, and cross-correlation is removed.

mation of bandpass gains and sky levels. If one considers the one-to-one relations between multibeam (i.e., bolometer camera) imaging observations and spectroscopic one:

$$\text{detectors of a camera} \rightarrow \text{channels of a spectrometer}$$
$$\text{moving the pointing} \rightarrow \text{sweeping the frequency}$$

then this noise removal technique can be applicable to spectroscopic observations (Kovács, Attila, 2008, Tamura et al., 2013). The relationship is also summarized in figure 1.7 with schematic diagrams of observation. In other words, correlated noises removal without observing OFF-point can be introduced to (sub-)millimeter spectroscopy if we obtain a time-series spectra (a timestream) of ON-point with its observed frequency modulated at a sampling rate of $\gtrsim 10$ Hz in order to capture
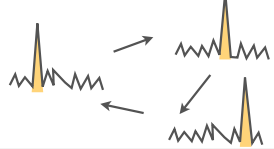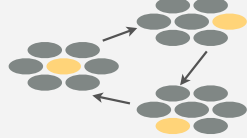
	Elements	How to modulate	Schematic diagram
FMLO	channels of spectrometer (D ~ 10³)	LO frequency (1D motion)	
Multi-pixel Camera	detectors of camera (D = 10² - 10⁴)	FoV of telescope (2D motion)	

Figure 1.7: Illustrative table for a comparison of two different methods of FMLO and multi-pixel camera. Although receiver type and its operation principle of them is totally different, correlated noise removal technique is used in common. The major difference is dimension of modulation: While FMLO is 1-dimension modulation along with frequency, that of camera is 2-demension modulation over celestial coorinates.

$1/f$-like noise behavior of the sky and estimate and remove them by PCA. As illustrated in figure 1.8, this new observing method of totally different operation principle is no longer switching one but frequecy "modulation" (FM) method, and modulation of observing frequency can be achieved with a heterodyne receiver by fast frequency sweeping of digital signal generator which generates local oscillator (LO) signal. We therefore call our proposed method a *Frequecy-Modulating Local Oscillator (FMLO)* method.

The expexted advantages of the FMLO method are (1) high observation efficiency of $\eta_{\mathrm{obs}} \gtrsim 0.9$ because of no OFF-point observation, (2) reducing of baseline ripple because of in-situ OFF-point estimation by PCA, (3) sideband separation in a offline data reduction, and (4) low cost implementation because existing instruments are likely to be available for the FMLO method. The detailed principle, and minimum requisites for a telescope is discussed in the chapter 2 and 3.

1.3 OUTLINE OF THIS THESIS

As early result of the commisioning of the FMLO method in ASTE 10 m, Tamura et al. (2013) observed a bright ^{12}CO (3–2) spectral line of Orion KL with the preliminary FMLO system and demonstrated an improvement of observation effi-
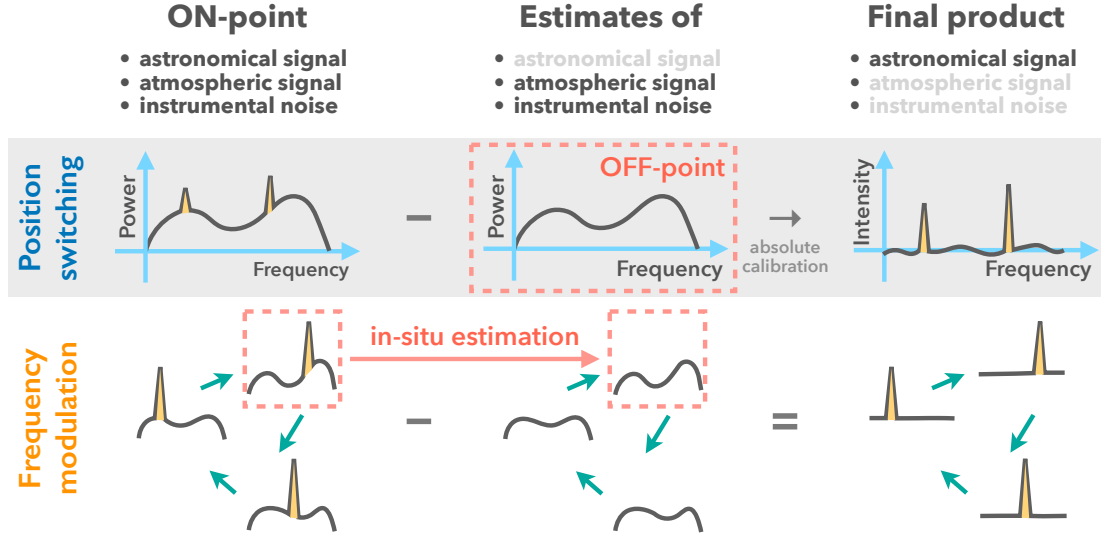
Figure 1.8: Schematic diagram to express how frequency modulation (FM) method is different from position switching (PSW) one. Both methods are intended to estimate and subtract an atmospheric signal and instrumental noise (center column) from an ON-point power spectrum (left column) in order to obtain a spectrum of only astronomical signal (right column). Conventional PSW method (middle row) estimates it as a result spectrum of observing different position and time (i.e., OFF-point). Subtraction of it from ON-point spectrum, however, may cause baseline wiggles due to difference of sky condition in both position and time. On the other hand, FM method (bottom row) estimates it as a result of in-situ linear fitting of common mode spectra which is derived by principal component analysis (PCA) applied to a timestream ON-point FM spectra. In-situ estimates can trace time-variable atmosphric signal and instrumental noise (correlated noises) and thus it is expected to reduce baseline wiggles.

ciency by a factor of 4.9 compared to conventional PSW method. At that moment of the FMLO method, however, the following items are not verified yet which are essential to be demonstrated for claiming the consistency and advantages of the FMLO method compared to PSW and also defining the limitation of the FMLO method:

Time synchronization The precise time synchronization between frequency modulation of LO and data acquisition of a spectrometer is essential but not achieved yet at that moment. If we obtain a timestream at a sampling rate of 10 Hz (a spectrum is outputed every 100 millisecond), a synchronization within ∼1 ms is required. We therefore implement a controller for such time

synchronization.

Gain correction Calibration method for the FMLO method is not yet developed for correcting for gain, which is also expected to be frequecy modulated during an ON-point observation.

Optimal frequency modulation We don't get the guide of how to modulate frequency (i.e., width or step of frequency modulation one ofter another). Such frequency modulation pattern should be optimized (in a multi-pixel camera observation, how to sweep in a mapping region (scan pattern) is optimized for the spatial distribution of a target).

Detailed verification for consistency The consistency of the result spectrum of the FMLO compared to that of PSW should be verified by both actual astronomical line observation and artificial line simulation, with various line shapes and line intensity from brighter one (like Orion KL) to faint one (signal-to-noise ratio of $\lesssim 5$, for example).

Atmospheric line emission The bright spectral line emission from the Earth's atmosphere such as ozone is possible to be detected in an FMLO observation because of no OFF-point observation. Such spectral lines other than astronomical ones should be modeled and subtracted properly in a final spectrum.

In this thesis, we establish, for the first time, a data analysis method of the FMLO observations: We point out, for the first time, issues about the observation equations, calibration method of PSW which is raised when we extend them for the frequency-modulating observations (e.g., gain correction and contamination of atmospheric line emission). Then we propose and develop signal processing methods to resolve the issues and demonstrate, for the first time, that there exist correlated noises under the proper calibration method based on proper observation equations. We verify, for the first time, the consistency of FMLO methods with PSW one in terms of absolute intensity (i.e., spectral line shape), achieved noise level based on correlated noise removal in both single-pointing spectrum and on-the-fly mapping observations. Finally we demonstrate much higher observing

19

efficiency (i.e., effective sensitivity) achieved by the observations with the FMLO method. Here is an outline of this thesis:

Chapter 1 The chapter of introduction (this chapter).

Chapter 2 The chapter of the principle of the FMLO method. We introduce mathematical expression of a timestream and its modulation, demodulation, and reverse-demodulation, which are fundamental operations used in the following chapters. We also describe noise characteristics and its isolation by PCA. Finally we describe how to convert a timestream to a final spectrum of map (in the case of mapping observation).

Chapter 3 The chapter of implementation of FMLO systems for Nobeyama 45 m and ASTE 10 m. First of all, we describe minimuml requisites for an implementation of the FMLO method. We then describe how an FMLO system operates in an telescope with block diagram of the FMLO system and results of the system time synchronizations of both Nobeyama 45 m and ASTE 10 m.

Chapter 4 The chapter of developing signal processing of the FMLO method. Here we introduce timestream-based observation equations of the FMLO method and calibration strategies of gain and intensity for such timestream data. We then describe the detailed methods of correlated component removal using normal PCA and weighted PCA achieved by EM-algorithm (Bailey, 2012), which is used for modeling and subtracting atmospheric line emission. Finally we introduce an end-to-end pipeline algorithm for the data reduction of an FMLO timestream, which conduct iterative estimation processes from calibration to correlated component removal.

Chapter 5 The chapter of the verification for the FMLO method of several items mentioned above using timestream data observed or measured on telescope sites. We conduct an end-to-end data reduction using the pipeline in chapter 4 to verify gain and intensity correction, and consistency of the FMLO method compared to PSW by conducting simulation embedding artificial

20

line emission to the obtained timestreams. We obtain an observation efficiency achieved by such observations, and obtain the guide for an optimal frequency modulation pattern for an FMLO observation by also simulation.

Chapter 6 The chapter of the demonstration of the FMLO method using actual astronomical targets. We show the results of several spectral line and mapping observations of Nobeyama 45 m and/or ASTE 10 m and demonstrate that they are consistent with those of conventional methods. In the FMLO mapping observations, we further discuss the consistency of FMLO and the conventioal method and demonstrate an improvement of observation efficiency of the FMLO mapping observation.

Chapter 7 The chapter of the general discussion together with all results of the previous chapters. We describe the adbantages and also limitation of the FMLO method compared to the conventional observing methods. We also discuss computation costs and future prospects of the FMLO method and correlated noises removal scheme.

Chapter 8 The chapter of the conclusion for this thesis.

Simple is better than complex.
Complex is better than complicated.

  From the Zen of Python, by Tim Peters

2

Principle

This chapter describes the principle of the FMLO method with mathematical expression. We aim to express a frequency-modulated timestream data (time-series spectra) as an output from a spectrometer at 10 Hz, (§ 2.1), and introduce the concept of modulation and demodulation of a timestream for both signal and image sideband , which are used for making a specrum of map from a timestream (§ 2.2 and 2.3). Then we describe how we derive a modulated timestream corresponding to T_A^* of the conventional position switching (PSW) method, from a timestream after intensity calibration (§ 2.4). We express how signal and noises are characterized in a calibrated timestream and how correlated components are defined and removed from it to make a "clean"ed timestream. Finally we describe how we convert a cleaned timestream to a final product of a spectrum (single point observation) or a map (on-the-fly observation) and vice versa (§ 2.5). We note that only mathemtical definition is discussed in this chapter. The actual algorithms such intensity caliration, correlated component removal are discussed in chapter 4.

2.1 Mathematical expression of timestreams

We define timestreams as matrices whose axes are frequency and time (time-series spectra). Although frequency and time are originally continuous, we usually obtain them as an output of a digital spectrometer which has discrete D frequency channels with channel width of $d\nu$ (total bandwidth of $Dd\nu$), and discrete N spectra with sampling interval of dt (total observation time of Ndt). Thus we can express an arbitrary timestream of any physical units with a bold letter like:

$$
\boldsymbol{X} \equiv \{x_{dn}\} = \begin{pmatrix} x_{11} & \cdots & x_{1n} & \cdots & x_{1N} \\ \vdots & \ddots & \vdots & \ddots & \vdots \\ x_{d1} & \cdots & x_{dn} & \cdots & x_{dN} \\ \vdots & \ddots & \vdots & \ddots & \vdots \\ x_{D1} & \cdots & x_{Dn} & \cdots & x_{DN} \end{pmatrix} \tag{2.1}
$$

We use $\boldsymbol{X}_{:,n}$ and $\boldsymbol{X}_{d,:}$ to denote n-th column vector (n-th sampled spectrum) and d-th row vector (d-th channel's time-series data), respectively. The scalar element of d-th channel in n-th sampled spectrum is $\boldsymbol{X}_{dn}$ ($= x_{dn}$).

We also define the mathmatical operations between timestreams. Since there are many element-wise operations between timestreams in the following equations, we express them in the same manner as scalar values:

$$
\boldsymbol{X}\boldsymbol{Y} \equiv \{x_{dn}y_{dn} \,|\, x_{dn} \in \boldsymbol{X}, y_{dn} \in \boldsymbol{Y}\} \tag{2.2}
$$

$$
\boldsymbol{X}/\boldsymbol{Y} \equiv \{x_{dn}/y_{dn} \,|\, x_{dn} \in \boldsymbol{X}, y_{dn} \in \boldsymbol{Y}\} \tag{2.3}
$$

$$
\boldsymbol{X}^{\boldsymbol{Y}} \equiv \{x_{dn}^{y_{dn}} \,|\, x_{dn} \in \boldsymbol{X}, y_{dn} \in \boldsymbol{Y}\} \tag{2.4}
$$

For the convinience in the following equations, we use bold symbol of constants such as $\boldsymbol{0}$, $\boldsymbol{1}$ and $\boldsymbol{e}$, which are $D \times N$ matrices filled with 0, 1, and e, respectively.
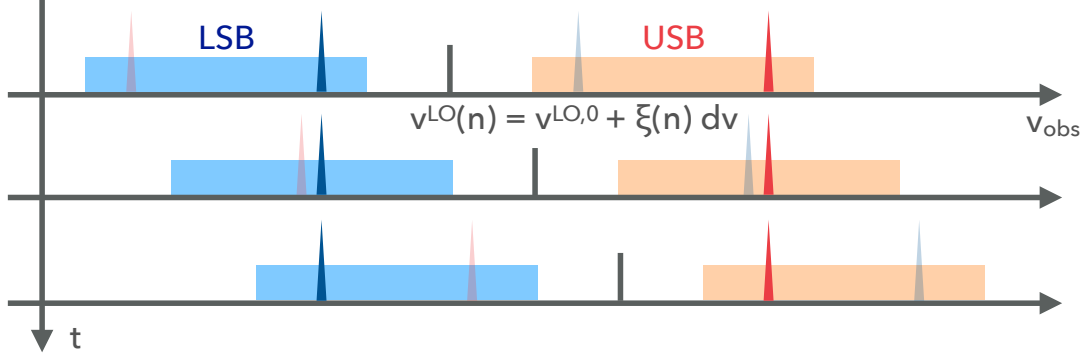
Figure 2.1: Schematic diagram of expressing modulation and demodulation of a timestream according to FM channels, supposing an FMLO observation of both USB (orange box) and LSB (lightblue one) where only one spectral line (red and blue spikes) exists at each sideband. A modulated timestream is an output of a spectrometer itself: It obtain data with fixed IF range (represented as two boxes). On the other hand, a demodulated timestream is a matrix that we align each sample of modulated timestream with RF (observed) frequency. From the diagram, it is clear that a line in a sideband and that contaminated from the *image* sideband is revesely frequency modulated, which enable us to achieve sideband separation based on software post reduction.

2.2 MODULATION AND DEMODULATION OF TIMESTREAMS

We define the frequency modulation of RF frequency with discrete changes of 1st LO frequency synchronized with the sampling of the spectrometer. We can express RF frequency at the center of observed band, ν^{RF}, and 1st LO frequency, ν^{LO}, as a function of sampling number n $(1 \leq n \leq N)$:

$$\nu^{\mathrm{RF}}(n) = \nu^{\mathrm{LO}}(n) + \nu^{\mathrm{IF}} \tag{2.5}$$

where ν^{IF} represents IF frequency ($\nu^{\mathrm{IF}} < 0$ for lower sideband and $\nu^{\mathrm{IF}} > 0$ for upper sideband) and is constant during an observation. Now we introduce the frequency modulation (FM) channel, $\xi(n)$, which represents frequency offset between n-th observed spectrum and reference one in units of channel:

$$\xi(n) \equiv \frac{\nu^{\mathrm{RF}}(n) - \nu^{\mathrm{RF},0}}{\mathrm{d}\nu} = \frac{\nu^{\mathrm{LO}}(n) - \nu^{\mathrm{LO},0}}{\mathrm{d}\nu} \tag{2.6}$$

24

where $\nu^{\mathrm{RF},0}$ and $\nu^{\mathrm{LO},0}$ represent RF and LO frequencies of reference observation such as load observation (hereafter 0 denotes "reference"). Although $\xi(n)$ is not necessarily an integer, it is useful to assume $\xi(n)$ to be an integer for computational purposes. We also define the zero-based FM channel, $\bar{\xi}(n)$, for the convenience in the following equations:

$$\bar{\xi}(n) \equiv \xi(n) - \min(\{\xi(1), \ldots, \xi(N)\}) \tag{2.7}$$

By definition, the maximum value of $\bar{\xi}(n)$ equals the total width of FM channel during an observation.

In this paper, we express modulated timestreams with $D \times N$ matrices like $\boldsymbol{X}$, where D and N represent the number of spectrometer's channels aligned with IF frequency, and the number of samples, respectively. In the same manner we can express demodulated timestreams with $\tilde{D} \times N$ matrices like $\tilde{\boldsymbol{X}}$, where $\tilde{D}$ represents the number of channels aligned with RF frequency (hereafter tilde denotes "demodulation"), which is the sum of D and the total width of FM channel during an observation:

$$\tilde{D} \equiv D + \max(\{\bar{\xi}(1), \ldots, \bar{\xi}(N)\}) \tag{2.8}$$

The operator of demodulation is a mapping $\mathcal{DM} : \boldsymbol{X} \to \tilde{\boldsymbol{X}}$ (i.e., from a modulated timestream to demodulated one), which is defined as the following relation:

$$\tilde{\boldsymbol{X}}_{dn} = \begin{cases} \boldsymbol{X}_{d-\bar{\xi}(n),n} & (d - \bar{\xi}(n) > 0) \\ \mathrm{NaN} & (\text{otherwise}) \end{cases} \tag{2.9}$$

where NaN (not-a-number) represents not-observed value and should be excluded in matrix computation such as averaging $\tilde{\boldsymbol{X}}$ over time axis to make a spectrum. In the same manner, the operator of modulation is a mapping $\mathcal{M} : \tilde{\boldsymbol{X}} \to \boldsymbol{X}$:

$$\boldsymbol{X}_{dn} = \tilde{\boldsymbol{X}}_{d+\bar{\xi}(n),n} \tag{2.10}$$

By definition, NaNs ($\in \tilde{\boldsymbol{X}}$) are not mapped to $\boldsymbol{X}$, which guarantees the equalities

25
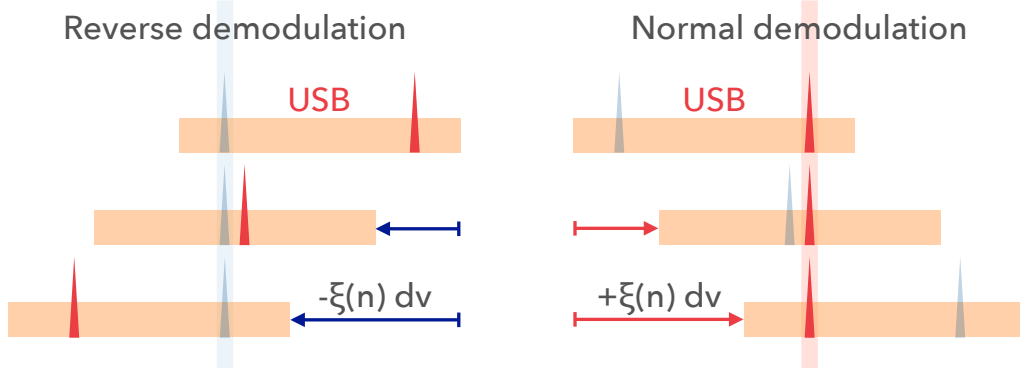
Figure 2.2: Schematic diagram of reverse-demodulation of a timestream. As we see in figure 2.1, demodulation according to FM channels with their signs reversed will align a timestream with RF frequncy of *image* sideband: Such contamiation can be modeled and subtracted if we integrate the reverse-demodulated timestream to make a supectrum of contamiation.

of $\boldsymbol{X} = \mathcal{M}(\mathcal{D}\mathcal{M}(\boldsymbol{X}))$ and $\tilde{\boldsymbol{X}} = \mathcal{D}\mathcal{M}(\mathcal{M}(\tilde{\boldsymbol{X}}))$. These concept of FM channel, modulation and demodulation of a timestream are illustrated in figure 2.1.

2.3 Sideband separation with reverse-demodulation

For an FMLO observation with a sideband separation mixer, signal leaking from image sideband may worsen the sensitivity of the final spectrum if there exists strong line emission in them. As one of the advantages of the FMLO method, we can model the leaked line emission from image sideband independently of that from signal sideband. For any signals within the signal sideband whose observed frequency is ν, we can express the frequency offset from the center of observed band, $\nu^{\mathrm{RF}}(n)$, as a function of $\xi(n)$:

$$\nu - \nu^{\mathrm{RF}}(n) = (\nu - \nu^{\mathrm{RF},0}) - \xi(n)\,\mathrm{d}\nu \tag{2.11}$$

Any signals in the image sideband whose observed frequency is ν^{i}, on the other hand, may appear in the signal sideband as leaked signal at the observed frequency of ν:

$$\nu = \nu^{\mathrm{i}} + 2(\nu^{\mathrm{LO}}(n) - \nu^{\mathrm{i}}) = (2\nu^{\mathrm{LO},0} - \nu^{\mathrm{i}}) + 2\xi(n)\,\mathrm{d}\nu \tag{2.12}$$

Hereafter i denotes "image sideband". Substituting equation 2.12 for equation 2.11, the frequency offset from $\nu^{\mathrm{RF}}(n)$ regarding leaking signal is expressed as:

$$\nu - \nu^{\mathrm{RF}}(n) = (2\nu^{\mathrm{LO},0} - \nu^{\mathrm{i}} - \nu^{\mathrm{RF},0}) + \xi(n)\,\mathrm{d}\nu \tag{2.13}$$

This indicates that the leaked signal from the image sideband is modulated reversely: We can model the leaked signal because it is aligned when the timestream is reverse-demodulated by adopting $-\xi(n)$ as FM channel instead of $+\xi(n)$, while the native signal is smeared out in the final spectrum. On the other hand, the leaked signal is not aligned with RF frequecy in a demodulated timestream and thus smeared out in the final spectrum even if we do not model the leaked signal. This can reduce the noise induced by the leaking signal, and thus improve an image sideband rejection ratio by only signal processing discussed above. The concept of reverse-demodulation is illustrated in figure 2.2.

2.4 Noise characteristics and isolation

Using the expression of modulated timestreams, we can model a measured timestream of antenna temperature after intensity calibration, $\boldsymbol{T}^{\mathrm{Calib}}$, as antenna temperatures in two sidebands for heterodyne receiver in addition to correlated and non-correlated noises from the sky and instruments:

$$\begin{aligned}
\boldsymbol{T}^{\mathrm{Calib}} &= \boldsymbol{T}^{\mathrm{Ast}}\boldsymbol{e}^{-\boldsymbol{\tau}} + T^{\mathrm{Atm}}(\mathbf{1} - \boldsymbol{e}^{-\boldsymbol{\tau}}) \\
&\quad + R\left[\boldsymbol{T}^{\mathrm{Ast,i}}\boldsymbol{e}^{-\boldsymbol{\tau}^{\mathrm{i}}} + T^{\mathrm{Atm}}(\mathbf{1} - \boldsymbol{e}^{-\boldsymbol{\tau}^{\mathrm{i}}})\right] + \boldsymbol{E}
\end{aligned} \tag{2.14}$$

where $\boldsymbol{T}^{\mathrm{Ast(,i)}}$, $\boldsymbol{\tau}^{\mathrm{(i)}}$, $\boldsymbol{E}$, $\boldsymbol{e}$, and $\mathbf{1}$ are $D \times N$ matrices: $\boldsymbol{T}^{\mathrm{Ast}}$ is the modulated antenna temperature of astronomical source corrected for atmospheric absorption and spillover loss, T^{Atm} is the physical temperature of atmosphere, $\boldsymbol{\tau}$ is the modulated opacity of atmosphere, and matrices with i are those from image sideband. R is an image rejection ratio of a sideband separation mixer ($R = 1$ for a double sideband mixer). $\boldsymbol{E}$ is the noises attributed to the atmosphere and telescope system.

Using low-rank approximation techniques such as PCA, we can decompose the following timestreams into correlated and non-correlated components:

$$\boldsymbol{T}^{\mathrm{Ast}(,\mathrm{i})} = \boldsymbol{T}^{\mathrm{C}(,\mathrm{i})} + \boldsymbol{T}^{\mathrm{NC}(,\mathrm{i})} \tag{2.15}$$

$$\boldsymbol{\tau}^{(\mathrm{i})} = \boldsymbol{\tau}^{\mathrm{C}(,\mathrm{i})} + \boldsymbol{\tau}^{\mathrm{NC}(,\mathrm{i})} \tag{2.16}$$

$$\boldsymbol{E} = \boldsymbol{E}^{\mathrm{C}} + \boldsymbol{E}^{\mathrm{NC}} \tag{2.17}$$

Hereafter C and NC denote "correlated" and "non-correlated" timestreams, respectively. The correlated components of $\boldsymbol{T}^{\mathrm{C}}$ and $\boldsymbol{\tau}^{\mathrm{C}}$ are attributed to continuum emission from astronomical source and sky, the latter of which usually fluctuates during an observation. The non-correlated components of $\boldsymbol{T}^{\mathrm{NC}}$ and $\boldsymbol{\tau}^{\mathrm{NC}}$ are attributed to spectral line emission and/or absorption from astronomical source and the atmosphere (atmospheric ozone, for example), respectively. $\boldsymbol{E}^{\mathrm{C}}$ is the correlated noise, which is mainly attributed to the fluctuation of bandpass gain coupled with the sky and instruments. $\boldsymbol{E}^{\mathrm{NC}}$ is the residual non-correlated noises which is expected to follow a Gaussian distribution. After subtracting correlated terms from equation 2.14 which are composed of at least one of correlated components (for example, $\boldsymbol{T}^{\mathrm{C}}\boldsymbol{e}^{-\boldsymbol{\tau}^{\mathrm{C}}}$), the "clean"ed timestream is composed of only non-correlated terms:

$$\begin{aligned}
\boldsymbol{T}^{\mathrm{Clean}} \simeq{}& \boldsymbol{T}^{\mathrm{NC}}\boldsymbol{e}^{-\boldsymbol{\tau}^{\mathrm{NC}}} + T^{\mathrm{Atm}}(\boldsymbol{1} - \boldsymbol{e}^{-\boldsymbol{\tau}^{\mathrm{NC}}}) \\
&+ R\left[\boldsymbol{T}^{\mathrm{NC,i}}\boldsymbol{e}^{-\boldsymbol{\tau}^{\mathrm{NC,i}}} + T^{\mathrm{Atm}}(\boldsymbol{1} - \boldsymbol{e}^{-\boldsymbol{\tau}^{\mathrm{NC,i}}})\right] \\
&+ \boldsymbol{E}^{\mathrm{NC}}
\end{aligned} \tag{2.18}$$

where we obtain the modulated antenna temperature of astronomical source except for continuum emission and that from image sideband, which raise a limitation of continuum observation with the FMLO method (discussed further in chapter 7).

Finally, modeling and subtracting non-correlated components other than astronomical source, we obtain a modulated timestream, $\boldsymbol{T}^{\mathrm{A}^*}$, which is consistent with T_{A}^* of the conventional position switching (PSW) method except that it is

modulated.

$$\boldsymbol{T}^{\mathrm{A}^*} \simeq \boldsymbol{T}^{\mathrm{NC}} \boldsymbol{e}^{-\boldsymbol{\tau}^{\mathrm{NC}}} + \boldsymbol{E}^{\mathrm{NC}} \tag{2.19}$$

If astronomical spectral lines do not overlap with those from the atmosphere, the equation 2.19 is simply expressed as:

$$\boldsymbol{T}^{\mathrm{A}^*} \simeq \boldsymbol{T}^{\mathrm{NC}} + \boldsymbol{E}^{\mathrm{NC}} \tag{2.20}$$

Otherwise, contribution of absorption by atmospheric line, $\boldsymbol{e}^{-\boldsymbol{\tau}^{\mathrm{NC}}}$, should be derived from $T^{\mathrm{Atm}}(\boldsymbol{1} - \boldsymbol{e}^{-\boldsymbol{\tau}^{\mathrm{NC}}})$ and corrected to derive 2.20. In this case, division of $\boldsymbol{e}^{-\boldsymbol{\tau}^{\mathrm{NC}}}(< 1)$ may worsen the noise level at the observed frequency where atmospheric lines exist.

How to model the components we see above will be discussed in chapter 4, where we introduce new algorithms to model them. Modeling them of actual data will be discussed in chapter 5.

2.5   Making final product

Once we obtain a final modulated timestream, $\boldsymbol{T}^{\mathrm{A}^*}$, it is time we demodulate them to $\tilde{\boldsymbol{T}}^{\mathrm{A}^*}$ and then we can make a final product of a spectrum in the case of single-pointing observations, or map in the case of on-the-fly (OTF) observation in the same manners as we make them from the data observed with the conventional PSW method. The difference of the process between FMLO and PSW is that after making a spectrum or a map as the final product, it is possible that we reshape it to a shape (dimension) same as the modulated timestream to use it as *a signal model* in a succeeding iterative signal processing for better estimation. We hereafter refer to "integration" as we convert a timestrem to a spectrum or a map, and "projection" as we fill values of a spectrum or a map to a timstream.
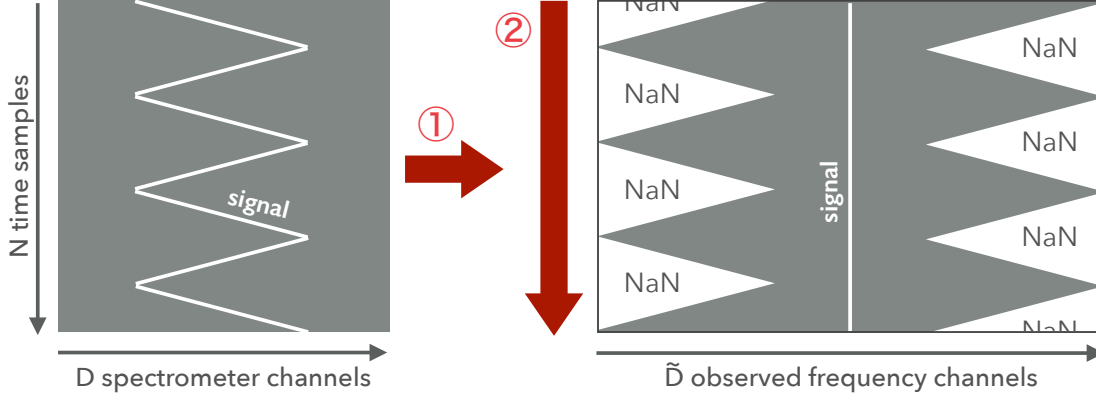
Figure 2.3: Schematic diagram of integration and projection processes of spectral making. Integration process is to convert a modulated timestream into demodulated one, and then make a spectrum in demodulation space by calculating mean along time axis without counting NaN elements. On the other hand, projection process is to make a demodulated timestream with each time sample filled with a spectrum and then make a modulated timestream.

2.5.1 Spectral making

A spectrum of the FMLO method, $\tilde{\boldsymbol{s}}$, is a $\tilde{D}$-length vector. Integration and projection are illustrated in figure 2.3. Integration of a demodulated timestream to a spectrum is simply the mean of it taken along the time axis except for NaN values:

$$\tilde{\boldsymbol{s}}_d = \frac{\sum_{n=1}^{N} \tilde{\boldsymbol{T}}_{dn}^{\mathrm{A}^*} \left(\tilde{\boldsymbol{T}}_{dn}^{\mathrm{A}^*} \notin \mathrm{NaN} \right)}{\sum_{n=1}^{N} 1 \left(\tilde{\boldsymbol{T}}_{dn}^{\mathrm{A}^*} \notin \mathrm{NaN} \right)} \tag{2.21}$$

If we define weight values of each element of a timestream (for example, from system noise temperature, T_{sys}), this operation shall be a weighted mean. At the same time, we also derive the r.m.s. noise level of a spectrum. If we obtain statistically-sufficient samples, a simple way is to calculate the standard deviation of a demodulated timestream along the time axis except for NaN and dividing each value by root of the number of samples counted. Another one is to resample the timestream by the bootstrap method to make resampled spectra several times
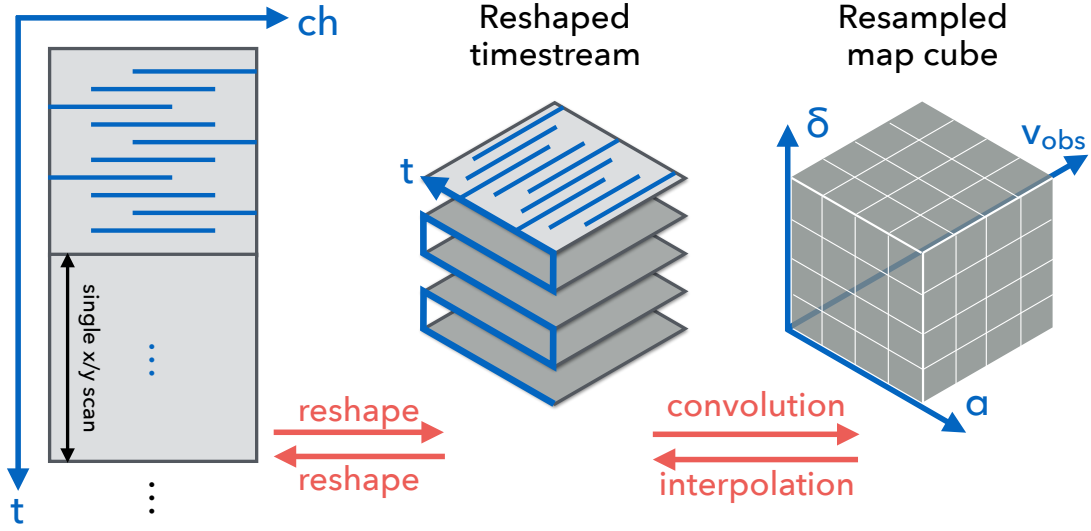
Figure 2.4: Schematic diagram of integration and projection processes of map making. (left) A demodulated timestream whose non-NaN values are expressed as blue lines. (center) A reshaped (folded) 3D-cube-like timestream according to a scan pattern of a mapping observation. At this moment, each sample of the timestream is not weight-meaned. (right) A 3D cube map after weighted mean (equation 2.23). An integration process is to convert a timestream into a 3D map cube (left to right). On the other hand, a projection process is to convert a 3D map cube to a timestream whose shape is same as the input timestream, which can be derived by 2D (spatial axes) interpolation of a 3D map cube at a map coordinates of R.A and Dec. We note that both integration and projection processes include demodulation and modulation (which are not illustrated, though).

and calculate the standard deviation of them. The latter takes more time but will be used for deriving exact noise level in chapter 5.

Projection of a spectrum to a timestream is calculated by (1) creating a demodulated timestream each column vector filled with the spectrum, and (2) modulating it to create demodulated one.

2.5.2 MAP MAKING

There are mounting demands for large-scale mapping observations using (sub-)millimeter single-dish telescopes. The FMLO method offers mapping capability by just slewing telescope pointing contiguously. A map of the FMLO method, $\tilde{\boldsymbol{M}}$, is a $X \times Y \times \tilde{D}$ tensor (3D data cube), where X and Y are the horizontal and vertical numbers of grids of a map. With this type of making, an FMLO

observation is supposed to be carried out with telescope moving according to a scan pattern which controls how to scan a region as a function of time. The number of grids and thus grid spacing are coupled with a beam size of a telescope and scan pattern used for an observation. Integration and projection are illustrated in figure 2.4.

Integration of a demodulated timestream to a map is a weighted mean of samples located within a certain radius of each map grid. The weight values are calculated by a gridding convolution function (GCF), $c(r)$, described in (Sawada et al., 2008), where r is a distance between antenna coordinates of a sample and those of a map grid in units of grid spacing. For example, the pure Gaussian GCF can be expressed as the following equation:

$$c(r) = \begin{cases} \exp\left(-r^2\right) & (r \leq R_{\mathrm{max}}) \\ 0 & (\text{otherwise}) \end{cases} \tag{2.22}$$

where R_{max} is the maximum radius within which samples are included to calculate the weighted mean. We use $R_{\mathrm{max}} = 3$ as default. The value of a frequency channel, d, at a map grid (x, y) is thus expressed as the following equation:

$$\tilde{\boldsymbol{M}}_{x,y,d} = \frac{\sum_{n=1}^{N} c(r_n) \, \tilde{\boldsymbol{T}}_{dn}^{\mathrm{A}^*} \left(r_n \leq R_{\mathrm{min}}, \, \tilde{\boldsymbol{T}}_{dn}^{\mathrm{A}^*} \notin \mathrm{NaN}\right)}{\sum_{n=1}^{N} c(r_n) \left(r_n \leq R_{\mathrm{min}}, \, \tilde{\boldsymbol{T}}_{dn}^{\mathrm{A}^*} \notin \mathrm{NaN}\right)} \tag{2.23}$$

Projection of a map to a timestream is calculated by (1) creating a demodulated timestream each column vector filled with the spectrum which are calculated by 2D (spatial axes) interpolation of the map at each antenna coordinates, and (2) modulating it to create demodulated one.

Flat is better than nested.
Sparse is better than dense.
Readability counts.

From the Zen of Python, by Tim Peters

3

Implementation

In the proposed FMLO method, it is important to modulate astronomical signals of interest into high frequency ranges in timestream data by modulating the observing frequency, which enables to isolate the astronomical signals from low-frequency correlated noises. Whereas there are several options of modulating the observing frequency, we choose to modulate radio frequency (RF) signals. This is because (1) in many modern systems a first LO is realized with a tunable digital signal generator in which a built-in modulation function is implemented; and (2) RF modulation in mm/submm allows a wide (GHz-order) frequency change compared with IF modulation. There is, however, a drawback in first LO modulation; an LO frequency modulation leads to changes in the mixer gain, which depend on frequency modulation. We will show that the gain changes are fully predictable as a function of LO frequency in short time-scales ($\sim$10 min) and are reasonably modeled and corrected in offline signal processing. This will be discussed in § 4.

3.1 Minimum requisites

Minimum requisites on a telescope system where the FMLO system is going to be installed are (1) a first LO which is tunable and programmable; (2) a system

33

clock which ensures the synchronization among frequency modulation and data acquisition; and (3) a backend spectrometer that takes the data at a sampling rate sufficiently higher than the sky/system variation. A heterodyne receiver in modern mm/submm astronomy often utilizes a microwave signal generator with a cascade of frequency multipliers, instead of a Gunn oscillator, as a first LO. A digital signal generator is particularly useful for the FMLO purpose, since it is easy to quickly tune the LO frequency and to program the frequency modulation pattern. A sampling rate of $\sim$0.1 s should be enough for many cases; the time-scale of sky variation is of order $\sim$1 s, since it is roughly determined by a crossing-time in which the phase screen ($v \sim 10$ m s^{-1}) goes across the telescope aperture ($D \sim 10$ m). Note that when we apply the FMLO method to on-the-fly (OTF) mapping rather than single-pointed observations, synchronization between frequency modulation and antenna drive control is also required.

3.2 Nobeyama 45 m

We installed the FMLO system on the Nobeyama 45 m telescope in 2013. Figure 3.1 shows the schematic block diagram of the Nobeyama 45 m receiver system equipped with an FMLO. The receiver system comprises the two-beam TZ front-end receiver with a cryogenic superconductor-insulator-superconductor (SIS) mixer (Nakajima et al., 2013) and the digital backend spectrometer SAM45, which is an exact copy of the ALMA ACA correlator (Kamazaki et al., 2012), while we just uses a single IF (a single beam and a single polarization). We employed a signal generator, Agilent E8257D, which is capable of generating a continuous wave (CW) according to a list of frequencies given by an observer. Each frequency in the list is switched to by external TTL-compatible reference triggers one by one. The trigger is produced with an arbitrary waveform generator, Agilent E33521A. The waveform generator produces a rectangular wave with a period of 100 ms, which is synchronized with the telescope system clock via 1 pps and 10 MHz reference signals. The period must be identical to the sampling rate of the spectrometer outputs, and the phase of the rectangular wave must be synchronized with the onset of data acquisition/integration. The local controller unit (LCU) of the 45 m
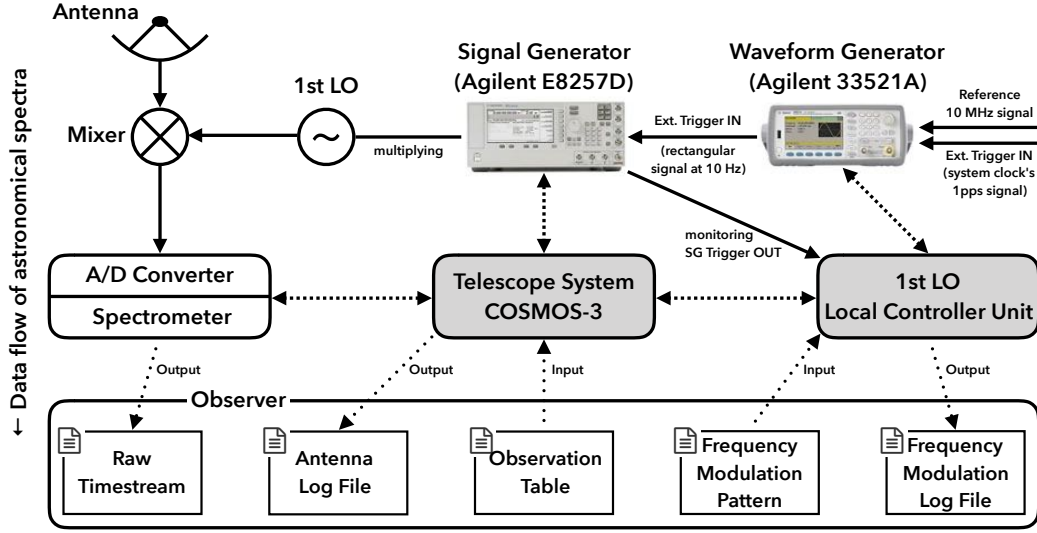
Figure 3.1: Block diagram of the Nobeyama 45 m receiver system equipped with an FMLO. The solid arrows represent directions of signal and the dashed ones represent those of data or communication between instruments. The diagram shows 3 layers: (top) the frontend receiver system, where RF signal from sky and frequecy-modulated LO signal are mixed at the SIS mixer and subsequent IF signal is analog-to-digital converted and input to the spectrometer; (middle) the backend spectrometer and telescope system, where the `COSMOS-3` controls both frontend and backend; (bottom) an observer who creates an observation table for the FMLO and frequency modulation file as inputs and receives the raw timestream data, frequency modulation and antenna moving log files as outputs.

telescope system (`COSMOS-3`; Morita et al. (2003), Kamazaki et al. (2005)) reads the frequency list (a frequency modulation pattern file) given by a user before an observation starts and sends the list to the signal generator.

Once the telescope begins a stable tracking, the receiver is properly tuned, and the spectrometer setup is ready, then the LCU triggers the signal generator when the data acquisition starts. During an FMLO observation the spectral data are recorded at a rate of 10 Hz in typical. This is made in the on-the-fly (OTF) mode of the 45 m (Sawada et al., 2008), while the telescope pointing may stare at a single point on the sky. The 45 m OTF control methods of the antenna, the spectrometer, Doppler tracking of the receiver, and data formatting are presented by (Sawada et al., 2008). During the observation, the LCU writes the frequency and timestamp and saves them as a frequency log file. At the same time, the spectrometer records a series of spectra at 10 Hz, but it does not know what the
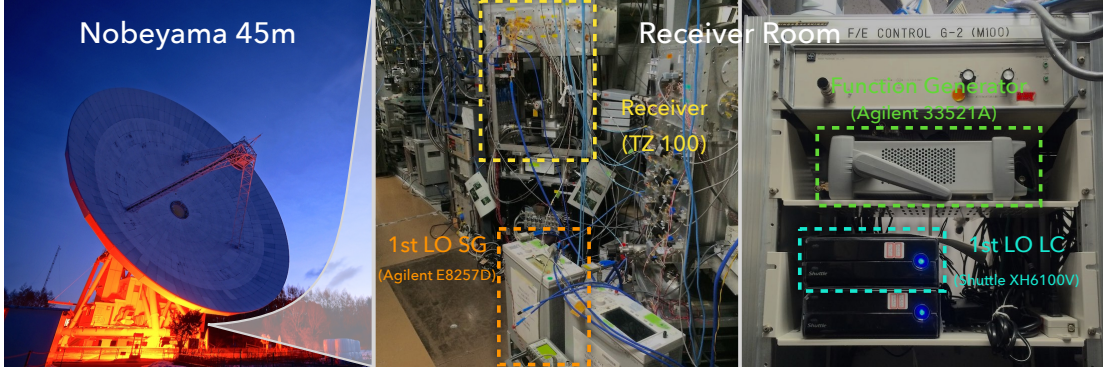
Figure 3.2: (left) The Nobeyama 45 m telescope at Nobeyama, Nagano, Japan. (center, right) Photos of the receiver room of Nobeyama 45 m located at the beneath the antenna. The instruments we utilized for the FMLO observations are indicated as colored dashed boxes with its names.

observing frequency actually is, so the spectral data and the frequency log data are merged before data analysis.

The synchronization between the frequency modulation and the system clock must carefully be adjusted before observations and is monitored by the LCU by receiving a TTL external trigger signal from the signal generator. Figure 3.3 shows the voltages of the reference trigger and 1 pps signal as a function of time, which shows accurate enough synchronization. The typical error in synchronization is better than $\simeq 200~\mu$s, which is well below a typical dwell time of a single frequency (100 ms). The synchronization between the data acquisition of the spectrometer and the system clock must also be adjusted before observations: If the time of changing LO frequency and that of starting data acquisition are shifted, each spectral datum is possible to be contaminted with leaking signal which is obtained with antecedent LO frequency (spectrum leaking). We adjusted this synchronization and confirmed that the spectrum leaking did not occur before astronomical observations with the FMLO method by observing spectra of bright SiO maser with changing the trigger delay parameter which defers a start time of a waveform generator's output (rectangular wave) after triggered by the 1pps signal of the system clock. This will be discussed in § 5.2.2.

Note that it typically takes $\lesssim 8$ ms to settle the generated LO frequency after the frequency is set from one to another (see Figure 3.3). The E8257D signal
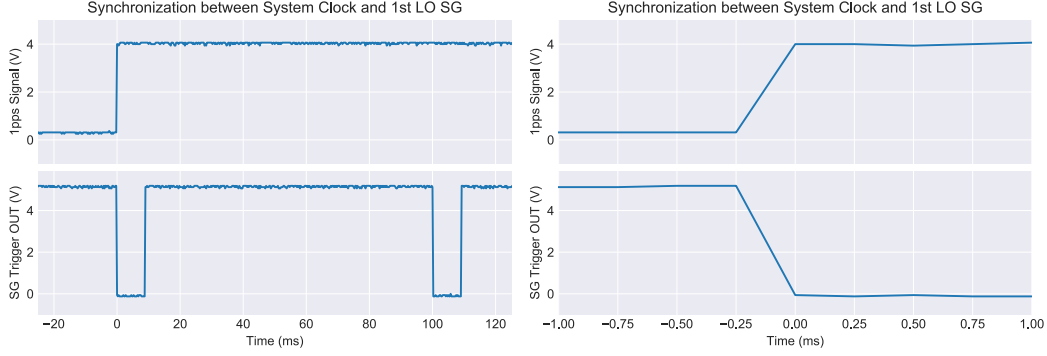
Figure 3.3: The measured signals of 1pps system clock (top) and 1st LO signal generator's reference trigger (bottom) of Nobeyama 45 m in units of voltage. The left panel shows $\Delta t = 150$ ms view of them, where 1pps signal rises at $t = 0$ ms while the trigger signal falls synchronized with 1pps clock. The subsequent $\Delta t \simeq 8$ ms voltage dropping at 0 V is attributed to the settling time of the signal generator, where it doesn't generate signal for LO and thus the SIS mixer is unavailable. The right panel shows the same results, but of $\Delta t = 2$ ms view around $t = 0$ ms, which demonstrates that the time synchronization error is better than 200 μs.

generator (i.e., LO) does not output any CW signal during the interval in which the frequency is going to settle to a programmed one (the settling time, hereafter). This makes the SIS device deactivated temporally, and thus the SIS is unavailable only during a short period of time ($\lesssim 8$ ms). This causes a sensitivity loss of $\lesssim 4\%$ for a dwell time of 100 ms (i.e., $\sqrt{(100-8)/100} \simeq 0.96$). The decrement of astronomical signals is corrected in an intensity calibration process, and we confirmed that this works correctly by comparing the spectrum obtained with the conventional position switching method.

3.3   ASTE 10M

We installed the FMLO system on the ASTE 10 m telescope (Ezawa et al., 2004, 2008) in 2012 and 2016. The ASTE receiver system equipped with an FMLO is similar to that of the Nobeyama 45 m, but the receiver and spectrometer are different. The receiver system comprises the DASH 345 or the ASTE Band 8 (Satou et al., 2008) front-end receivers with a cryogenic SIS mixers and the digital backend spectrometer MAC (Sorai et al., 2000), while we just use a single IF (a single polarization).

37
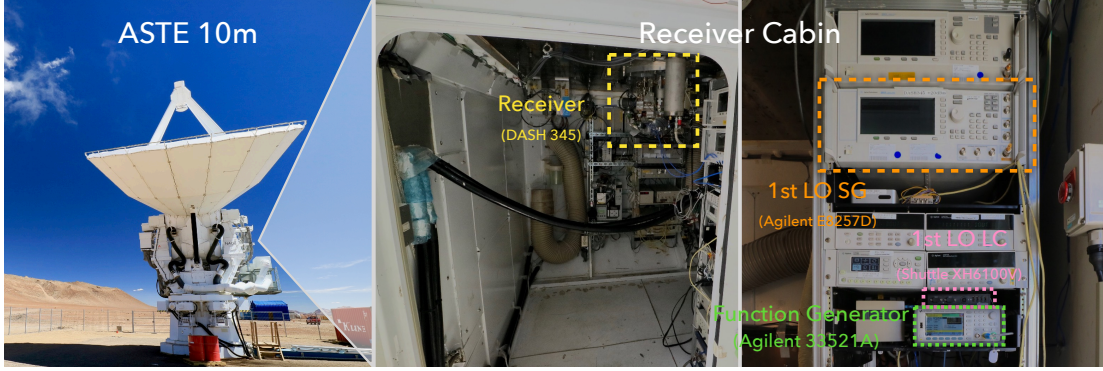
Figure 3.4: (left) The ASTE 10 m telescope at Pampa La Bola, Antofagasta, Chile. (center, right) Photos of the receiver cabin of ASTE 10 m located at the beneath the antenna. The instruments we utilized for the FMLO observations are indicated as colored dashed boxes with its names.

We adjusted the synchronization between the frequency modulation and the system clock. Figure 3.5 shows the voltages of the reference trigger and 1 pps signal as a function of time, which shows accurate enough synchronization. The typical error in synchronization is better than $\simeq 200\ \mu$s, which is well below a typical dwell time of a single frequency (100 ms). We also adjusted synchronization between data acquisition of the spectrometer and the system clock and confirmed that the spectrum leaking did not occur by observing spectra of the atmospheric CO(3–2) rotational line with changing the trigger delay parameter. This will be discussed in § 5.2.2.
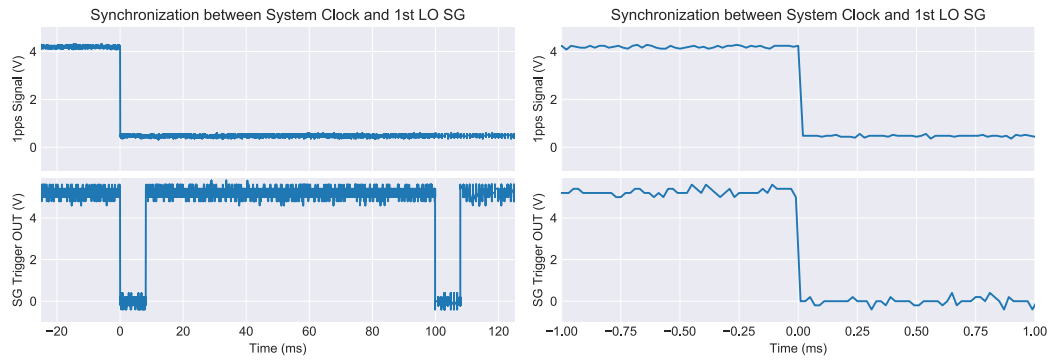
Figure 3.5: The measured signals of 1pps system clock (top) and 1st LO signal generator's reference trigger (bottom) of ASTE 10 m in units of voltage. The left panel shows $\Delta t = 150$ ms view of them, where 1pps signal drops at $t = 0$ ms while the trigger signal rises synchronized with 1pps clock (signs of signals are reversed compared to those of Nobeyama 45 m). The subsequent $\Delta t \simeq 8$ ms voltage dropping at 0 V is attributed to the settling time of the signal generator, where it doesn't generate signal for LO and thus the SIS mixer is unavailable. The right panel shows the same results, but of $\Delta t = 2$ ms view around $t = 0$ ms, which demonstrates that the time synchronization error is better than 200 μs.

4

Signal Processing

This chapter describes the signal processing for observed FMLO data and the pipeline algorithm used in the actual data reduction. We express the observation equations of the one-load chopper wheel method (so called R-SKY calibration, see § 1.1.3) which represent relations between observed quantities and antenna temperatures (§ 4.1). The signal processing has four steps; gain correction (§ 4.2), intensity calibration (§ 4.3), and correlated component removal (§ 4.4). Finally, we present a pipeline algorithm of end-to-end data reduction for observations using the FMLO method which iteratively executes these steps to estimate the final product (§ 4.5). The schematic diagram of the whole signal processing is illustrated in figure 4.1. Throughout the signal processing, we assume the following conditions:

- The physical temperature of atmosphere, T^{Atm}, is equal to that of receiver room, T^{Room}, because we use the one-load chopper wheel method for the intensity calibration

- The observation is carried out with a two sideband (2SB) mixer whose image rejection ratio, R, is much less than unity (more than 10 dB of image rejection ($R < 0.1$) is expected)

- The correlated components of opacity, $\boldsymbol{\tau}^{\mathrm{C}}$, is equal to that from the image sideband, $\boldsymbol{\tau}^{\mathrm{C,i}}$

- The correlated components of antenna temperature of astronomical signal, $\boldsymbol{T}^{\mathrm{C}}$, is equal to that from the image sideband, $\boldsymbol{T}^{\mathrm{C,i}}$, and these two components are much less than T^{Atm}

- Both ON-point and load measurements are obtained by the same spectrometer (i.e., the same IF frequency range), and the center frequencies of observed band, $\nu^{\mathrm{RF}}(n)$, during an frequency-modulating observation cover that of the reference observation, $\nu^{\mathrm{RF,0}}$
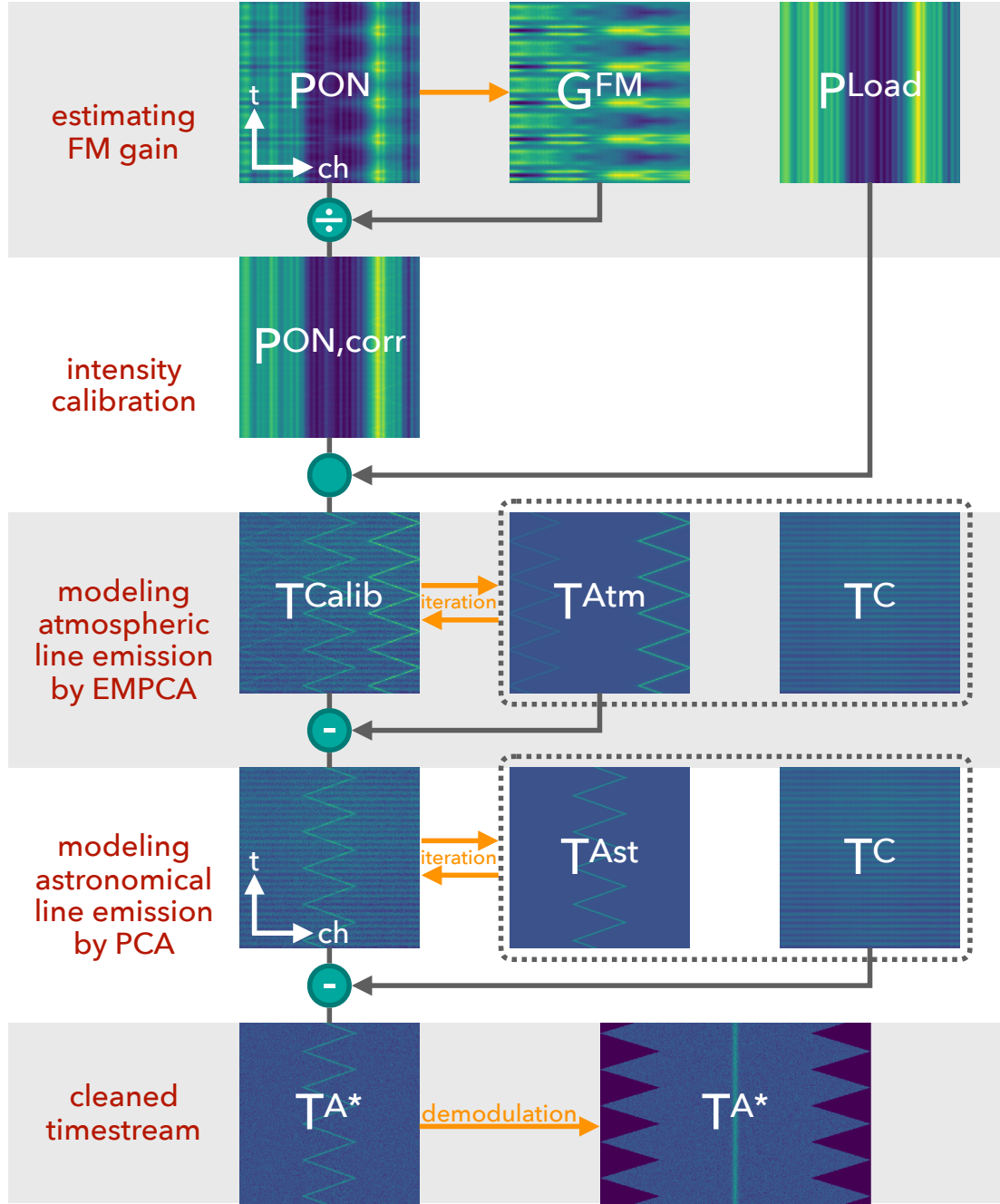
Figure 4.1: Schematic diagram of an overview of signal processing from gain correction (§ 4.2) to correlated component removal (§ 4.4). Each image is a demodulated timestream (time axis is vertical one) whose label is used in the pipeline algorithm 1. Orange arrows indicate some estimation processes, and gray ones indicate some operation between a timestream and esimated one in each step. Orange arrows of both directions indicate iterative processes. See the following sections.

42

4.1 OBSERVATION EQUATIONS

For either spectral or mapping observations using the FMLO method, we obtain the modulated timestream of the ON-point spectra which is proportional to incident power, $\boldsymbol{P}^{\text{ON}}$:

$$
\begin{aligned}
\boldsymbol{P}^{\text{ON}} = \boldsymbol{G}^{\text{ON}} k_{\text{B}} \Big\{ & \eta \Big[\boldsymbol{T}^{\text{Ast}} \boldsymbol{e}^{-\boldsymbol{\tau}} + T^{\text{Atm}} (\mathbf{1} - \boldsymbol{e}^{-\boldsymbol{\tau}}) \\
& + R \left(\boldsymbol{T}^{\text{Ast,i}} \boldsymbol{e}^{-\boldsymbol{\tau}^{\text{i}}} + \boldsymbol{T}^{\text{Atm}} (\mathbf{1} - \boldsymbol{e}^{-\boldsymbol{\tau}^{\text{i}}}) \right) \Big] \\
& + (1 + R) \left[(1 - \eta) T^{\text{Room}} + T^{\text{RX}} \right] \mathbf{1} \Big\}
\end{aligned}
\tag{4.1}
$$

where $\boldsymbol{G}^{\text{ON}}$ is the dimensionless timestream of gain, k_{B} is the Boltzmann constant, and T^{RX} is the receiver noise temperature (other symbols are the same as those descrived in § 2.4).

The load measurement is generally carried out once at the reference RF frequency, $\nu^{\text{RF},0}$ between ON-point observations and thus represented as a D-dimension vector. For the convenience of matrix computation, however, we concatenate the load spectrum N times to make a $D \times N$ matrix (not a timestream) which is proportional to power, $\boldsymbol{P}^{\text{Load}}$:

$$
\begin{aligned}
\boldsymbol{P}^{\text{Load}} &= \boldsymbol{G}^{\text{Load}} k_{\text{B}} (1 + R) \left(T^{\text{Room}} + T^{\text{RX}} \right) \\
&= \big(\underbrace{\boldsymbol{g}^0 \boldsymbol{g}^0 \dots \boldsymbol{g}^0}_{N} \big) k_{\text{B}} (1 + R) \left(T^{\text{Room}} + T^{\text{RX}} \right)
\end{aligned}
\tag{4.2}
$$

where $\boldsymbol{g}^0$ is the dimensionless vector of gain at $\nu^{\text{RF}} = \nu^{\text{RF},0}$.

We note that the scalar value of an image rejection ratio, R, is intrinsically expressed as the timestream, $\boldsymbol{R} = \boldsymbol{G}^{\text{ON,i}} / \boldsymbol{G}^{\text{ON}}$, where $\boldsymbol{G}^{\text{ON,i}}$ is the dimensionless gain of the image sideband. Since $\boldsymbol{G}^{\text{ON,i}}$ is modulated reversely (see § 2.3), elements of $\boldsymbol{R}$ are expected not to be equal to R but have some variation around R. We can nevertheless express $\boldsymbol{R}$ as R because such variation is small enough ($< R < 1$) from the assumptions described above and the effect on intensity calibration is thus negligible. Moreover, the variation of the calibrated antenna temperature, $\boldsymbol{T}^{\text{calib}}$, is finally modeled and subtracted by the correlated noise re-

moval because the variation is expected to be correlated (one of the contributors of $\boldsymbol{E}^{\mathrm{C}}$ in equation 2.17). The detailed deformation of the observation equations are described in appendix B.

4.2 GAIN CORRECTION

The conventional non-FM position switching method assumes that the gain does not change between ON-point and load measurements (i.e., $\boldsymbol{G}^{\mathrm{ON}} \simeq \boldsymbol{G}^{\mathrm{Load}}$). In the FMLO method, however, the timestream of ON-point gain is modulated and thus has some dependences on observed frequencies. Before intensity calibration, it is necessary to model $\boldsymbol{G}^{\mathrm{ON}}$ by estimating frequency-modulation-dependent gain, $\boldsymbol{G}^{\mathrm{FM}}$, and dividing them from $\boldsymbol{G}^{\mathrm{ON}}$.

Since the axes of a timestream are as functions of IF frequency (frequency axis) and LO frequency (time axis), the modulation of a timestream is characterized by IF–LO frequency space, and each IF frequency channel may have some dependency on frequency modulation of LO. In the gain correction, we assume that the ON-point gain can be expressed as a product of an FM-dependent term, $\boldsymbol{G}^{\mathrm{FM}}$, and a FM-independent term, $\boldsymbol{G}^0$, at a reference frequency, $\nu^{\mathrm{RF},0}$:

$$\boldsymbol{G}^{\mathrm{ON}} = \boldsymbol{G}^{\mathrm{FM}} \boldsymbol{G}^0 = \big(\underbrace{\boldsymbol{g}_1^{\mathrm{FM}} \boldsymbol{g}_2^{\mathrm{FM}} \cdots \boldsymbol{g}_D^{\mathrm{FM}}}_{D} \big)^T \big(\underbrace{\boldsymbol{g}^0 \boldsymbol{g}^0 \cdots \boldsymbol{g}^0}_{N} \big) \tag{4.3}$$

where $\boldsymbol{g}_d^{\mathrm{FM}}$ represents the FM gain of each IF frequency channel. We hereafter call $\boldsymbol{G}^{\mathrm{FM}}$ "FM gain", and $\boldsymbol{G}^0$ "reference gain". In order to correct for FM gain, we have two choices of observing strategy:

1. To obtain an FM timestream of ON-point and a spectrum of the load without frequency modulation, where FM gain should be estimated from ON-point timestream itself, after subtracting atmospheric and astronomical signals.

2. To obtain FM timestreams of both ON-point and load, where FM gain can be estimated from the load measurements. In that case, observation equation of $\boldsymbol{P}^{\mathrm{Load}}$ is as follows:

$$\boldsymbol{P}^{\mathrm{Load}} = \boldsymbol{G}^{\mathrm{FM}} \boldsymbol{G}^0 k_{\mathrm{B}} (1 + R) \left(T^{\mathrm{Room}} + T^{\mathrm{RX}} \right) \tag{4.4}$$

44
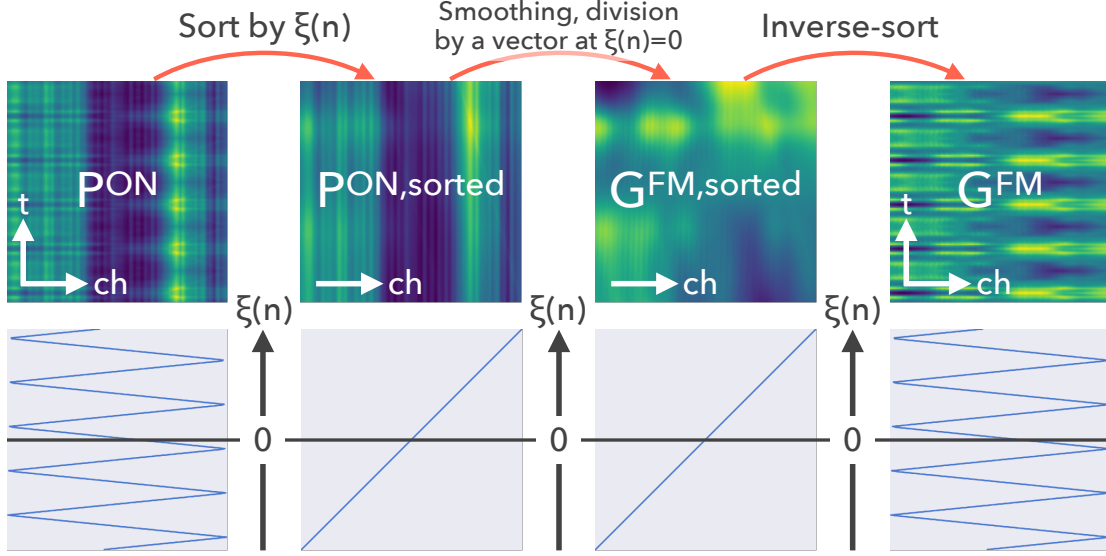
Figure 4.2: Schematic diagram of gain correction from a ON-point timestream itself. Top images represent modulated timestreams (frequency or IF axis is horizontal one), and bottom functions are FM corresponding each timestream. $\boldsymbol{P}^{\mathrm{ON}}$ is sorted according to its FM channel, $\xi(n)$. Then sorted ON-point timestream are smoothed by the Savitzky-Golay filter and each row vector is divided by one whose FM channel is $\xi(n) = 0$, which is equivalent to obtain a sorted FM gain, $\boldsymbol{G}^{\mathrm{FM,sorted}}$. We finally inverse-sort it to obtain the estimation of $\boldsymbol{G}^{\mathrm{FM}}$.

The latter is expected to be better estimation, however, we choose the former in on-site verification described in chapter 5 because load measurement with frequency modulation is not implemented yet in both Nobeyama 45 m and ASTE 10 m.

We hereafter describe how to estimate FM gain from an ON-point timestream itself (the first choice). Once we obtain $\boldsymbol{P}^{\mathrm{ON}}$, we rearrange its spectra so that their incident FM channels, $\xi(n)$, are sorted in ascending order. Then we apply interpolation to each row vector of it to make a sorted and resampled ON-point timestream along FM channels, $\boldsymbol{P}^{\mathrm{ON,sorted}}$, as a $D \times M$ matrix. M is the peak-to-peak number of FM channels obtained during an FMLO observation; for example, if we obtain an ON-point timestream whose FM channel reaches -1024 ch as the mimimum value and +1024 ch as the maximum value, M will be 2049 ($= 2048 - (-2048) + 1$). Now we apply the Savitzky-Golay filter (Savitzky & Golay, 1964), one of the smoothing filters, to each row of $\boldsymbol{P}^{\mathrm{ON,sorted}}$ to model a

smoothed gain curve of each IF channel. We choose window length, l_{window}, and order of polynominal of the Savitzky-Golay filter, N_{order}, so that the resulting model is smooth enough to represent overall features of the gain curve but not to fit noisy features (i.e., overfitting). Finally we estimate a $D \times N$ smoothed timestream, $\boldsymbol{P}^{\text{ON,smoothed}}$, from the gain curve of each IF channel; each column vector of $\boldsymbol{P}^{\text{ON,smoothed}}$ is filled with the values of each gain curve at corresponding $\xi(n)$. The FM gain is thus derived by the following equation:

$$\boldsymbol{G}^{\text{FM}} = \boldsymbol{P}^{\text{ON,smoothed}}/\boldsymbol{P}^{\text{ON,smoothed},0} \tag{4.5}$$

where $\boldsymbol{P}^{\text{ON,smoothed},0}$ is a $D \times N$ matrix each column vector of which is filled with that of $\boldsymbol{P}^{\text{ON,smoothed}}$ at $\xi(n) = 0$ (i.e, reference frequecy, $\nu^{\text{RF},0}$). Note that we cannot derive the reference gain because $\boldsymbol{G}^0$ is coupled with $\boldsymbol{T}$-related terms in the equation 4.1 and thus we do not know the absolute value of it. Estimating $\boldsymbol{G}^{\text{FM}}$ for the second choice is the same procedures as the first one. The schematic diagram of gain correction is illustrated in figure 4.2.

Finally we obtain the FM-gain-correcred timestreams of ON-point and load, respectively:

$$\boldsymbol{P}^{\text{ON,corr}} \equiv \boldsymbol{P}^{\text{ON}}/\boldsymbol{G}^{\text{FM}} \tag{4.6}$$

$$\boldsymbol{P}^{\text{Load,corr}} \equiv \begin{cases} \boldsymbol{P}^{\text{Load}}/\boldsymbol{G}^{\text{FM}} & (\text{with FM measurement}) \\ \boldsymbol{P}^{\text{Load}} & (\text{without FM measurement}) \end{cases} \tag{4.7}$$

4.3 Intensity calibration

After the FM gain correction, we proceed to the absolute intensity calibration to obtain a modulated timestream of an antenna temperature in the T_{A}^* scale. We can express it in the same manner as the one-load chopper-wheel calibration using FM-gain-corrected timestreams:

$$\boldsymbol{T}^{\text{Calib}} \equiv (1+R)T^{\text{Atm}} \frac{\boldsymbol{P}^{\text{ON,corr}} - \text{med}_n(\boldsymbol{P}^{\text{ON,corr}})}{\boldsymbol{P}^{\text{Load,corr}} - \text{med}_n(\boldsymbol{P}^{\text{ON,corr}})} \tag{4.8}$$

where $\mathrm{med}_n : \boldsymbol{X} \to \boldsymbol{X}$ is a mapping which computes the median of a given matrix along the time axis with keeping its shape:

$$\mathrm{med}_n(\boldsymbol{X})_{dn} = \mathrm{median}(\{x_{d1}, x_{d2}, \ldots, x_{dN}\}) \tag{4.9}$$

The term of $\mathrm{med}_n(\boldsymbol{P}^{\mathrm{ON,corr}})$ can provides the estimated timestream of OFF-point measurements without time vairation. Under the assumptions described above, this yields a modulated timestream of antenna temperatures similar to equation 2.14:

$$\begin{aligned}
\boldsymbol{T}^{\mathrm{Calib}} \simeq{}& \boldsymbol{T}^{\mathrm{NC}}\boldsymbol{e}^{-\bar{\boldsymbol{\tau}}} + T^{\mathrm{Atm}}(\boldsymbol{1} - \boldsymbol{e}^{-\bar{\boldsymbol{\tau}}}) \\
&+ R\left[\boldsymbol{T}^{\mathrm{NC,i}}\boldsymbol{e}^{-\bar{\boldsymbol{\tau}}^{\mathrm{i}}} + T^{\mathrm{Atm}}(\boldsymbol{1} - \boldsymbol{e}^{-\bar{\boldsymbol{\tau}}^{\mathrm{i}}})\right]
\end{aligned} \tag{4.10}$$

where $\bar{\boldsymbol{\tau}}^{(\mathrm{i})*}$ is the median-subtracted opacity of atmosphere:

$$\bar{\boldsymbol{\tau}}^{(\mathrm{i})} \equiv \boldsymbol{\tau}^{(\mathrm{i})} - \mathrm{med}_n(\boldsymbol{\tau}^{(\mathrm{i})}) \tag{4.11}$$

A difference of equation 4.10 from equation 2.14 is that the correlated components of $\boldsymbol{T}^{\mathrm{C(,i)}}$ are already subtracted by $\mathrm{med}_n(\boldsymbol{P}^{\mathrm{ON,corr}})$. Another different point is that the opacity terms of $\bar{\boldsymbol{\tau}}^{(\mathrm{i})}$ is composed of $\boldsymbol{\tau}^{\mathrm{NC(,i)}}$ and median-subtraced $\boldsymbol{\tau}^{\mathrm{C(,i)}}$, which assumes that $\bar{\boldsymbol{\tau}}^{(\mathrm{i})}$ fluctuate around zero. After correlated component removal (§ 4.4), however, this yields the same "clean"ed timestream, $\boldsymbol{T}^{\mathrm{Clean}}$, as that described in equation 2.18. The detailed deformation from equation 4.8 to 4.10 is described in the appendix B.

4.4   Correlated component removal[†]

We estimate and subtract correlated components by principal components analysis (PCA) with some modifications. PCA is originally an orthogonal matrix

---

[*]we hereafter express $\boldsymbol{X}$ and $\boldsymbol{X}^{\mathrm{i}}$ as $\boldsymbol{X}^{(\mathrm{i})}$ if they are not necessary to be distinguished

[†]within the section, expressions of matrix product ($\boldsymbol{XY}$, for example) are intended to compute dot product, not element-wise one. we also note that we use a name of correlated "component" removal (not noise) because not only noise but also correlated emission such as continuum are modeled and removed with this signal processing

transformation which converts an observed (possibly) correlated matrix, $\boldsymbol{X}$ (D variables and N samples, for example) into linearly non-correlated one, $\boldsymbol{C}$:

$$\boldsymbol{X} = \boldsymbol{PC} \quad \Leftrightarrow \quad \boldsymbol{C} = \boldsymbol{P}^T \boldsymbol{X} \tag{4.12}$$

where $\boldsymbol{P}$ is a $D \times \min(D, N)$ orthogonal matrix of basis vectors as a transformation matrix which is the set ot eigenvectors of the covariance matrix of $\boldsymbol{X}$. $\boldsymbol{C}$ is a $\min(D, N) \times N$ matrix called principal components because it is defined such that the first principal component has the largest variance and subsequent ones have the second, third, … largest variances, and are orthogonal to the other components. PCA is widely used to, for example, extract features of data with fewer ($< D$) variables, or visualize high demensional data as a two- or three-dimensional plot (Jolliffe, 2002).

From the viewpoint of correlated component removal, PCA is an effective way of estimating such components because it is one of low-rank approximation methods of a matrix. Correlated components can be modeled as a reconstruction of $\boldsymbol{X}$ with only $K(< \min(D, N))$ largest principal components and eigenvectors:

$$\boldsymbol{X}^{\mathrm{C}} \simeq \boldsymbol{P}_{:,:K} \boldsymbol{C}_{:K,:} \tag{4.13}$$

where $\boldsymbol{P}_{:,:K}$ is a $D \times K$ matrix of K largest eigenvectors and $\boldsymbol{C}_{:K,:}$ is a $K \times N$ matrix of corresponding principal components. By definition, the rank of $\boldsymbol{X}^{\mathrm{C}}$ is K. Since non-correlated components are expected to have smaller and uniform variances in the D-dimensional space, such components shall remain in the rest principal components:

$$\boldsymbol{X}^{\mathrm{NC}} \simeq \boldsymbol{X} - \boldsymbol{X}^{\mathrm{C}} \tag{4.14}$$

There exist, however, some issues when we apply PCA to the correlated component removal in the FMLO method: It is possible to be some errors between the estimated correlated components and "true" ones because PCA is easily affected by strong line emission from astronomical source and/or the sky, if any, which yields negative sidelobe-like features around strong lines in a final spectrum (see

figure 5.9 and 5.10, for example). This is the case even with an observation of faint line emission such as extragalactic objects because there may exist line emission from the Earth's atmosphere such as ozone molecule, which has much broader line shape caused by pressure broadening (FWZI $\gtrsim$ 1000 km/s, see figure 4.5, for example) than typical one from extragalactic objects (FWZI $\sim$ 500 km/s). Another issue is that it is arbitrary for users to choose the number of principal components, K, which is used for the reconstraction of correlated components. We should find the optimal number of K when we reconstruct $\boldsymbol{X}^{\mathrm{C}}$: contribution from correlated components may remain in $\boldsymbol{X}^{\mathrm{NC}}$ if K is much smaller or $\boldsymbol{X}^{\mathrm{C}}$ may model astronomical signals (and even non-correlated noises!) if K is much larger than the optimal one.

In the correlated component removal in the FMLO method, we introduce the weighted principal component analysis by expectation maximization (EM) algorithm (EMPCA; Bailey (2012)) which enables us to minimize the effect of strong line emission by de-weighting elements contaminated by such emission in a modulated timestream when estimating $\boldsymbol{P}$ and $\boldsymbol{C}$. Computing PCA by the EM algorithm approach is originally discussed by Roweis (1998), where an unweighted version is proposed for interpolating missing data. Bailey (2012) presents the EMPCA for noisy data and/or data some elements of which are missing, where noisiness and/or data missing are expressed as a weight matrix, $\boldsymbol{W}$, which has the same dimension as the data matrix. In the classical PCA minimizes the following quantity of χ^2:

$$\chi^2 = \sum_{d=1}^{D} \sum_{n=1}^{N} (\boldsymbol{X} - \boldsymbol{P}\boldsymbol{C})_{dn}^2 \tag{4.15}$$

while the EMPCA of Bailey (2012) tries to minimize χ^2 containing $\boldsymbol{W}$:

$$\chi^2 = \sum_{d=1}^{D} \sum_{n=1}^{N} \boldsymbol{W}_{dn} (\boldsymbol{X} - \boldsymbol{P}\boldsymbol{C})_{dn}^2 \tag{4.16}$$

The actual algorithm of the EMPCA is iterative estimating processes of $\boldsymbol{C}$ and $\boldsymbol{P}$ alternatingly, called E-step and M-step: At expectation step (E-step, hereafter) of the m-th iteration, it solves $\boldsymbol{C}^{(m)}$ from $\boldsymbol{X}$, $\boldsymbol{W}$, and $\boldsymbol{P}^{(m-1)}$. At maximization-
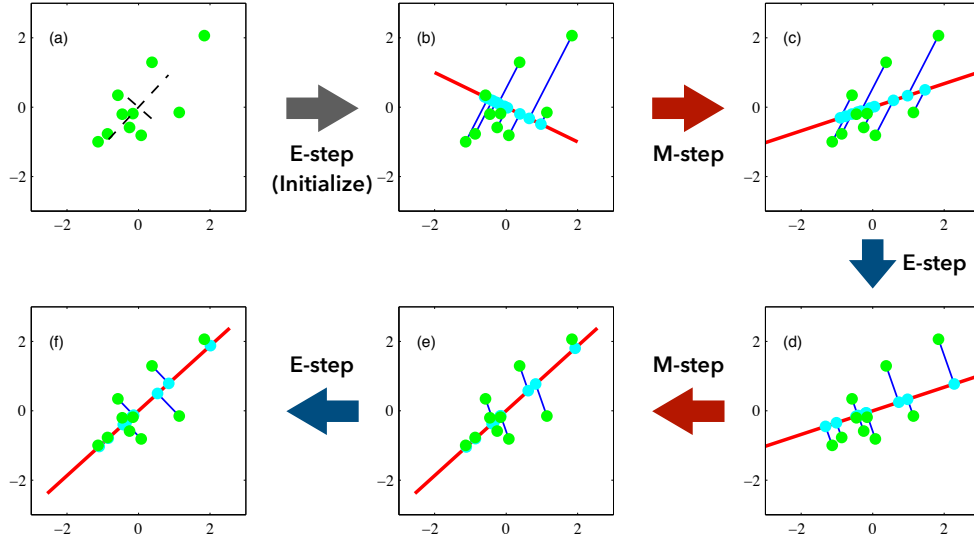
Figure 4.3: Schematic diagrams of PCA using EM algorithm in the case of $D = 2$ (modified figure 12.12 of Bishop (2006)), where 2D data points are expressed as green dots and the true directions of two eigen vetrors, $\boldsymbol{P}$, calculated by a normal PCA are expressed as orthogonal dotted lines in the panel (a). At each panel, the direction of 1st (most dominant) principal compoent is expressed as a red line like a solid bar, and that of 2nd one of each data point is expressed as a blue line like a spring. The E-step (c to d, for example) estimates the coefficients of each data point, $\boldsymbol{C}$, with fixed $\boldsymbol{P}$ so that red and blue lines are orthogonal. This is like connecting springs from knots to a bar fixed by hand. The subsequent M-step (d to e, for example) then estimates the direction of eigenvectors, $\boldsymbol{P}$, with fixed direction of $\boldsymbol{C}$ so that the sum of length of blue lines is minimized. This is like releasing the bar after springs connected, and re-fix it at a new direction so that the sum of tension of springs is minimized (i.e., most relaxed). After repeating some steps by turns, $\boldsymbol{P}$ (and $\boldsymbol{C}$, of course) is finally conveged at the directions closest to the intrinsic ones. The EM-PCA with weights can be interpreted that they have different spring constants according to the weight values.

step (M-step, hereafter) of the m-th iteration, it then solves $\boldsymbol{P}^{(m)}$ from $\boldsymbol{X}$, $\boldsymbol{W}$, and $\boldsymbol{C}^{(m)}$. After several iterations and both $\boldsymbol{C}$ and $\boldsymbol{P}$ are converged, correlated components are estimated as follows:

$$\boldsymbol{X}^{\mathrm{C}} \simeq \boldsymbol{P}^{(m)}_{:,:K} \boldsymbol{C}^{(m)}_{:K,:} \tag{4.17}$$

These EM steps of PCA is sometimes compared to determining the direction of a bar conneceted to data points by springs as illustrated in figure 4.3. While the springs have the same spring constant in a normal PCA, the EMPCA can be interpreted that they have different spring constants according to the weight

values. In the following subsections, we briefly review the E- and M-steps of the EMPCA using the same notations as used in this thesis. We also discuss how to determine $\boldsymbol{W}$ and K from a timestream.

4.4.1 EMPCA: E-step

At E-step of the m-th iteration, we estimate $\boldsymbol{C}^{(m)}$ from $\boldsymbol{X}$, $\boldsymbol{W}$, and $\boldsymbol{P}^{(m-1)}$. For each column of $\boldsymbol{C}$, we solve it by the following linear equation using weighted $\boldsymbol{X}_{:,n}$ and $\boldsymbol{P}$

$$\boldsymbol{\Psi}^n \boldsymbol{X}_{:,n} = \boldsymbol{\Psi}^n \boldsymbol{P}^{(m-1)} \boldsymbol{C}^{(m)}_{:,n} \tag{4.18}$$

where $\boldsymbol{\Psi}^n$ is a diagonal matrix of $\boldsymbol{W}_{:n}$:

$$\boldsymbol{\Psi}^n = \begin{pmatrix} \boldsymbol{W}_{1n} & & & \\ & \boldsymbol{W}_{2n} & & \\ & & \ddots & \\ & & & \boldsymbol{W}_{Dn} \end{pmatrix} \tag{4.19}$$

If $m = 1$, $\boldsymbol{P}^{(m-1)}$ is a random orthognal matrix calculated by the Gram-Schmidt process. The linear equation itself can be easily solved by some linear algebra package for a programming language. In the data analysis package for the FMLO method (FMFlow; see appendix C), we use `numpy.linalg.solve` function powered by the NumPy, a fundamental package for scientific computing with Python.

4.4.2 EMPCA: M-step

In a M-step of m-th iteration, we estimate $\boldsymbol{P}^{(m)}$ from $\boldsymbol{X}$, $\boldsymbol{W}$, and $\boldsymbol{C}^{(m)}$. For each column vector of $\boldsymbol{P}$, it is composed of the following three substeps to solve:

1. Estimate each element of the k-th column vector, $\boldsymbol{P}_{dk}$ $(1 \leq d \leq D)$ by the following equation using weighted $\boldsymbol{X}$ and $\boldsymbol{C}$:

$$\boldsymbol{P}_{dk} = \frac{\sum_{n=1}^{N} \boldsymbol{W}_{dn} \boldsymbol{X}_{dn} \boldsymbol{C}_{kn}}{\sum_{n=1}^{N} \boldsymbol{W}_{dn} \boldsymbol{C}_{kn} \boldsymbol{C}_{kn}} \tag{4.20}$$

2. Subtract the contribution of the k-th principal component from $\boldsymbol{X}$ in-place:

$$\boldsymbol{X} \leftarrow \boldsymbol{X} - \boldsymbol{P}_{:,k} \otimes \boldsymbol{C}_{k,:} \tag{4.21}$$

where $\otimes$ is an operator of direct (Cartesian) product.

3. Repeat 1 and 2 to solve for the next eigenvector $\boldsymbol{P}_{:,k+1}$ until $k+1$ reaches the number of eigenvectors K.

Whether or not $\boldsymbol{P}$ and $\boldsymbol{C}$ are converged compared to the previous ones is checked by calculating a Frobenius norm[‡] of $|(\boldsymbol{X}^{\mathrm{C}(m)} - \boldsymbol{X}^{\mathrm{C}(m-1)})/\boldsymbol{X}^{\mathrm{C}(m-1)}|_F$, which indicates the total variation between them. We stop the iteration if it is smaller than 10^{-4}, about 0.1 % of total variation as a practical value.

We note that these steps require element-wise operation in a programming language. In the `FMFlow`, we use the NumPy (van der Walt et al., 2011) with Numba (Lam et al., 2015), a just-in-time compiler which compiles a Python code to native machine instructions to achieve similar in performance to C, C++ and Fortran.

4.4.3 CHOOSING WEIGHTS FOR EMPCA

As is described in § 4.5, we estimate the correlated and non-correlated components, atmospheric and astronomical specral lines by the iterative processes (not mentioning the one above) in a pipeline in order to minimize the errors of each estimate. In the pipeline at n-th iteration, we can calculate the weight $\boldsymbol{W}^{(n)}$ which will be used for the EMPCA at $(n+1)$-th iteration, by the estimated spectrum of atmospheric line emission, $\boldsymbol{s}^{(n)}$. The conversion method from $\boldsymbol{s}$ to $\boldsymbol{W}$ must meet the following conditions:

1. The weight value must be 1 if no signal and reach to 0 if signal becomes larger.

2. If two values of signal are equal but noise levels are not, the weight value must be smaller with the one whose signal-to-noise ratio is larger.

[‡]a Frobenius norm of a matrix, $\boldsymbol{X}$, is expressed as $||\boldsymbol{X}||_F = \sqrt{\sum_d^D \sum_n^N |\boldsymbol{X}_{dn}|^2} = \sqrt{\mathrm{tr}(\boldsymbol{X}^*\boldsymbol{X})}$, where $\boldsymbol{X}^*$ is a adjoint matrix of $\boldsymbol{X}$
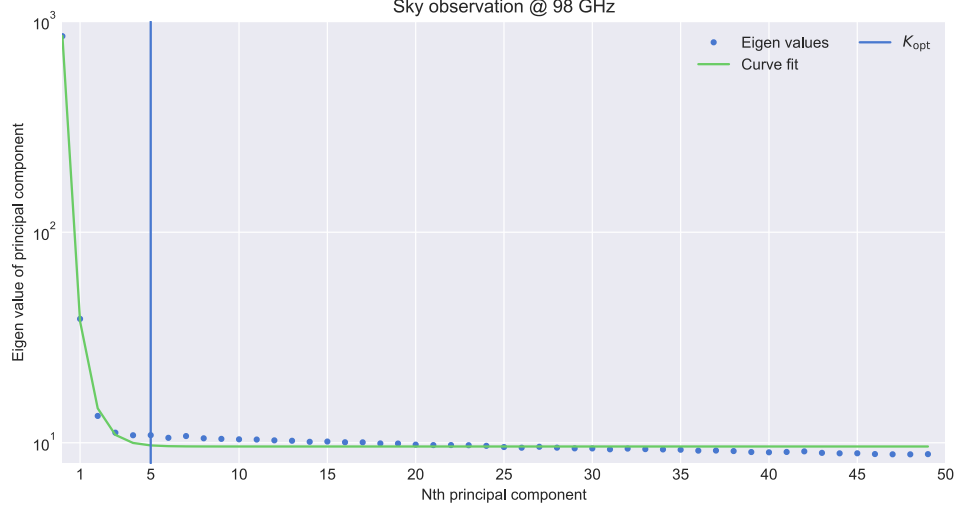
Figure 4.4: An example of curve fit of exponential-and-constant function to the logarithmic eiven values. The data are the same as that used in figure 5.11. The blue vertical line indicates the optimal number of principal components as a result of the curve fit.

For these reasons, we use the following equation to calculate weight values:

$$w = 2^{-\left|\frac{s/n}{\theta_{\mathrm{half}}}\right|} \tag{4.22}$$

where s and n are signal and noise values of a RF channel of difference between the n-th and $(n-1)$-th iterations, $\tilde{\boldsymbol{s}}^{(n)} - \tilde{\boldsymbol{s}}^{(n-1)}$. θ_{half} is the signal-to-noise threshold at which the weight value reaches $1/2$. This means that RF channels are more deweigheted where differences of spectra between the n-th and $(n-1)$-th iterations are large at the beginning of iterative processes, and most of channels are no longer deweighted at the end of them. In chapter 5, we use $\theta_{\mathrm{half}} = 10$ as a practical value.

4.4.4 CHOOSING OPTIMAL NUMBER OF PRINCIPAL COMPONENTS

As mentioned above, determining the number of principal components to be used for the reconstruction of correlated components in each iteration is important to isolate correlated and non-correlated component properly and converge the iterative process quickly. Since computing PCA by the EM algorithm is eas-

ily applicable to the PCA with probabilistic interpretation (PPCA; Tipping & Bishop (1999)), one can determine the optimal number of principal components by Bayesian model selection proposed by Minka (2001) if we could compute *all* eigen values of D, the number of spectrometer channels. In the actual signal processing of the FMLO method, however, computing all D eigen values and vectors by the EMPCA is not realistic because D easily reaches more than 10^3 in a typical spectrometer (for example, $D = 1024, 2048$ at ASTE 10 m and Nobeyama 45 m, respectively in this thesis), which takes more than several minutes to compute the EMPCA in the case of $K = D$ (computation time will be further discussed in chapter 7). Another issues is that the modulated bright atmospheric line emission in a timestream may contribute a large amount of principal components at the beginning of iterative processes, which may mislead to estimate the "true" optimal number of principal components to be removed.

For the simple and fast determination of principal components at each iteration, we conduct a curve fit of exponential-and-constant fuction, $\log \sigma_k^2 = A \exp(-Bk) + C$, to the k-th logarithmic eigen value of eigenvector, σ_k^2, Then we derive the half-valued period, $k_{\mathrm{half}} \equiv \ln 2 / B$, at which the exponential contribution in eigen values is reduced by half. Finally, we choose the optimal number of principal components as $K_{\mathrm{opt}} = 7 k_{\mathrm{half}}$, at which the exponential contribution in eigen values is $< 2^{-7} (\sim 1\%)$ of the first one. In other words, the eigen value reaches almost constant ($\sigma_k^2 \sim 10^C$) at K_{opt}, which suggests that contribution only from white noise dominates for K_{opt}-th or minor principal components. An example of curve fit is demonstrated in figure 4.4. As is demonstrated in chapter 5, we reveal that only a few principal components at the top is larger than the others by an order of magnitude in the timestreams of the FMLO observation, which suggests that they would have the most contribution of correlated components if we could calculate the all D principal components. We note that it is necessary to set the maximum number of principal components calculated by the EMPCA, K_{max}, when we conduct a data reduction ($K_{\mathrm{opt}} < K_{\mathrm{max}} \ll D$ will be expected). This means we need to know K_{opt} as a prior information and it is thus necessary to measure the typical value of K_{opt} at, for example, the beginning of observation seasons of a telescope.

4.5 End-to-end pipeline algorithm

After correlated component removal and obtaining the cleaned timestream, $\boldsymbol{T}^{\mathrm{Clean}}$, we can make a spectrum (single point observation) or a map (on-the-fly observation) as a final product by an integration process described in § 2.5. With a single process, however, there might be some errors between estimates and "true" values of the final product because the estimate of correlated components is affected by strong line emission from astronomical source and/or the sky, even if we use the EMPCA, which yields negative sidelobe-like features around strong lines in the final product.

The subsequent iterative processes can minimize the errors (e.g., Chapin et al. (2013)): Each term is re-estimated without including the other terms, which minimizes the effect from them. For example, when we re-estimate the correlated components by the EMPCA, we exclude the strong line emission by subtracting the modulated signal of it from the calibrated timestream, $\boldsymbol{T}^{\mathrm{Calib}}$, before we re-conduct the EMPCA. It is therefore necessary to "model"[§] the astronomical and atmospheric signals from the cleaned timestream of the n-th iteration, $\boldsymbol{T}^{\mathrm{Cleaned}}$, for the $(n{+}1)$-th process. We present how to model atmospheric and astronomical line emission. Then we introduce the end-to-end iterative algorithm for a sigle-pointing spectral line and mapping observations of the FMLO method which is used as a pipeline for the data reduction described in chapter 5 and 6.

4.5.1 Modeling atmospheric line emission

The thermal emission (and also absorption) of the Earth's atmosphere can be modeled by radiative transfer computations assuming a sequence of hydrostatic planar layers of the atmosphere each of which has its own pressure, temperature, and column density of a molecule of interest. We use a tool for radiative transfer compuations (`am` Atmospheric Model; Paine (2017)) and a layer model provided by `am` for the calculation of atmospheric spectral line such as ozone. As the molecule of ozone is only dominant and detected at the observed frequency bands and the

---

[§]the meaning of "model" here is not to estimate the true signals but to make a best-effort and noise-free spectrum or map at each iteration for the next one
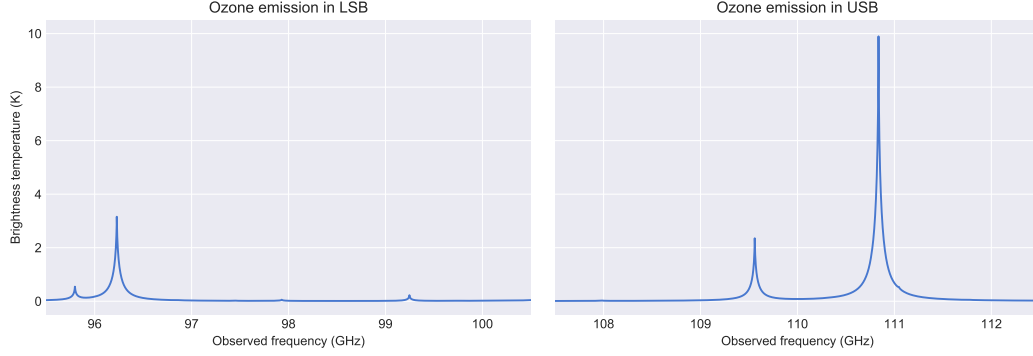
Figure 4.5: Spectral line emission of ozone molecule in the atmosphere calculated by `am` observed at (left) LSB and (right) USB of Nobeyama 45 m. Only radiative transfer of ozone is considered. The pressures, temperatures at the bottom of each layer, column densities of ozone of each layer are listed in table 4.1. Other parameters used for the calculation are as follows: zenith angle: 0 deg, background temperature: 2.7 K (that of cosmic microwave background; CMB).

achieved sensitivity of the FMLO observations during the commissioning, we thus focus on modeling and subtracting the ozone spectral lines in chapter 5 and 6. It is possible, however, to detect minor (and thus weaker) molecular species such as CO, CO_2, NO_x in the future observations where we reach the sensitivity better by more than an order of magnitude. Although the spectral lines of these molecules do not contribute much to the absorption of astronomical signals (i.e., $e^{-\boldsymbol{\tau}^{\mathrm{NC}}}$), it is necessary to model and subtract it to make a final product. This will be further discussed in chapter 7.

With the actual modeling of the atmospheric line emission from a cleaned timestream, however, we do not obtain information of actual values of parameters such as pressure, temperature, and ozone's column density of each layer apart from an FMLO observation, which means that we cannot solve the radiative transfer equations. We therefore conduct a linear fit of modeled ozone spectra of each layer to the obtained final spectrum or map, which are pre-computed by `am` using typical values of parameters of each layer. In the case of modeling ozone spectral lines from a final FMLO spectrum, $\tilde{\boldsymbol{s}}$, for example, we pre-compute to obtain typical ozone spectra of each layer, $\tilde{\boldsymbol{s}}_n^{\mathrm{ozone}}$, and derive coefficients of each layer, c_n,
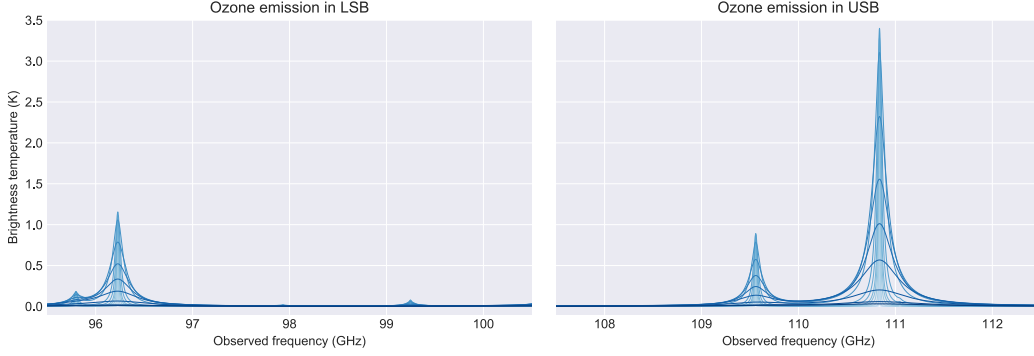
Figure 4.6: Spectral line emission of ozone molecule in the atmosphere calculated by `am` observed at (left) LSB and (right) USB of Nobeyama 45 m. Unlike figure 4.5, this figure shows the spectra considering radiative transfer of a single layer as listed in table 4.1. Because line width of ozone depends on the pressure at the altitude of 16–80 km/s, spectra of broader line width are from lower layers. Other parameters used for the calculation are same as described in figure 4.5.

so that they minimize χ^2 expressed in the following equation:

$$\chi^2 = \sum_{d=1}^{\tilde{D}} \left(\tilde{s} - \sum_{n=1}^{N_{\text{layer}}} c_n \tilde{s}_n^{\text{ozone}} \right) \tag{4.23}$$

where N_{layer} is the number of atmospheric layers assumed for the modeling. Figure 4.5 and 4.6 show the computed ozone spectra by solving the radiative transfer equations and pre-computed ones of each layer by `am` at the observed frequency bands of the Nobeyama 45 m telescope. The values of parameters used for the computation are listed in table 4.1. In the case of modeling ozone spectral lines from a final FMLO map, $\tilde{M}$, we can assume that the ozone molecule and thus the intensity of its spectral line is uniformly distributed in the whole mapping region if telescope's elevation does not change largely during an observation. We then make a mean spectrum of $\tilde{M}$ along spatial axes, which does not only improve the signal-to-noise ratio but also minimize the effect of astronomical signals (expected to be ununiformly distributed), and fit ozone spectra to the mean spectrum to derive the coefficients.

Finally, we create the model spectrum or map of the atmosphere as $\tilde{s}^{\text{model}} = \sum_n c_n \tilde{s}_n^{\text{ozone}}$ or $\tilde{M} = \sum_n c_n \tilde{M}_n^{\text{ozone}}$ and the model timestream of it by a projection

Figure 4.7: An example of the $n\sigma$-cutoff method, where a spectrum from an FMLO observation and a model as a result of 3σ-cutoff (i.e., $\theta_{\text{cutoff}} = 3$) are expressed as blue and green lines. The estimated 1σ noise level is indicated as a gray line. The negative sidelobe features at the both sides of a line are aftificial ones due to improper estimate of correlated component removal and thus should not be modeled as signals. The $n\sigma$-cutoff can eliminate such features well, however, faint outer skirts between 0 to 3σ are not modeled. We denomstrate that such faint features are also successfully reproduced in after several iterative processes in § 5.3.4.

of it to an ON-point timestream (see § 2.5 for the "projection").

4.5.2 Modeling astronomical line emission

Unlike atmospheric line emission, we do not have any models to be fitted to the final product because it is literally unknown and what we want to know after the signal processing. In the case of "model"ing such spectral lines from both spectrum and map, however, we conduct the $n\sigma$-cutoff method to make an astronomical model eliminating noises and negative sidelobe-like features: If we obtain a spectrum as a final product, for example, then the model is calculated by the following equation:

$$\tilde{\boldsymbol{s}}^{\text{model}} = \begin{cases} \tilde{\boldsymbol{s}} & (\tilde{\boldsymbol{s}} > \theta_{\text{cutoff}}\sigma) \\ 0 & (\text{otherwise}) \end{cases} \tag{4.24}$$

where σ is a standard deviation of line-free channels of the final spectrum, and $\theta_{\text{cutoff}}(> 0)$ is a threshold value of signal-to-noise. In chapter 5, we use $\theta_{\text{cutoff}} = 3$ as a practical value. In the case of astronomical line absorption, the first condition

of equation 4.24 will be modified as $\tilde{\boldsymbol{s}} < -\theta_{\mathrm{cutoff}}\sigma$. Note that a caveat of $n\sigma$-cutoff approach is that not only negative sidelobe-like fetures but also line emission below $n\sigma$ is also excluded from a model. In chapter 5, we confirm that such a weak emission features next to a modeled line (faint skirt of a spectral line, for example) will be reproduced in subsequent iterative processes. But for such emission of isolation (a line whose peak intensity is $< n\sigma$, for example), negative sidelobe-like features might be remaining in the last iteration, although such features are usually negligible for such weak emission.

4.5.3 Time-chunk process

So far the signal processing of a timestream assumes that the condition of atmosphere and a telescope do not change largely. This means that the eigenvectors, $\boldsymbol{P}$, of correlated components are regarded to be constant during an observation. In the case of long-time observations such as an FMLO observation of large map, however, telescope's elevation and thus intensity of atmospheric line emission may change largely during an observation because of an elevation dependency of air mass ¶ (this also changes $\boldsymbol{P}$). In order to properly model such time-varying correlated components and atmospheric line emission, we split a timestream data into chunks of several minutes (several hundred samples in a chunk) and conduct correlated component removal and modeling atmospheric line emission described above independently between chunks. This time-chunk process will be demonstrated as FMLO mapping observations in § 6.2.

4.5.4 Pipeline algorithm

Finally we present the end-to-end pipeline algorithm for spectral or mapping FMLO observarions. Algorithm 1 shows the overall pipeline used for the following data reduction of FMLO observations. Because the most part of the algorithm is common in both spectral and mapping observations, the algorithm we show below is the one assuming the following conditions:

¶the path length for light relative to that at the zenith ($\sec Z$, where Z is zenith angle).

- The algorithm is for a spectral line observarion of the FMLO method. The differences from that for mapping observation are the methods of integration/projection and modeling atmospheric/astronomical lines. Another one is how to subtract astronomical model from a timestream. This is commented in the algorithm 3.

- We estimate a frequency modulation gain, $\boldsymbol{G}^{\mathrm{FM}}$, from a timestream of ON-point measurement itself (the first choice as we describe in § 4.2)

- No strong line emission from the atmosphere and astronomical target leaks from the image sideband (i.e., the terms of the sideband in equation 4.10 is negligible)

- The astronomical lines do not completely overlap with those from the atmosphere (i.e., assuming equation 2.20)

- No time-chunk processes are described for clarity in the algorithm (because it makes nested for-loop and thus simply makes worse the readability of the algorithm)

- 293 K is used for the room temperature.

At the beginning of the algorithm (L.1), we read a timestream of ON-point and a matrix of the load from an observed data (as is provided with a FITS file format). Then we set several parameters for each modeling of atmospheric, astronomical line emission, and FM gain described above (L.2). One new parameter, ε, is used for a convergence check of each model: Once we obtain a new estimate in an iterative process ($\boldsymbol{G}^{\mathrm{FM}}_{\mathrm{new}}$, for example), whether or not it is converged compared to the previous one, $\boldsymbol{G}^{\mathrm{FM}}$, is checked by calculating a Frobenius norm of $|(\boldsymbol{G}^{\mathrm{FM}}_{\mathrm{new}} - \boldsymbol{G}^{\mathrm{FM}})/\boldsymbol{G}^{\mathrm{FM}}|_F$ which indicates the total variation between them. If the value of a norm is below ε, we then stop the iterative process.

We then create a calibrated timestream (L.8, although FM gain is not corrected in the first outer loop), and then model spectral line emission from the sky (L.10) and an astronomical target (L.11) by inner loops of iterative processes as described in algorithm 2 and 3. We note that the notations of $\boldsymbol{T}^{\mathrm{Atm}}$, $\boldsymbol{T}^{\mathrm{Ast}}$ used in these algorithm are different from that described in chapter 2 (in this section we use these notations as "model"s). The algorithms 2 and 3 are almost similar

Algorithm 1 End-to-end pipeline to estimate $\boldsymbol{T}^{\mathrm{A}^*}$

1: Take $\boldsymbol{P}^{\mathrm{ON}}, \boldsymbol{P}^{\mathrm{Load}}, \boldsymbol{1}, \boldsymbol{0}$ $(\in \Re^{D \times N})$
2: Take $K_{\mathrm{max}}, \theta_{\mathrm{half}}, \theta_{\mathrm{cutoff}}, l_{\mathrm{window}}, N_{\mathrm{order}}, \varepsilon$
3:
4: $\boldsymbol{G}^{\mathrm{FM}} \leftarrow \boldsymbol{1}$
5: **loop**
6:      $\boldsymbol{P}^{\mathrm{ON,corr}} \leftarrow \boldsymbol{P}^{\mathrm{ON}}/\boldsymbol{G}^{\mathrm{FM}}$
7:      $\boldsymbol{P}^{\mathrm{OFF}} \leftarrow \mathrm{med}_n\left(\boldsymbol{P}^{\mathrm{ON,corr}}\right)$ $\triangleright$ See equation 4.9
8:      $\boldsymbol{T}^{\mathrm{Calib}} \leftarrow 293 \cdot (\boldsymbol{P}^{\mathrm{ON,corr}} - \boldsymbol{P}^{\mathrm{OFF}})/(\boldsymbol{P}^{\mathrm{Load}} - \boldsymbol{P}^{\mathrm{OFF}})$ $\triangleright$ See equation 4.8
9:
10:     $\boldsymbol{T}^{\mathrm{Atm}} \leftarrow \mathrm{AtmModel}\left(\boldsymbol{T}^{\mathrm{Calib}};\ K_{\mathrm{max}}, \theta_{\mathrm{half}}, \varepsilon\right)$ $\triangleright$ See algorithm 2
11:     $\boldsymbol{T}^{\mathrm{Ast}} \leftarrow \mathrm{AstModel}\left(\boldsymbol{T}^{\mathrm{Calib}}, \boldsymbol{T}^{\mathrm{Atm}};\ K_{\mathrm{max}}, \theta_{\mathrm{cutoff}}, \varepsilon\right)$ $\triangleright$ See algorithm 3
12:     $\boldsymbol{T}^{\mathrm{Res}} \leftarrow \boldsymbol{T}^{\mathrm{Calib}} - \boldsymbol{T}^{\mathrm{Atm}} - \boldsymbol{T}^{\mathrm{Ast}}$
13:
14:     $\boldsymbol{P}^{\mathrm{Res}} \leftarrow \boldsymbol{G}^{\mathrm{FM}}\left((\boldsymbol{T}^{\mathrm{Res}}/293)\boldsymbol{P}^{\mathrm{Load}} + (1 - \boldsymbol{T}^{\mathrm{Res}}/293)\boldsymbol{P}^{\mathrm{OFF}}\right)$
15:     $\boldsymbol{G}^{\mathrm{FM}}_{\mathrm{new}} \leftarrow \mathrm{GainModel}\left(\boldsymbol{P}^{\mathrm{Res}};\ l_{\mathrm{window}}, N_{\mathrm{order}}\right)$ $\triangleright$ See § 4.2
16:
17:     **if** $|(\boldsymbol{G}^{\mathrm{FM}}_{\mathrm{new}} - \boldsymbol{G}^{\mathrm{FM}})/\boldsymbol{G}^{\mathrm{FM}}|_F < \varepsilon$ **then**
18:        break
19:     **else**
20:        $\boldsymbol{G}^{\mathrm{FM}} \leftarrow \boldsymbol{G}^{\mathrm{FM}}_{\mathrm{new}}$
21:     **end if**
22: **end loop**
23:
24: $\boldsymbol{T}^{\mathrm{C}} \leftarrow \mathrm{PCA}(\boldsymbol{T}^{\mathrm{Calib}} - \boldsymbol{T}^{\mathrm{Atm}} - \boldsymbol{T}^{\mathrm{Ast}};\ K_{\mathrm{max}})$ $\triangleright$ See § 4.4
25: $\boldsymbol{T}^{\mathrm{A}^*} \leftarrow \boldsymbol{T}^{\mathrm{Calib}} - \boldsymbol{T}^{\mathrm{C}}$

---

to each other, and, one of the major differences is that the EMPCA is only used for the atmospheric line estimate. Astronomical lines wider than prssure-broaden atmospheric lines are little observed actually, and other lines from astronomical sources are reproduced in both simulation (§ 5.3.4) and real observations (chapter 6). The importance of applying the EMPCA to astronomical sources will be discussed in chapter 7.

By subtracting the modeled atmospheric and astronomical lines, the algorithm estimates a timestream, $\boldsymbol{P}^{\mathrm{Res}}$, of ON-point measurement which are free from lines

Algorithm 2 AtmModel $(\boldsymbol{T}^{\mathrm{Calib}};\ K_{\max}, \theta_{\mathrm{half}}, \varepsilon)$

1: $\boldsymbol{T}^{\mathrm{Atm}} \leftarrow \boldsymbol{0}, \boldsymbol{W} \leftarrow \boldsymbol{1}$
2: **loop**
3:   $\boldsymbol{T}^{\mathrm{C}} \leftarrow \mathrm{EMPCA}(\boldsymbol{T}^{\mathrm{Calib}} - \boldsymbol{T}^{\mathrm{Atm}};\ \boldsymbol{W}, K_{\max})$ $\triangleright$ See § 4.4
4:   $\boldsymbol{T}^{\mathrm{NC}} \leftarrow \boldsymbol{T}^{\mathrm{Calib}} - \boldsymbol{T}^{\mathrm{C}}$
5:   $\tilde{\boldsymbol{T}}^{\mathrm{NC}} \leftarrow \mathcal{DM}(\boldsymbol{T}^{\mathrm{NC}})$
6:   $\tilde{s} \leftarrow \mathrm{Integration}(\tilde{\boldsymbol{T}}^{\mathrm{NC}})$ $\triangleright$ See § 2.5.2
7:   $\tilde{s}^{\mathrm{Model}} \leftarrow \mathrm{Model}(\tilde{s})$ $\triangleright$ See equation 4.23
8:   $\tilde{\boldsymbol{T}}_{\mathrm{new}}^{\mathrm{Atm}} \leftarrow \mathrm{Projection}(\tilde{s}^{\mathrm{Model}};\ \tilde{\boldsymbol{T}}^{\mathrm{NC}})$ $\triangleright$ See § 2.5.2
9:   $\boldsymbol{T}_{\mathrm{new}}^{\mathrm{Atm}} \leftarrow \mathcal{M}(\tilde{\boldsymbol{T}}^{\mathrm{Atm}})$
10:   $\boldsymbol{W} \leftarrow 2^{-|(\boldsymbol{T}_{\mathrm{new}}^{\mathrm{Atm}} - \boldsymbol{T}^{\mathrm{Atm}})/\theta_{\mathrm{half}}|}$
11:                    $\triangleright$ See equation 4.22
12:   **if** $|(\boldsymbol{T}_{\mathrm{new}}^{\mathrm{Atm}} - \boldsymbol{T}^{\mathrm{Atm}})/\boldsymbol{T}^{\mathrm{Atm}}|_F < \varepsilon$ **then**
13:    break
14:   **else**
15:    $\boldsymbol{T}^{\mathrm{Atm}} \leftarrow \boldsymbol{T}_{\mathrm{new}}^{\mathrm{Atm}}$
16:   **end if**
17: **end loop**
18:
19: **return** $\boldsymbol{T}^{\mathrm{Atm}}$

as described in (L.14). Using it we finally estimate the FM gain, $\boldsymbol{G}^{\mathrm{FM}}$, which is expected not to be affected with line emission.

With estimating FM gain of the first iteration, we then go back to the top of the outer loop, and correct for the FM gain of the ON-point timestream and repeat the same iterative processes of spectral line emission. After the outer loop is converged (normally it is conveged in the second iteration), we escape all the loops to create a final modulated timestream, $\boldsymbol{T}^{\mathrm{A}^*}$, and then make a final product of a spectrum or map.

The real-world pipeline code written in Python (Rossum, 1995) using `FMFlow` works according to the algorithm. We will show the one used for the science demonstration of Nobeyama 45 m in Appendix C.

Algorithm 3 AstModel $(\boldsymbol{T}^{\mathrm{Calib}}, \boldsymbol{T}^{\mathrm{Atm}}; K_{\max}, \theta_{\mathrm{cutoff}}, \varepsilon)$

1: $\boldsymbol{T}^{\mathrm{Ast}} \leftarrow \mathbf{0}$
2: **loop**
3: $\quad$ $\boldsymbol{T}^{\mathrm{C}} \leftarrow \mathrm{PCA}(\boldsymbol{T}^{\mathrm{Calib}} - \boldsymbol{T}^{\mathrm{Atm}} - \boldsymbol{T}^{\mathrm{Ast}}; K_{\max})$ $\qquad\qquad$ ▷ See § 4.4
4: $\quad$ $\boldsymbol{T}^{\mathrm{NC}} \leftarrow \boldsymbol{T}^{\mathrm{Calib}} - \boldsymbol{T}^{\mathrm{C}}$
5: $\quad$ $\tilde{\boldsymbol{T}}^{\mathrm{NC}} \leftarrow \mathcal{DM}(\boldsymbol{T}^{\mathrm{NC}})$
6: $\quad$ $\tilde{s} \leftarrow \mathrm{Integration}(\tilde{\boldsymbol{T}}^{\mathrm{NC}})$ $\qquad\qquad\qquad\qquad$ ▷ See § 2.5.2
7: $\quad$ $\tilde{s}^{\mathrm{Model}} \leftarrow \mathrm{Model}(\tilde{s})$ $\qquad\qquad\qquad\qquad$ ▷ See equation 4.24
8: $\quad$ $\tilde{\boldsymbol{T}}^{\mathrm{Ast}}_{\mathrm{new}} \leftarrow \mathrm{Projection}(\tilde{s}^{\mathrm{Model}}; \tilde{\boldsymbol{T}}^{\mathrm{NC}})$ $\qquad\qquad$ ▷ See § 2.5.2
9: $\quad$ $\boldsymbol{T}^{\mathrm{Ast}}_{\mathrm{new}} \leftarrow \mathcal{M}(\tilde{\boldsymbol{T}}^{\mathrm{Ast}}_{\mathrm{new}})$ $\qquad\qquad$ ▷ use this if spectral line observation
10: $\quad$ $\boldsymbol{T}^{\mathrm{Ast}}_{\mathrm{new}} \leftarrow \boldsymbol{T}^{\mathrm{Ast}} + 0.5 \times \mathcal{M}(\tilde{\boldsymbol{T}}^{\mathrm{Ast}}_{\mathrm{new}})$ $\qquad$ ▷ use this if mapping observation
11: $\quad$ **if** $|(\boldsymbol{T}^{\mathrm{Ast}}_{\mathrm{new}} - \boldsymbol{T}^{\mathrm{Ast}})/\boldsymbol{T}^{\mathrm{Ast}}|_F < \varepsilon$ **then**
12: $\qquad$ break
13: $\quad$ **else**
14: $\qquad$ $\boldsymbol{T}^{\mathrm{Ast}} \leftarrow \boldsymbol{T}^{\mathrm{Ast}}_{\mathrm{new}}$
15: $\quad$ **end if**
16: **end loop**
17:
18: **return** $\boldsymbol{T}^{\mathrm{Ast}}$

Pressure (hPa)	Temperature (K)	Ozone column density (cm^{-2})
0.1	221.1	1.74×10^{-6}
0.3	243.3	1.64×10^{-6}
0.4	249.4	1.62×10^{-6}
0.5	254.9	1.81×10^{-6}
0.7	262.8	2.12×10^{-6}
1	265.8	2.66×10^{-6}
2	256.4	3.99×10^{-6}
3	248.9	5.83×10^{-6}
4	244.3	7.19×10^{-6}
5	240.5	8.00×10^{-6}
7	234.8	8.51×10^{-6}
10	230.0	8.71×10^{-6}
20	221.7	7.69×10^{-6}
30	216.5	5.52×10^{-6}
40	212.4	3.53×10^{-6}
50	208.9	2.20×10^{-6}
70	200.4	1.16×10^{-6}
100	197.8	3.92×10^{-7}
150	207.4	1.14×10^{-7}
200	219.4	6.18×10^{-8}
250	230.4	5.02×10^{-8}
300	239.9	4.70×10^{-8}
350	247.9	4.58×10^{-8}
400	254.9	4.52×10^{-8}
450	261.2	4.47×10^{-8}
500	266.8	4.39×10^{-8}
550	271.8	4.30×10^{-8}
554	272.2	4.24×10^{-8}

Table 4.1: Parameters used for creating atmospheric ozone spectra by am. Each column shows the pressure, temperatures at the bottom of each layer, and column densities of ozone of each layer. These values are taken from an am configuration file of ALMA_annual_50.amc available at https://www.cfa.harvard.edu/~spaine/am/cookbook/unix/sites/ALMA/.

Errors should never pass silently. Unless explicitly silenced. In the face of ambiguity, refuse the temptation to guess.

From the Zen of Python, by Tim Peters

5

On-site Verification

This chapter describes scientific verification of the FMLO method by on-site commissioning of the FMLO systems implemented on the Nobeyama 45 m and the ASTE 10 m telescopes (see Chapter 3).

We present the summaries of the FMLO test observations of these telescopes (§ 5.1) which are used for several verification items. We also introduce the concept of frequency modulation patterns (FMPs), which control the total frequency modulation width and each frequency modulation step of LO frequency during an observation. We then present the result of system-level verification items of the FMLO method (§ 5.2), which must be verified before the FMLO observations. In the final section (§ 5.3), we present end-to-end data reduction with the signal processing of the FMLO method. We embed some artificial signal (spectrum) to the sky (i.e., off-point) observations of the FMLO method with several FMPs as simulations and demonstrate that the signal processing of the FMLO method (see Chapter 4) works well and the final spectrum is consistent with those of the conventional position switching method. We also define here the optimal FMP to be used for an FMLO observation. Finally, we derive the observation efficiency of the FMLO method and demonstrate how it is improved compared with that of the conventional position switching method quantitatively.
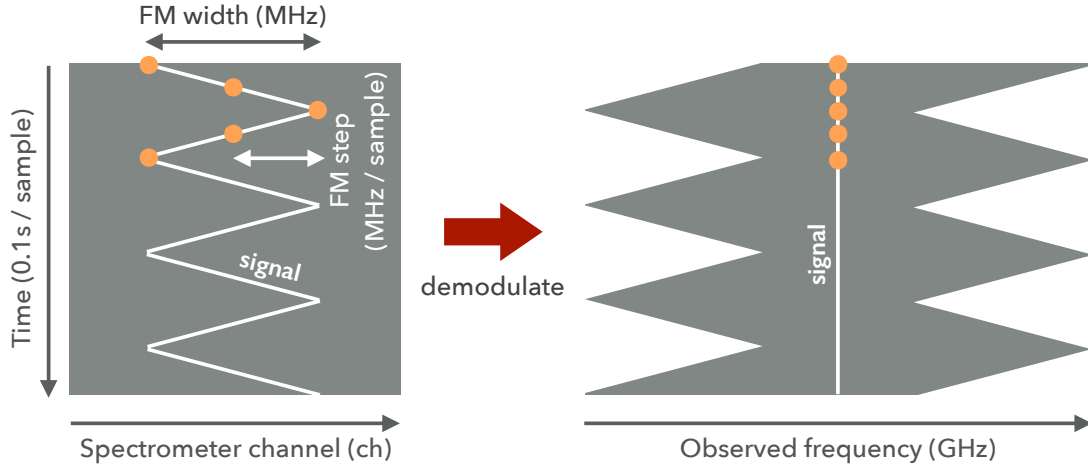
Figure 5.1: Schematic diagram of a zig-zag frequency modulation pattern. (left) modulated timestream, where orange dots repredent modulated signals. The FM width (dark arrow) is a total modulation width over a timestream, and FM step (white arrow) is an interval between successive time samples. (right) demodulated timestream, where signals are aligned to an observed frequency.

5.1 OBSERVATIONS

5.1.1 FREQUENCY MODULATION PATTERNS

As described in § 3.2, we use a signal generator which can modulate a LO frequency according to a frequency modulation pattern file. It is therefore necessary to define how LO frequency modulates during an FMLO observation. It is referred to as a frequency modulation pattern (FMP). During the verification and science demonstration of both Nobeyama 45 m and ASTE 10 m, we used zig-zag FMPs as illustrated in figure 5.1. The zig-zag FMP has two free paramters:

FM width the total LO frequency modulation width during an FMLO observation in units of MHz.

FM step the LO frequency modulation step between adjacent spectrometer samples in units of MHz/sample.

In the actual FMP files, we slightly change LO frequency at the foldings of

66

zig-zag patterns so that LO frequencies do not completely overlap each other.

By definition, the total observed band width is the sum of the total band width of spectrometer and the FM width. As illustrated in figure 5.1, wider FM width results in wider total observed band width but less number of samples at the edge of demodulated timestreams, which causes sensitivity loss compared to the center of the observed band. On the other hand, narrower FM width or shorter FM step are possible to fail to estimate correlated and non-correlated components by PCA when the frequency width of a target spectral line is wider than them, which makes incorrect estimates of spectral line or mapping even signal processing works correctly (i.e., the number of principal components is properly optimized). It is therefore necessary to search which parameters should be used in an FMLO observation by simulations of observations of artificial spectral line with FMPs of different FM widths and FM steps. This will be further discussed in § 5.3.4.

5.1.2 Observations of Nobeyama 45 m

We carried out test observations of the FMLO method in 2014, 2016, and 2017 (PI: Yoichi Tamura, ID: i2514yt). As described in chapter 3, we obtained timestreams with the TZ front-end receiver and the SAM45 backend spectrometer with the FMLO system implemented. We summarize verification items and their observation parameters in Table 5.1.

Unless otherwise spacified, we allocated A7 array of SAM45 with LSB (98 GHz) and A5 array with USB (110 GHz), and used output timestream data for the following analyses. We configured the spectral resolution of SAM45 as 0.48828 MHz and the total bandwidth as 2000 MHz (4096 channels in total), which correspond 1.33 km/s and 5451 km/s in velocity representation at the observed frequency of 110 GHz. The output timestream data were recorded at a rate of 10 Hz by the OTF mode of the Nobeyama 45 m. The obtained output timestream data, frequency modulation log files, and antenna log files were offline-merged into FITS files by the `FMFlow`, the data analysis package for the FMLO method (see appendix C). In the following data analyses, we conducted 2-channel binning to the timestream data to half the total number of channels as 2048 for reducing computation time

of each analysis. For the comparison of the spectral line or mapping of the FMLO method with that of the conventional PSW method, we simultaneously observed and obtained PSW data for science demonstration (see chapter 6).

5.1.3 Observations of ASTE 10 m

We carried out test observation of the FMLO method in 2016 (PI: Yoichi Tamura, ID: fmlo16). As described in chapter 3, we obtained timestreams with the DASH345 front-end receiver for 345 GHz (Band 7) band and Band 8 QM receiver for 490 GHz (Band 8) band, and the MAC backend spectrometer with the FMLO system implemented. We summarize verification items and their observation parameters in Table 5.2.

Unless otherwise spacified, we allocated A1 array of MAC with LSB and used output timestream data for the following analyses. We configured the spectral resolution of MAC as 0.5 MHz and the total bandwidth as 512 MHz (1024 channels in total), which correspond 0.43 km/s and 445 km/s in velocity representation at the observed frequency of 345 GHz. The output timestream data were recorded at a rate of 10 Hz by the OTF mode of the ASTE. The obtained output timestream data, frequency modulation log files, and antenna log files were offline-merged into FITS files by the `FMFlow`, the data analysis package for the FMLO method (see appendix C). For the comparison of the spectral line or mapping of the FMLO method with that of the conventional PSW method, we simultaneously observed and obtained PSW data for science demonstration (see chapter 6).

Item	Section	Observation period	ν_{obs} (GHz)	FM width (MHz)	FM step (MHz/sample)
Continuous wave	§ 5.2.1	Early June 2014	98	60.96	0.03–0.5[†]
R-Leo SiO maser	§ 5.2.2	Early June 2017	86	125	10
Blank sky	§ 5.3	Early June 2017	98/110	31–2000[*]	3–80[⋆]
IRC+10216	§ 6.1	Early June 2016	98/110	250	80
Orion KL region	§ 6.2	Early June 2016	98/110	120	40

Table 5.1: Summary of the FMLO observations at Nobeyama 45 m telescope for various commisioning items.
[†]: see table 5.3, [*]: see table 5.4, [⋆]: see table 5.5

Item	Section	Observation period	ν_{obs} (GHz)	FM width (MHz)	FM step (MHz/sample)
Blank Sky	§ 5.2.2	Late August 2016	346	128	32
Orion donut	§ 6.1	Late August 2016	346	256	64
IRAS 16293−2422	§ 6.1	Late August 2016	346	256	64

Table 5.2: Summary of the FMLO observations at ASTE 10 m telescope for various commisioning items.
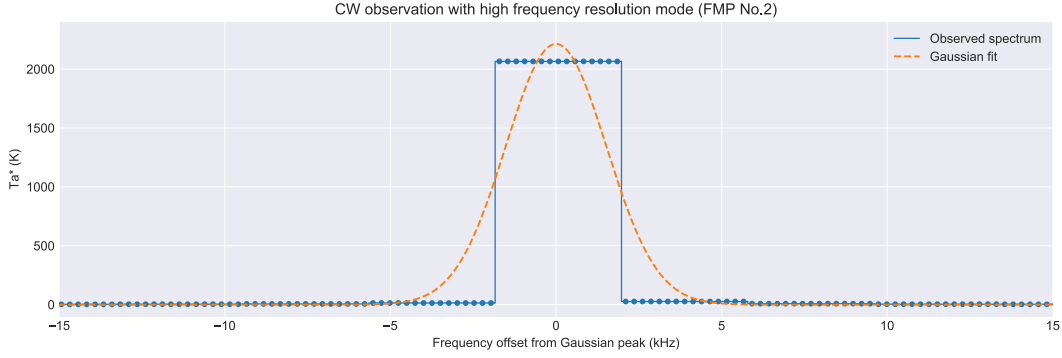
Figure 5.2: The final spectrum of continuous wave at 98.0 GHz measured at Nobeyama 45 m. We plot it as blue line, while blue dots are over-sampled data points used to a Gaussian fit. The fitted Gaussian is shown as dashed orange line, whose center frquency is 98.000002379 GHz and FWHM is 2.864 kHz ($<$ 3.81 kHz).

5.2 System verification

5.2.1 Frequency purity

First of all, we must confirm whether no frequency perturbation occurs or not with frequency modulation during an observation and demodulation process: if such perturbation could really happen, a spectral line in a final spectrum would have incorrect line width (wrongly broad) and/or intensity. This frequency "purity" must be guaranteed before all FMLO observations. We thus carried out FMLO observations of an artificial continuous wave (CW) at 98.0 GHz with five FMPs (see table 5.3) and the highest resolution mode of the spectrometer SAM45 (a total band width of 15.625 MHz, a channel width of 3.81 kHz). The telescope antenna is fixed at an elevation of 70 deg during an observation. After obtaining cleaned timestreams using the signal processing, we create the final spectrum of CW like figure 5.2 and then conduct a Gaussian fit to it for deriving line width and center frequency of a CW spectrum.

The results of Gaussian fittings derived from all FMLO measurements of five FMPs are listed in table 5.3, which indicates that the FWHMs of Gaussian are narrower than that of channel width (3.81 kHz). This guarantees that the frequency purity meets the specification even with the high frequency resolution mode of

70

No.	FM width (MHz)	FM step (kHz/sample)	Gaussian FWHM (kHz)
1	60.96	499.49	2.900
2	60.96	249.94	2.864
3	60.96	124.59	2.980
4	60.96	62.865	2.863
5	60.96	31.623	2.850

Table 5.3: The parameters of frequency modulation patterns used for continuous wave measurements and the FWHMs of Gaussian derived from Gaussian fitting to the final spectrum of each measurement. The FM width used are much wider than the total band width (15.625 MHz) because we aim to testify the frequency purity under a such extreme condition.

SAM45.

5.2.2 Time synchronization

As described in § 3.2, the synchronization between the frequency modulation and the data acquisition of the spectrometer must be adjusted before observation in order to avoid spectrum leaking in timestreams. We adjusted this synchronization by observing bright spectral lines with changing the trigger delay parameter which defers a start time of a waveform generator's output (rectangular wave) after triggered by the 1pps signal of the system clock.

In the case of Nobeyama 45 m, we observed bright the SiO J=2–1, v=1 maser line at $\nu_{\rm rest}$ = 86.24337 GHz with varying the trigger delay parameter's value from -70 ms to + 20 ms in mid May and early July of 2017. Figure 5.3 shows the result of these observarions. The right side of the figure shows the leaking spectra exist next to those of the main at the proper frequency. Leaking spectra are diminishing as trigger delay parameter's value increases, which suggests the exact time synchronization requires a trigger delay parameter's value as $\sim$ 20 ms. We quantitatively derive the exact value by calculating the leaking rate of each trigger delay paramter and interpolation of data points. The left side of the figure is the relation between trigger delay parameters and leakage rates, $f_{\rm leak}$. The leakage rate is the fraction of integrated intensity of leaking spectrum over that of
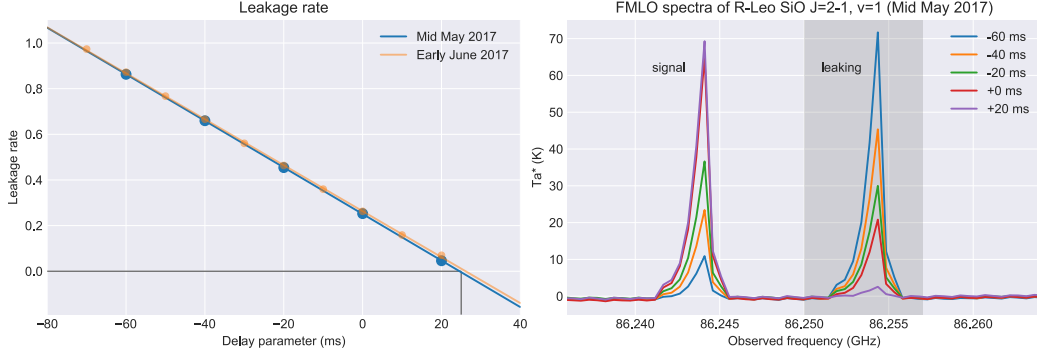
71

Figure 5.3: The result of time synchronization between the frequency modulation and the data acquisition of the spectrometer SAM45 in Nobeyama 45 m. (left) spectrum leakage rate, f_{leak}, as a function of the trigger delay parameter in units of millisecond. The five points are obtained by integrated intensity ratio $I_{\mathrm{leak}}/(I_{\mathrm{main}} + I_{\mathrm{leak}}) \equiv f_{\mathrm{leak}}$ from the spectra in Mid May 2017 shown in the right panel. The linear fit to the points yields the optimal trigger delay parameter's value as +24.59 ms (Mid May 2017) and +26.13 ms (Early June 2017). (right) The spectra of SiO maser lines of R-Leo observed with various trigger delay parameters. The spectra are created by the cleaned timestream using only the samples whose FM channels, $\xi(n)$, fulfill $\xi(n) - \xi(n-1) > 0$. The lines within a shading are the leaking spectra from adjacent time samples.

total (main and leaking) spectra:

$$f_{\mathrm{leak}} = \frac{I_{\mathrm{leak}}}{I_{\mathrm{main}} + I_{\mathrm{leak}}} \tag{5.1}$$

where I denotes integrated intensity of spectrum, $I = \int T_{\mathrm{A}}^{*} \mathrm{d}\nu$. As results of interpolation of data points of two observation seasons, we derive the optimal trigger delay parameter's value as +24.59 ms (mid May 2017) and +26.13 ms (early June 2017), respectively. The difference of values between two observation seasons is ~1.5 ms, which is small enough compared to the settling time ($\lesssim 8$ ms) of the signal generator. This means that the spectrum leaking is expected not to occur if we set the trigger delay parameter's value so that the data aquisition starts during the settling time. In the following FMLO observations, we set the optimal trigger delay parameter's value as +25 ms and confirm that spectrum leaking did not occur at each signal processing of timestream.

In the case of ASTE 10 m, we observed atmospheric CO(3–2), v=0 rotational line at $\nu_{\mathrm{rest}} = 345.79599$ GHz in mid August 2016 because no bright astronomical
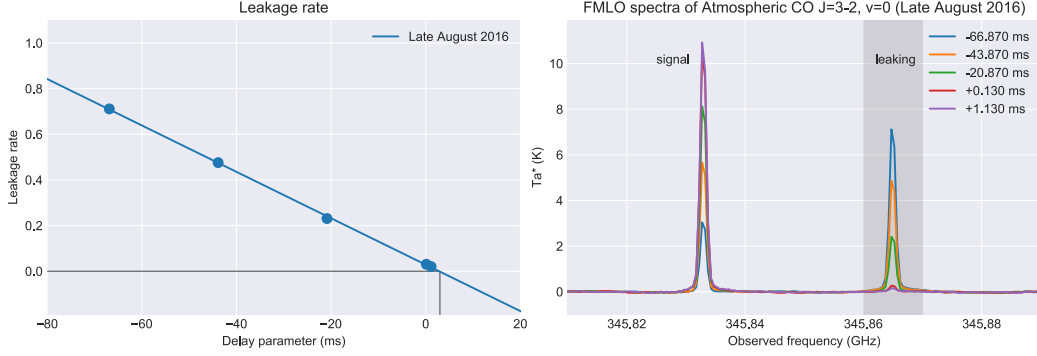
Figure 5.4: The result of time synchronization between the frequency modulation and the data acquisition of the spectrometer MAC in ASTE 10 m. (left) spectrum leakage rate, f_{leak}, as a function of the trigger delay parameter in units of millisecond. The five points are obtained by integrated intensity ratio $I_{\text{leak}}/(I_{\text{main}} + I_{\text{leak}}) \equiv f_{\text{leak}}$ from the spectra shown in the right panel. The linear fit to the points yields the optimal trigger delay parameter's value as $+2.83$ ms. (right) The spectra of atmospheric CO (3–2) lines observed with various trigger delay parameters. The spectra are created by the cleaned timestream using only the samples whose FM channels, $\xi(n)$, fulfill $\xi(n) - \xi(n-1) > 0$. The lines within a shading are the leaking spectra from adjacent time samples.

lines were available during the commissioning. We varied the trigger delay parameter from -67 ms to + 1 ms. Figure 5.4 shows the result of these observarions in the same manner as Nobeyama 45 m. As a result of interpolation of data points, we derive the optimal trigger delay parameter's value as $+2.83$ ms. In the following FMLO observations, we set the optimal trigger delay parameter's value as $+3$ ms and confirm that spectrum leaking did not occur at each signal processing of timestream.

5.3 End-to-end data reduction

In this section, we present data reduction of the FMLO observations at Nobeyama 45 m according to the signal processing described in chapter 4. We observed the blank sky (i.e., OFF-point) with the FMLO method, where no astronomical spectral lines are expected to exist. Such observations can minimize the effect of astronomical signal and thus suitable for demonstration of, in particular, gain correction, estimating correlated noises, and measuring noise levels. In the following
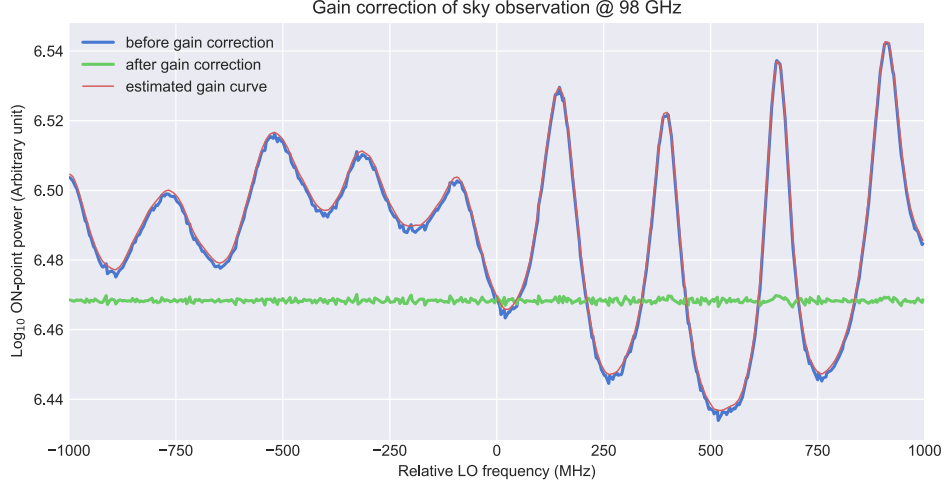
Figure 5.5: The demonstration of gain correction in a timestream data of LSB, $\boldsymbol{P}^{\mathrm{ON}}$, after subtracting atmospheric and astronomical signals. We plot $\boldsymbol{P}^{\mathrm{ON,sorted}}$ at the center channels of the spectrometer SAM45 as a function of relative LO frequency (i.e., $\xi(n)$; blue line) and the result gain curve fitted by a Savitzky-Golay filter ($l_{\mathrm{window}} = 51$, $N_{\mathrm{order}} = 3$; red line). The unit of vertical axis is artibrary unit but proportional to power. We can see characteristic periodic patterns in the gain curve. We also plot the FM gain corrected $\boldsymbol{P}^{\mathrm{ON,sorted}}$ as green line.

subsections, we demonstrate each signal processing works well step by step, and verify that the achieved noise level of the FMLO observations improve compared to that of conventional PSW method. We then conduct simulations of embedding artificial spectral line to timestreams of observations with different frequency modulation patterns (FMPs).

5.3.1 GAIN CORRECTION

From the beginning of signal processing, we estimate frequency modulation gain, $\boldsymbol{G}^{\mathrm{FM}}$. Since we didn't obtain frequency modulation load measurements, we estimate $\boldsymbol{G}^{\mathrm{FM}}$ from ON-point timestream itself, $\boldsymbol{P}^{\mathrm{ON}}$, as the first choice described in § 4.2. Note that this means that we antecedently model and subtract atmospheric lines to make $\boldsymbol{P}^{\mathrm{ON}}$ without containing any spectral line signals. Once we obtain $\boldsymbol{P}^{\mathrm{ON}}$, we sort it according to FM channel, $\xi(n)$, and then interpolate $\boldsymbol{P}^{\mathrm{ON}}$ along FM channel to make a sorted and resampled ON-point timestream, $\boldsymbol{P}^{\mathrm{ON,sorted}}$ as
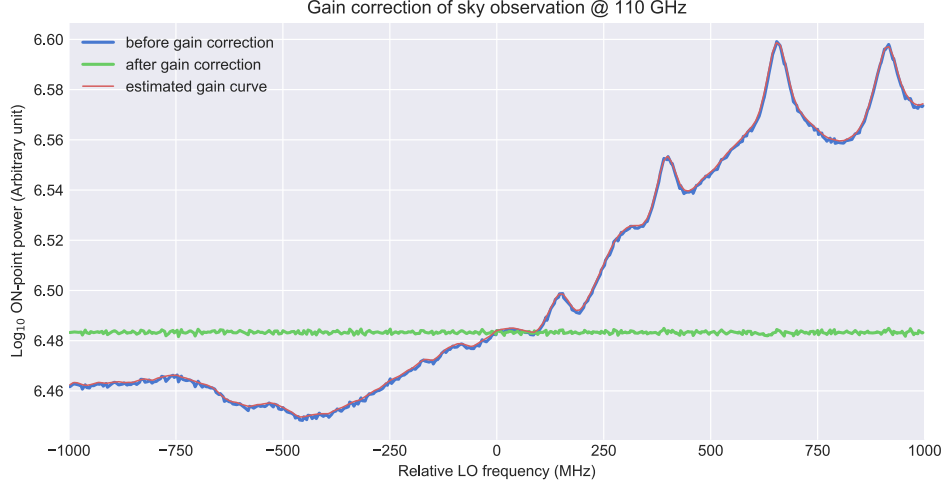
Figure 5.6: The demonstration of gain correction in a timestream data of USB, $\boldsymbol{P}^{\mathrm{ON}}$, after subtracting atmospheric and astronomical signals. We plot $\boldsymbol{P}^{\mathrm{ON,sorted}}$ at the center channels of the spectrometer SAM45 as a function of relative LO frequency (i.e., $\xi(n)$; blue line) and the result gain curve fitted by a Savitzky-Golay filter ($l_{\mathrm{window}} = 51$, $N_{\mathrm{order}} = 3$; red line). The unit of vertical axis is artibrary unit but proportional to power. Although the shape of gain curve is different from that of LSB, some periodic patterns can be seen at the same LO frequencies of LSB. We also plot the FM gain corrected $\boldsymbol{P}^{\mathrm{ON,sorted}}$ as green line.

described in § 4.2.

Figure 5.5 and 5.6 show logarithmic $\boldsymbol{P}^{\mathrm{ON,sorted}}$ of an FMLO observation whose FM width is 2000 MHz and FM step is 10 MHz/sample, at spectrometer channels which see 98 GHz and 110 GHz at $\xi(n) = 0$, respectively. As results of plotting, they clearly show strong and periodic dependences on LO frequency in both LSB and USB, so we hereafter call it gain curve. Note that another spectrometer channels also show such dependencies. We then apply Savitzky-Golay filter to model the gain curves and subtract the models from them in logarithmic space (corresponding division in linear space). We use window length of the filter as $l_{\mathrm{window}} = 51$ and order of the polynomial as $N_{\mathrm{order}} = 3$. These parameters are determined from the gain curves themselves, which are smooth enough to fit overall features of the gain curve but not to fit noisy features (i.e., overfitting). The model subtracted $\boldsymbol{P}^{\mathrm{ON,sorted}}$ are plotted as grean lines in figure 5.5 and 5.6,

Figure 5.7: The time-series plots of a spectrometer's channel of modulated timestreams before and after gain correction with a blank sky observation at LSB around 98 GHz. (top) the time-series plots at the center channels of the spectrometer SAM45. (bottom) the corresponding FM channels, $\xi(n)$, used for an FMLO observation. We can clearly see that most of fluctuation are attributed to the FM gain variation as a function of $\xi(n)$. We note that the periodic features in the blue line at time frequency of ~ 2 Hz is independent on the frequecy modulation pattern.

respectively, which show the gain curves are now flat. Note that ON-point power at $\xi(n) = 0$ does not change before and after the model subtraction.

After correcting FM gain of both LSB and USB, we conduct intensity calibration according to the equation 4.8 to make $\boldsymbol{T}^{\mathrm{Calib}}$. Figure 5.7 and 5.8 show $\boldsymbol{T}^{\mathrm{Calib}}$ at spectrometer channels which see 98 GHz and 110 GHz at $\xi(n) = 0$, respectively before and after FM gain correction. Before FM gain correction, they clearly show strong and periodic dependenies on FMP due to the effect of gain changes, while after FM gain correction, they are flat timestreams. Note that although they seem to be flat enough in both figures, correlated components are still remaining in $\boldsymbol{T}^{\mathrm{Calib}}$, which should be modeled and subtracted by correlated component removal. How FM gain correction decreases the correlation over channels will be discussed in the following section of correlated component removal.
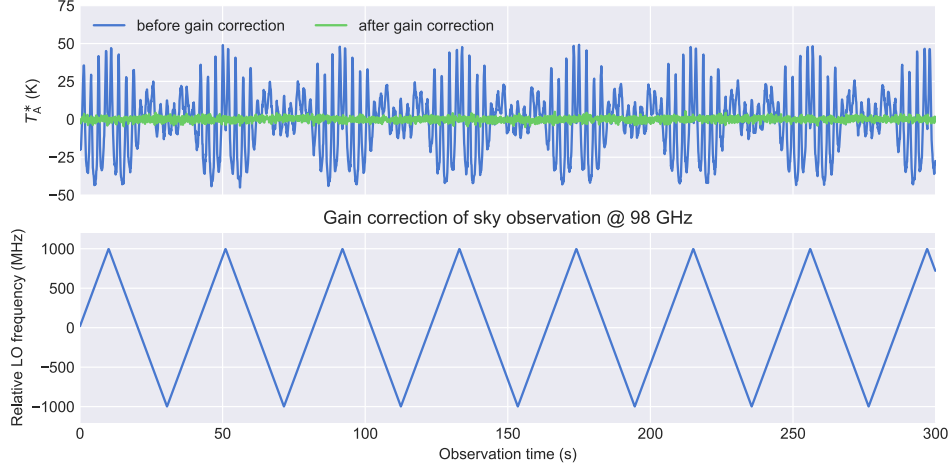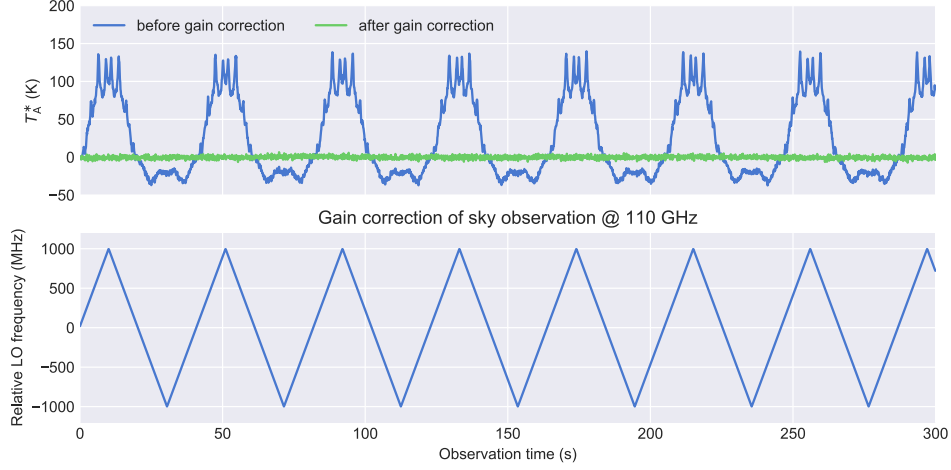
Figure 5.8: The time-series plots of a spectrometer's channel of modulated timestreams before and after gain correction with a blank sky observation at USB around 110 GHz. (top) the time-series plots at the center channels of the spectrometer SAM45. (bottom) the corresponding FM channels, $\xi(n)$, used for an FMLO observation. We can clearly see that most of fluctuation are attributed to the FM gain variation as a function of $\xi(n)$.

5.3.2 Correlated component removal

Using FM gain corrected and intensity calibrated timestream, $\boldsymbol{T}^{\mathrm{Calib}}$, we then conduct model and remove correlated components by the EMPCA as described in § 4.4. Since there are no astronomical signals in, $\boldsymbol{T}^{\mathrm{Calib}}$, we then model only atmospheric line emission, $T^{\mathrm{Atm}}(\boldsymbol{1} - \boldsymbol{e}^{-\boldsymbol{\tau}^{\mathrm{NC}}})$, as described in § 4.5.1, and then subtract it from $\boldsymbol{T}^{\mathrm{Calib}}$ and remodel correlated components in an iteration loop. After model estimates are converged, we make a final spectrum from correlated components subtracted timestream, $\boldsymbol{T}^{\mathrm{Clean}}$, according to §2.5.

Figure 5.9 and 5.10 show the final spectra of LSB (around 98 GHz) and USB (around 110 GHz) with correlated components subtracted. The total observed bands of both spectra contain bright ozone spectral lines. In the case of LSB, the ozone line ($\nu_{\mathrm{rest}} = 96.2$ GHz) is located near the left edge of the observed band, which means that the number of samples that observed the ozone line is much smaller than the total number of samples ($N = 3000$). This increases the total

77

Figure 5.9: The spectra of blank sky around 98 GHz (LSB) at the first and last (34-th) iteration. The fitst one (blue line) shows atmosphric ozone line emission, but there exist negative sidelobe-like features around peaks. The last one (green line) shows that such features are dinimished. We also plot the model spectrum at the last iteration (red line). Because the line emission is located at the edge of the observed band, it takes more iteration to reproduce it compared to USB spectrum.

number of iterations of modeling atmospheric lines until it is converged compared to that of USB. In the case of USB, two ozones lines ($\nu_{\text{rest}} = 109.6, 110.8$ GHz) are located at the middle of the observed band and the number of iterations of modeling atmospheric lines is much smaller than that of LSB.

Both spectra show that the iterative modeling of correlated components and atmospheric lines by the EMPCA successfully removes spectral baseline wiggles and reconstructs the atmospheric lines. We further verify it by plotting how the effect of atmospheric lines is minimized in correlated components. Figure 5.11 and 5.12 show variance of coeffeicients of principal components, $\boldsymbol{C}$, of LSB and USB at each iteration, respectively. By the definition of PCA, these quantities are equal to eigen values of corresponding eigenvectors, $\boldsymbol{P}$, which represents contribution of each eigen vector used to be reconstruct correlated components. As a result of LSB, correlated components estimated in the first iteration contain ozone signal and the optimal number of principal components is estimated to be 6 according to the choosing strategy described in § 4.4.4. After seveal iterations, most of ozone
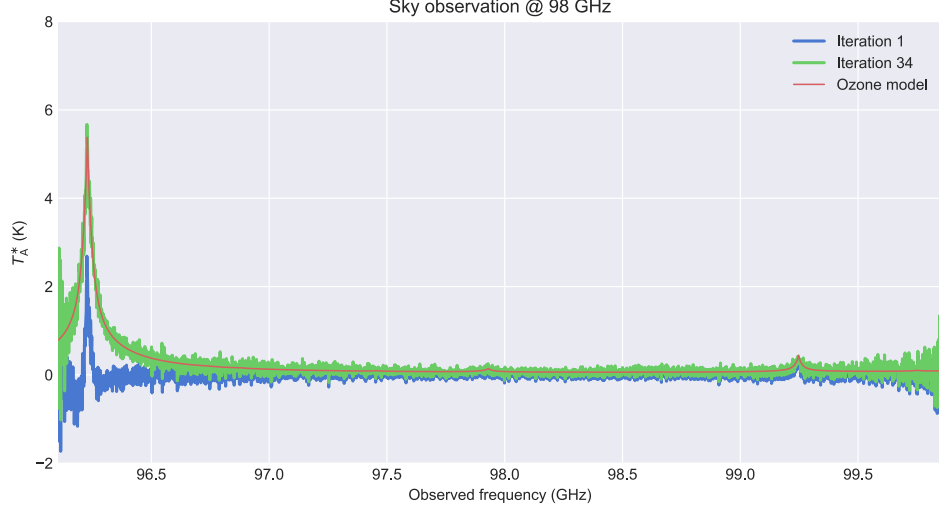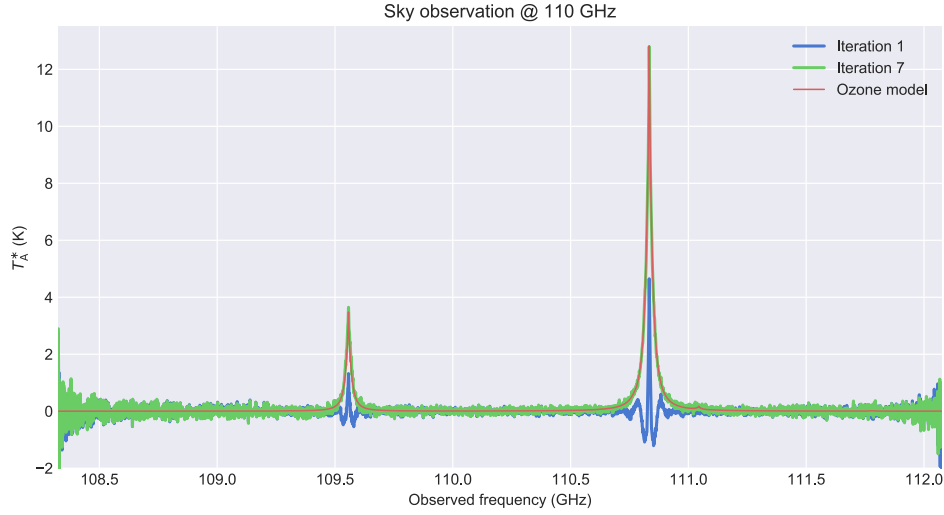
Figure 5.10: The spectra of blank sky around 110 GHz (USB) at the first and last (7-th) iteration. The fitst one (blue line) shows atmosphric ozone line emission, but there exist negative sidelobe-like features around peaks. The last one (green line) shows that such features are dinimished. We also plot the model spectrum at the last iteration (red line).

signal is estimated and isolated by modeling of atmospheric lines before estimating correlated components, which minimizes the contribution of ozone signal into the correlated components and thus the optimal number of principal components decreases to 5 in the final (34th) iteraion. As a result of USB, we can see this isolation more drastically: The optimal number of principal components decreases from 50 to 5 during 7 iterations.

We also verify how correlated component removal reduces low frequency noises ($\lesssim 10$ Hz) in a cleaned timestream, $\boldsymbol{T}^{\mathrm{Clean}}$, by plotting power spectral densities (PSDs) and covariance matrice of timetream before and after correlated component removal. Figure 5.13, 5.14, 5.15, and 5.16 show the results of both LSB and USB. They represent that almost all low frequency noises are attributed to gain changes due to frequency modulation, and PSDs are flat after gain correction. But as is seen in the covariance matrices, correlated components are still remaining in the calibrated timestreams, $\boldsymbol{T}^{\mathrm{Calib}}$. After correlated component removal, low frequency noises less than 0.1 Hz decrease by 0.5 dex, which are dominant correlated

Figure 5.11: The demonstration of how eigen values changes in iterative processes of the EMPCA and modeling atmospheric line emission in the data of blank sky at LSB (around 98 GHz). The lines indicate the value of eigen values (equivalent to variance of data points along the axis of eigenvector) as a function of N-th largest principal component. The circle markers are estimated optimal number of principal components, K_{opt}, as results of exponential curve fit described in § 4.4.4. The estimated $\boldsymbol{P}$ and $\boldsymbol{C}$ are converged after 34 iterations, and the final $K_{\mathrm{opt}} = 5$ is same as that of USB.

components. Covariance matrices after correlated component removal also shows that there are almost no correlated components remaining compared to diagonal (auto correlation) values.

5.3.3   ACHIEVED OBSERVATION EFFICIENCY

After subtracting atmospheric lines, we derive a residual timestream which is expected to contain only non-correlated noises, $\boldsymbol{E}^{\mathrm{NC}}$. With this timestream, we evaluate the noise level of the final spectrum and verify that the achieved noise level of the FMLO method actually improves compared to that of PSW method.

We denote the 1σ noise level (sensitivity) of each spectrometer channel of a final spectrum as ΔT. In the conventional PSW method, it is represented as root sum of the noises from ON- and OFF-point:

$$\Delta T^2 = \Delta T_{\mathrm{ON}}^2 + \Delta T_{\mathrm{OFF}}^2 \tag{5.2}$$
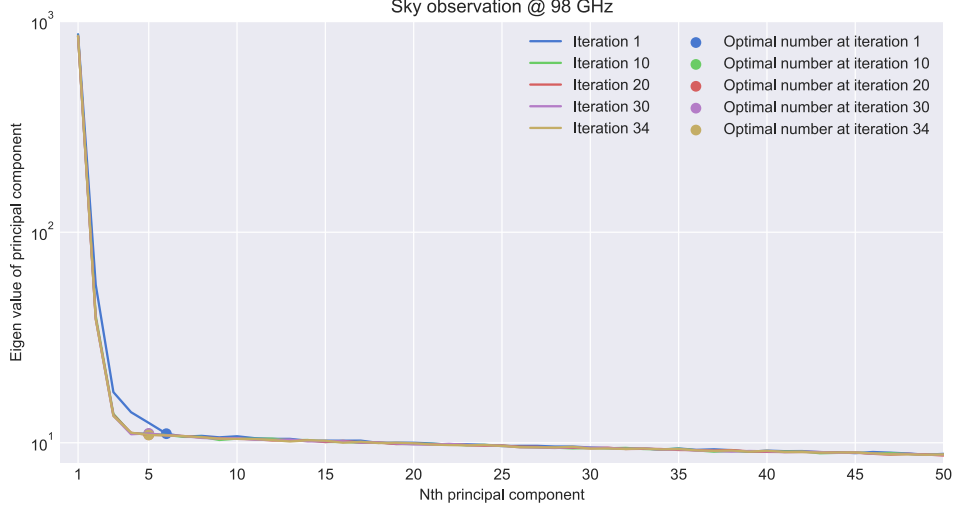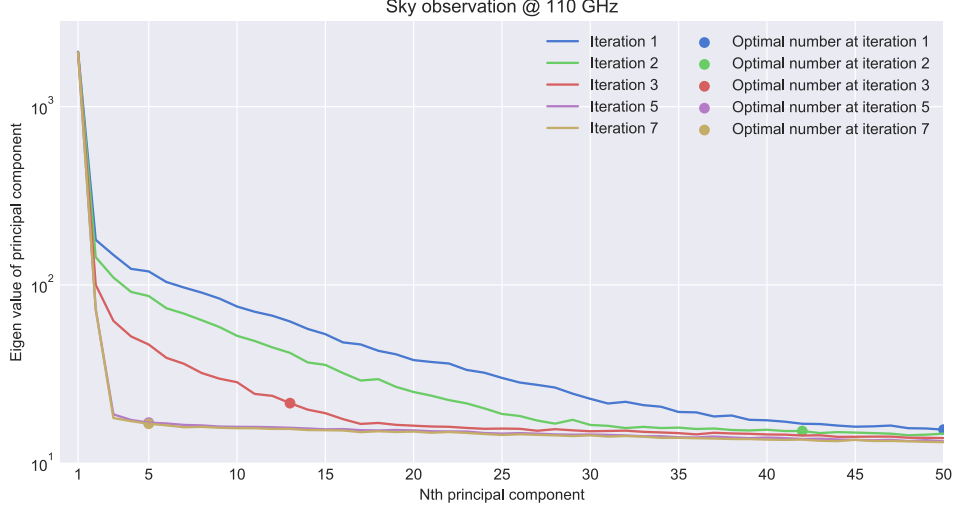
Figure 5.12: The demonstration of how eigen values changes in iterative processes of the EMPCA and modeling atmospheric line emission in the data of blank sky at USB (around 110 GHz). The lines indicate the value of eigen values (equivalent to variance of data points along the axis of eigenvector) as a function of N-th largest principal component. The circle markers are estimated optimal number of principal components, K_{opt}, as results of exponential curve fit described in § 4.4.4. The estimated $\boldsymbol{P}$ and $\boldsymbol{C}$ are converged after 7 iterations, and the final $K_{\mathrm{opt}} = 5$ is same as that of LSB.

Since the ON- and OFF-source integration times are equal in general, we can write ΔT as the following equation:

$$\Delta T_{\mathrm{PSW}} = \frac{\sqrt{2}\, T_{\mathrm{sys}}}{\sqrt{\Delta \nu \, t_{\mathrm{ON}}}} \tag{5.3}$$

where T_{sys} is system noise temperature of a telecope at observed frequency, $\Delta \nu$ is channel width of a spectrometer, and t_{ON} is an ON-source integration time to be used to make a spectrum. In the proposed FMLO method, we don't observe OFF-point but model it by the correlated component removal, which is expected to be less noises from the model to be added to ON-point timestream. Since ΔT of the FMLO method is also proportional to $T_{\mathrm{sys}}/\sqrt{\Delta \nu \, t_{\mathrm{ON}}}$, we can write it as the following equation:

$$\Delta T_{\mathrm{FMLO}} = \frac{\alpha \, T_{\mathrm{sys}}}{\sqrt{\Delta \nu \, t_{\mathrm{ON}}}} \tag{5.4}$$

Figure 5.13: The power spectrum densities (PSDs) created by various timestreams of blank sky around 98 GHz (LSB) using the Welch method: (a) the one created by T^{calib} before gain correction (i.e., the first outer loop of the pipeline algorithm; blue line), (b) the one created by T^{calib} after gain correction (the second outer loop; green line), and (c) the one created by T^{a^*} (red line). We note that periodic power fluctuations are observed at time frequency of ~ 2 Hz, which is independent on the frequency modulation pattern used for an FMLO observation.

where α is a factor of noise contribution from correlated component removal and expected to be less than $\sqrt{2}$. If comparing both noise level of PSW and FMLO method with the same ON-source integration time, the FMLO method is expected to improve the sensitivity $\sqrt{2}/\alpha$ times better than that of PSW method. If comparing both noise level of PSW and FMLO method with the same *total observation time*, which is more practical comparison when we suppose an observation, the FMLO method is expected to improve much more sensitivity because observing efficiency is much higher than that of PSW method. We hereafter define the observation efficiency, η_{obs}, as a fraction of ON-source time over a total observation time:

$$\eta_{\mathrm{obs}} = t_{\mathrm{ON}}/t_{\mathrm{Total}} \tag{5.5}$$

In the ideal cases where the overhead time such as telescope slue time between ON- and OFF-point is negligible, the observation efficiency of the PSW method is $\eta_{\mathrm{obs,PSW}} \simeq 0.5$ because the ON- and OFF-source integration times are equal,
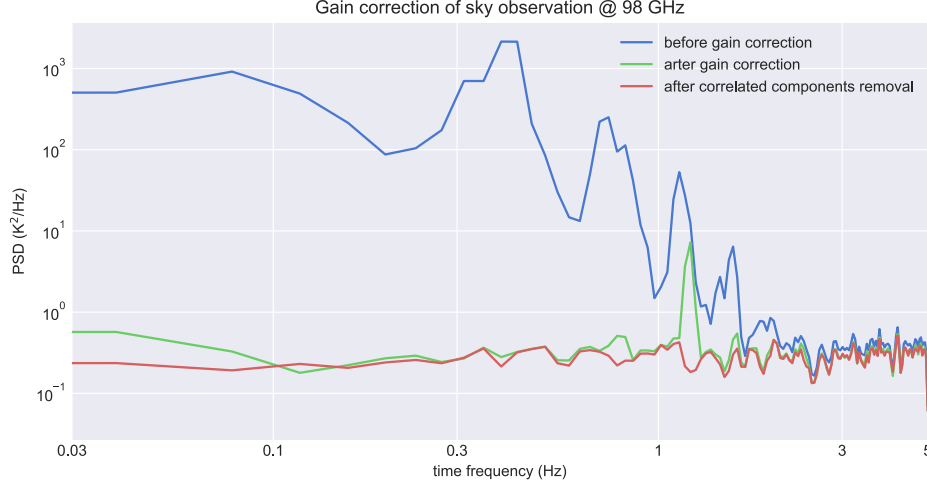
82
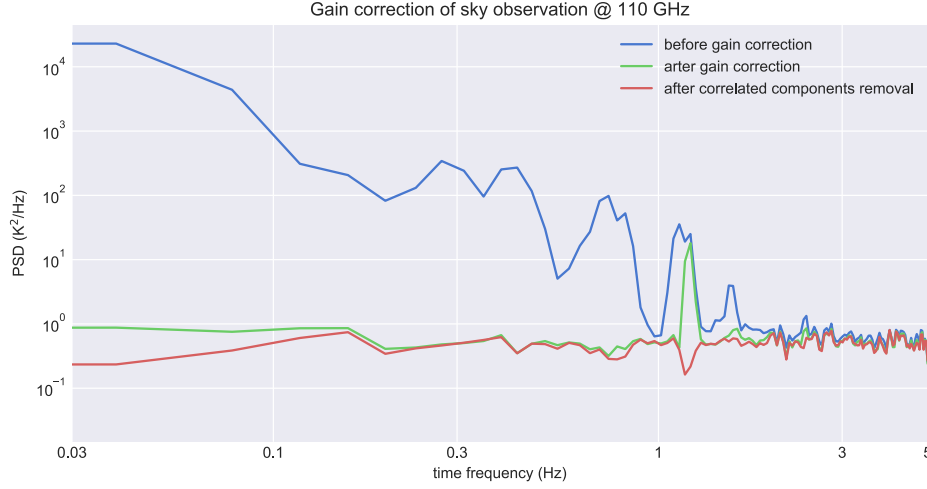
Figure 5.14: The power spectrum densities (PSDs) created by various timestreams of blank sky around 110 GHz (USB) using the Welch method: (a) the one created by T^{calib} before gain correction (i.e., the first outer loop of the pipeline algorithm; blue line), (b) the one created by T^{calib} after gain correction (the second outer loop; green line), and (c) the one created by T^{a^*} (red line). We note that periodic power fluctuations are observed at time frequency of ~ 2 Hz, which is independent on the frequency modulation pattern used for an FMLO observation.

while that of FMLO is $\eta_{\mathrm{obs,FMLO}} \simeq 0.92$ because only ON-point observations are allocated to the total observation time, but there exists settling time ($\lesssim 8$ ms) for each sampling time (100 ms) of spectrometer (see § 3.2). Taking these observation efficiencies, the sensitivity improvement of the FMLO method compared to that of PSW per unit total observation time, can be expressed as the following equation:

$$\iota = \frac{\sqrt{2}}{\alpha} \left(\frac{\eta_{\mathrm{obs,PSW}}}{\eta_{\mathrm{obs,FMLO}}} \right)^{-1/2} \tag{5.6}$$

In other words, this indicates that the FMLO observation requires only $1/\iota^2$ of total observation time compared to that of the PSW to achieve the same sensitivity of the final spectra.

Figure 5.17 and 5.18 show the final spectra of the FMLO method with atmospheric lines subtracted, and noise level curves evaluated from timestreams themselves, ones calculated by using the equation 5.4 (with $\alpha = 1$), and ones ex-

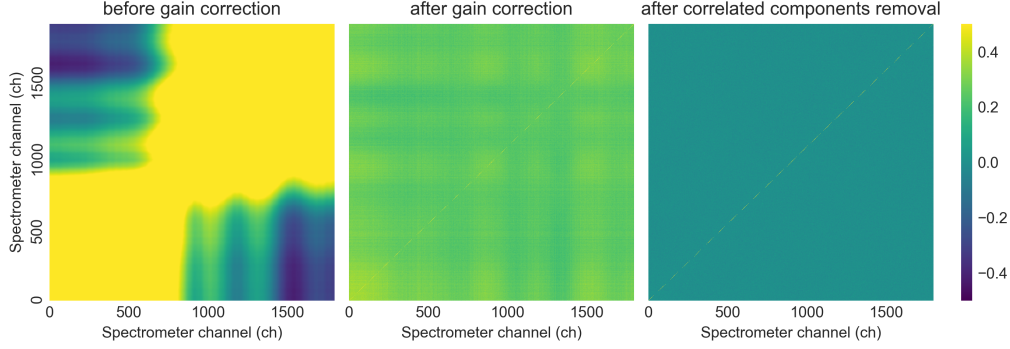**Figure 5.15:** The covariance matrices created by various timestreams of blank sky around 98 GHz (LSB): (left) the one created by $\boldsymbol{T}^{\mathrm{calib}}$ before gain correction (i.e., the first outer loop of the pipeline algorithm), (center) the one created by $\boldsymbol{T}^{\mathrm{calib}}$ after gain correction (the second outer loop), and (right) the one created by $\boldsymbol{T}^{\mathrm{a^*}}$. timestreams are normalized so that diagonal values of the derived covariance matrix are unity.

pected to achieve with PSW observations compared to the same observation times. The noise level curves of timestreams are estimated by the bootstrap method by randomly changing signs of samples of demodulated residual timestreams to re-sample the final spectra and derive the standard deviation. Since the number of samples ($\propto$ ON-source time) of each channel of demodulated timestreams depends on the FMP used (see § 5.1.1), the noise level gets worse near the edge of spectra.

As the results of both LSB and USB, the factor of noise contribution from correlated component removal is achieved to be $\alpha \sim 1.1$ over observed band, which is estimated by dividing green lines by red ones. In other words, *equivalent* noises from OFF-point are $\Delta T_{\mathrm{OFF}} = \sqrt{1.1^2 - 1^2}\,(T_{\mathrm{sys}}/\sqrt{\Delta\nu\,t_{\mathrm{ON}}}) \sim 0.46 T_{\mathrm{sys}}/\sqrt{\Delta\nu\,t_{\mathrm{ON}}}$, which means more than twice accurate estimates of in-situ baseline are achieved with the FMLO method.

The achieved improvement of sensitivity of the FMLO method according to the equation 5.6 is $\iota = 1.74$, or the FMLO observation requires only $1/\iota^2 = 33$ % of total observation time compared to that of the PSW to achieve the same sensitivity of the final spectra. In other words, we *equivalently* observe with a telescope whose system noise temperature is $(1 - 1/1.74) \sim 43$ % lower than the previous one.

In the actual observations, observation efficiencies of both FMLO and PSW method are lower than ideal ones. For example of blank sky observations we used
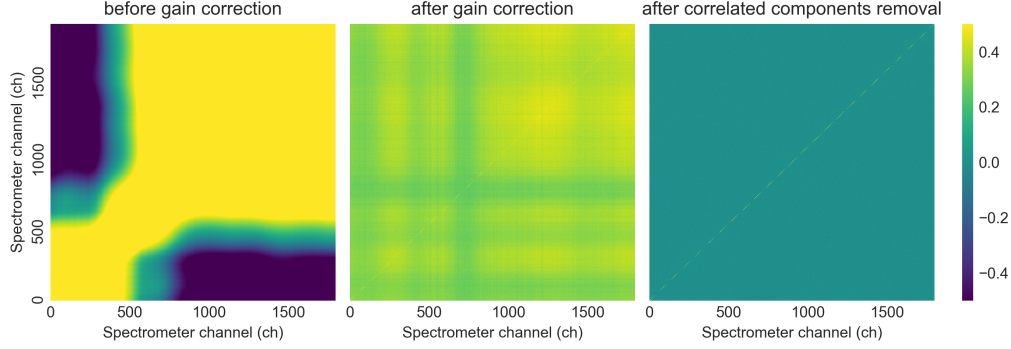
Figure 5.16: The covariance matrices created by various timestreams of blank sky around 110 GHz (USB): (left) the one created by T^{calib} before gain correction (i.e., the first outer loop of the pipeline algorithm), (center) the one created by T^{calib} after gain correction (the second outer loop), and (right) the one created by T^{a^*}. timestreams are normalized so that diagonal values of the derived covariance matrix are unity.

for the verifiction, $\eta_{\mathrm{obs,FMLO}}$ and $\eta_{\mathrm{obs,PSW}}$ are 0.69 and 0.42, respectively. This is because both observations are short (on-source time of 5 min) and the fractions of overhead such as preparation time before and after ON- and OFF-observations are large, compared to the typical scientific observations (on-source time of several hours). Using the values of actual observing efficiencies, however, we achieve the improvement as $\iota = 1.65$, which is almost same value as the ideal one. We also note that these improvement values are lower limit ones: $\eta_{\mathrm{obs,PSW}}$ is going to be much smaller because of larger fraction of telescope slue time between ON- and OFF-observations if we conduct a scientific observation where single observation time of ON- and OFF-point should be shorter (< 10 seconds, for example) for the better ON–OFF subtraction.

5.3.4 OPTIMAL FREQUENCY MODULATION PATTERN

For the reasons described in § 5.1.1, it is necessary to derive a guide to an optimal frequency modulation pattern (FMP) for an FMLO observation. Using timestream data of blank sky observed with various FMPs, we finally conduct simluations of FMLO observations to derive the guide by embedding artificial spectral lines of various intensities (i.e., different signal-to-noises) and line width

85

Figure 5.17: The final spectrum of blank sky around 98 GHz (LSB) with atmospheric line emission subtracted (light blue line). We also plot: (a) noise level curves evaluated from timestreams themselves (green line), (b) ones calculated by using the equation 5.4 (with $\alpha = 1$; red line), and (c) ones expected to achieve with PSW observations compared to the same observation times (purple line). The noise level curves of timestreams are estimated by the bootstrap method by randomly changing signs of samples of demodulated residual timestreams to resample the final spectra and derive the standard deviation. We derive the factor of noise contribution from correlated component removal, $\alpha \sim 1.1$ over observed band estimated by dividing (a) by (b).

in them. In the commissioning of Nobeyama 45 m, we obtained timestreams of blank sky with 34 different FMPs, which have different FM widths (100–6000 km/s at 98 GHz) and FM steps (8–250 km/s at 98 GHz) summarized in table 5.4 and 5.5. In order to eliminate spectral line emission from the atmosphere, we use timestreams of only 30 FMPs in LSB* because there exist strong ozone lines in the observed frequency range of USB (see figure 5.12). We then make model spectral lines of Gaussian and rectangular shapes whose line widths of 50, 100, and 300 km/s and peak intensities of 0.1 and 0.5 K, respectively, for simulations. The frequency at the center of these lines is 98.0 GHz in common. This means we conduct 360 (12 models × 30 FMPs) different simulations. The reasons we choose these parameters are as follows:

---

*We use *a part of* LSB timestreams (30 of 34) because an ozone line is located at the edge with FMPs of largest FM width. See also table 5.4
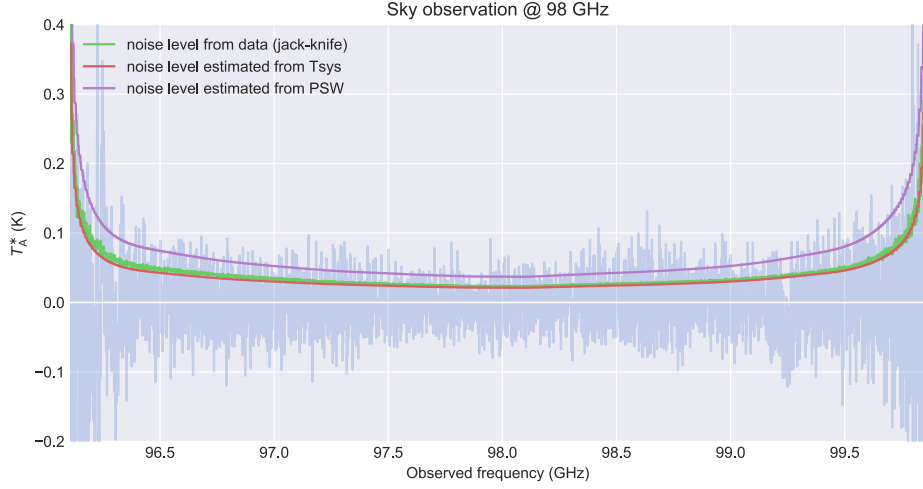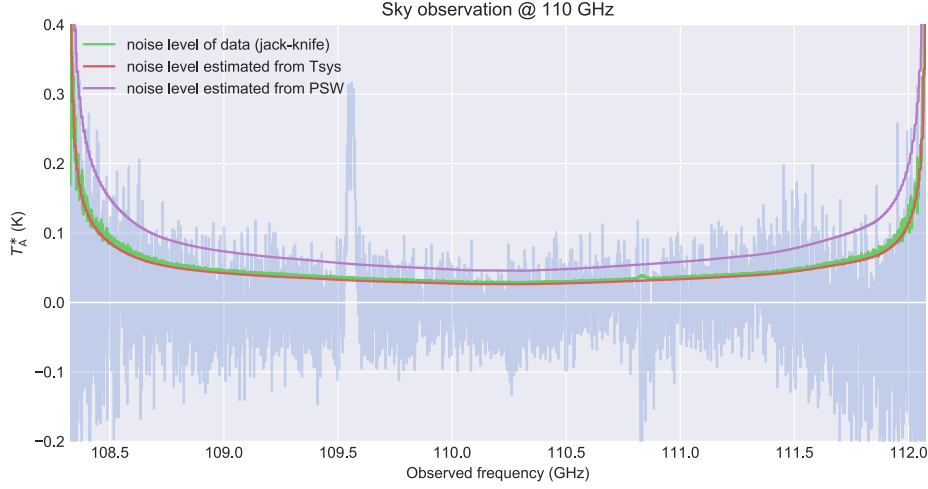
Figure 5.18: The final spectrum of blank sky around 110 GHz (USB) with atmospheric line emission subtracted (light blue line). We also plot: (a) noise level curves evaluated from timestreams themselves (green line), (b) ones calculated by using the equation 5.4 (with $\alpha = 1$; red line), and (c) ones expected to achieve with PSW observations compared to the same observation times (purple line). The noise level curves of timestreams are estimated by the bootstrap method by randomly changing signs of samples of demodulated residual timestreams to resample the final spectra and derive the standard deviation. We derive the factor of noise contribution from correlated component removal, $\alpha \sim 1.1$ over observed band estimated by dividing (a) by (b).

Gaussian: Gaussian and similar line shapes are uniformly observed in rotating objects. Because a Gaussian line has faint and wide skirts, we aim to confirm whether such shape of lower signal-to-noise is successfully reproduced in signal processing.

Rectangular: As well as Gaussian, rectangle-like shape are observed in expanding shells like stellar envelope. Because a rectangular line has steep rising at the edges of it, we aim to confirm whether such shape is successfully reproduced and also whether artificial components are *not* produced around the edges in signal processing.

Line widths: We aim to simulate FWHM line widths of spectral lines, Δv, from galactic star-forming region ($\Delta v \lesssim 50 \, \mathrm{km/s}$) to extragalactic giant molecular cloud or overall galaxy itself ($\Delta v \gtrsim 100 \, \mathrm{km/s}$).

87

Peak intensities: We aim to simulate peak signal-to-noise ratios of marginal (~ 5) and sufficient ~ 30 detections, which correspond peak instensities of $T_{\text{peak}} = 0.1$ and 0.5 K in the final spectra of blank sky observations, respectively (see also figure 5.17).

The method of each simulation is summarized in the following steps. We note that we start simulation *after* gain correction because the purpose of the simulations is to investigate only the effect of FMP onto correlated noise removal and modeling astronomical line emission, not for end-to-end pipeline itself.

Step 1: Reduce timestream data of a blank sky observation of a FMP to create a cleaned modulated timestream, $\boldsymbol{T}^{\text{Clean}}$, according to the signal processing described in chapter 4 (i.e., using the pipeline algorithm of § 4.5.4). We skip the modeling of atmospheric line emission because we pre-select a no-line data as mentioned above.

Step 2: Create a demodulated timestream, $\tilde{\boldsymbol{T}}^{\text{Clean}}$, and embed a model line spectrum $\tilde{\boldsymbol{s}}^{\text{model}}$ into each time sample of $\tilde{\boldsymbol{T}}^{\text{Clean}}$. Then re-modulate it and add a modulated timestream of correlated components, which revert it to a calibrated timestream, $\boldsymbol{T}^{\text{Calib}}$, with embedded model spectral line signals.

Step 3: Re-reduce data created by step 2 in the exactly same manner as step 1 to create a cleaned modulated timestream. In this step, however, model spectal line signals are expected to be included in it.

Step 4: Finally we make a spectrum of simulation, $\tilde{\boldsymbol{s}}^{\text{sim}}$, from the cleaned modulated timestream. Whether a line is reproduced properly after the simulation, we calculate a value of reduced χ^2 in the following equation:

$$\chi^2 = \frac{1}{\tilde{D}_{\text{in}}} \sum_{d=1}^{\tilde{D}_{\text{in}}} \left(\frac{\tilde{\boldsymbol{s}}_d^{\text{model}} - \tilde{\boldsymbol{s}}_d^{\text{sim}}}{\sigma} \right)^2 \tag{5.7}$$

where $\tilde{D}_{\text{in}}$ is the number of channels within $\pm 3\Delta v$ from the peak intensity of the model line (line region), and σ is typical noise level calculated from line-free regions corresponding $3\Delta v$ width outside both ends of the line region.

Figure 5.19: The results of spectral line simulations with six rectangular models ($\Delta v = 50, 100, 300$ km/s $\times$ $T_{\mathrm{peak}} = 0.1, 0.5$ K at 98.0GHz) embedded to timestream of blank sky observed with the best FMP (FM width is 1000 MHz and FM step is 80 MHz/sample). The FMP is the one with which the largest FM width and FM step are used, which yields the reduced χ^2 values of 0.87–1.1. Blue and green lines show the reproduced spectrum after signal processing and the model spectrum itself, respectively.

As results of all simulations, we obtain reproduced model spectra and their reduced χ^2 values. First of all, we find the best FMP within value ranges of FM width and steps in table 5.4 and 5.5: An FMP whose FM width is 1000 MHz and FM step is 80 MHz/sample, with which peak-to-peak value of reduced χ^2 of all 12 models is the smallest ($\chi^2 = 0.87 - 1.1$) among all FMPs. Figure 5.19 and 5.20 show the all spectra of reproduced models and models themselves, which denomstrate that models and simulations are consistent within the noise level. Taking all results into account, we then derive the guide for an optimal FMP (with which the best FMP agrees, of course) as follows:

Guide to FM width: An FM width *must* be wider than the FWHM line width, Δv, of an observed spectral line regardless of its peak intensity (i.e., signal-to-noise) and line shape. If an FM width is narrower than Δv, then the peak intensity of the reproduced line will be lower (or almost non-detection) than that of intrinsic value.
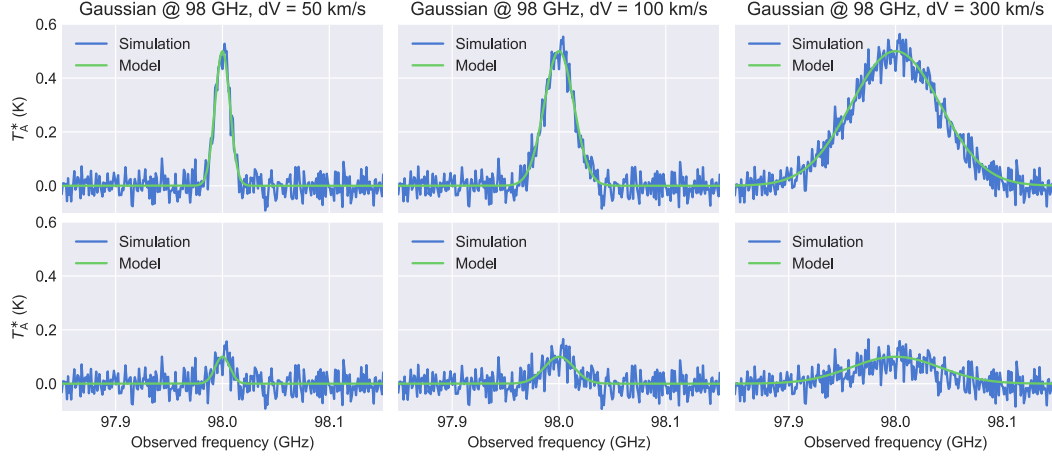
89
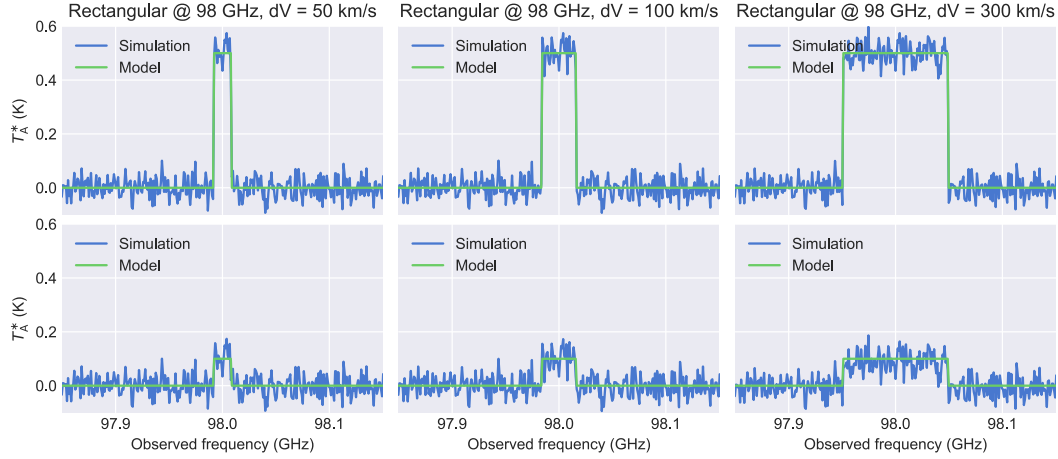
Figure 5.20: The results of spectral line simulations with six rectangular models ($\Delta v = 50, 100, 300$ km/s $\times$ $T_{\mathrm{peak}} = 0.1, 0.5$ K at 98.0GHz) embedded to timestream of blank sky observed with the best FMP (FM width is 1000 MHz and FM step is 80 MHz/sample). The FMP is the one with which the largest FM width and FM step are used, which yields the reduced χ^2 values of 0.88–1.1. Blue and green lines show the reproduced spectrum after signal processing and the model spectrum itself, respectively.

Guide to FM step: An FM step *should* be wider as much as possible in the using FM width. The value of an FM step doesn't affect the final peak intensity of the reproduced line, however, χ^2 value of *the first iteration* after correlated component removal will be better (closer to unity) if wider FM step is used.

The guide is led by reduced χ^2 values expressed as heatmaps. Figure 5.21 to 5.22 show the heatmaps of them with Gaussian model of various Δv and T_{peak}, which indicates that the reduced χ^2 is sensitive to the FM width. This trend is remarkable when FM width is smaller than Δv: In the case of $\Delta v = 300$ km/s, for example, the reduced χ^2 become drastically worse at FM width is 62.5 and 31.25 MHz (corresponding 191, 96 km/s), respectively. It is a reasonable result because line shape cannot be distinguished whether it is line or "base"line (one of correlated components) by PCA and the EMPCA and much amount of line shape still remains in a timestream of correlated components. On the other hand, it

seems that the value of FM step doesn't change the values of reduced χ^2 drastically. It affects, however, the values of *the first iteration* after correlated component removal as shown in figure 5.23 to 5.24. This suggests that narrower FM step may miss a faint line detection if we use $n\sigma$-cutoff method for modeling astronomical spectral line (see § 4.5.2) because the peak signal-to-noise at the first iteration may be lower than the threshold, θ_{cutoff}. The results of heatmaps of rectangular models, and all reproduced model spectra of each simulation are shown in the appendix A as Supplementary figures (A.1 to A.16).
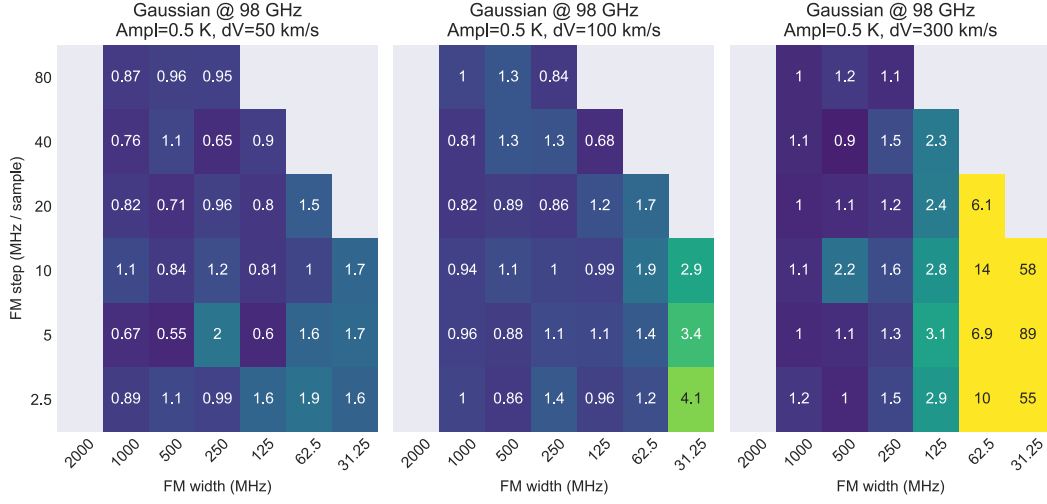
Figure 5.21: Heatmaps of reduced χ^2 between reproduced and model spectra of Gaussian models ($\Delta v = 50, 100, 300$ km/s from left to right, $T_{\text{peak}} = 0.5$ K at 98.0 GHz) calculated for various FMPs. The numbers in each cell are the values of reduced χ^2 which are derived using $\pm 3\Delta v$ frequency range as line region and $\pm[3\Delta v, 6\Delta v]$ as line-free regions for calculating noise level.

Figure 5.22: Heatmaps of reduced χ^2 between reproduced and model spectra of Gaussian models ($\Delta v = 50, 100, 300$ km/s from left to right, $T_{\text{peak}} = 0.1$ K at 98.0 GHz) calculated for various FMPs. The numbers in each cell are the values of reduced χ^2 which are derived using $\pm 3\Delta v$ frequency range as line region and $\pm[3\Delta v, 6\Delta v]$ as line-free regions for calculating noise level.
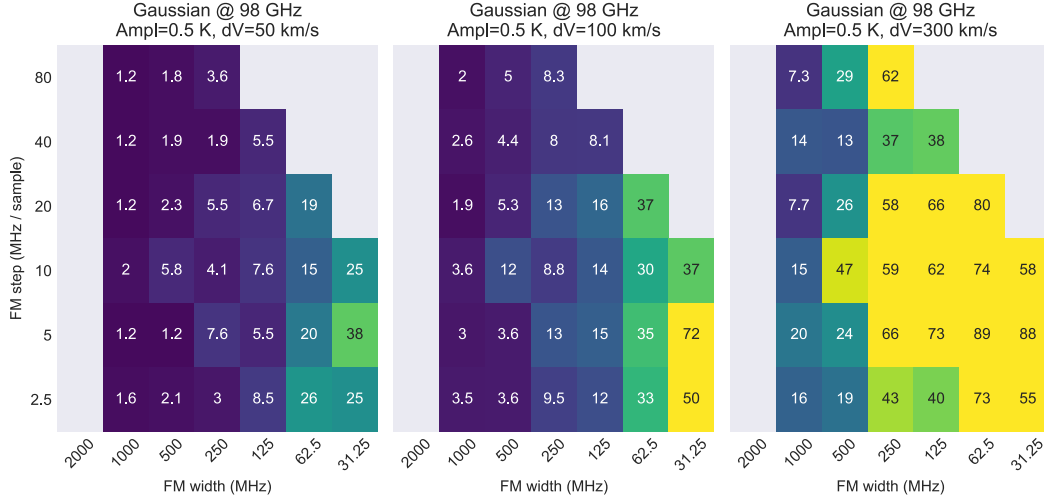
Figure 5.23: Heatmaps of reduced χ^2 after subtracting correlated components *at the first iteration* between reproduced and model spectra of Gaussian models ($\delta v = 50, 100, 300$ km/s from left to right, $T_{\mathrm{peak}} = 0.5$ K at 98.0 GHz) calculated for various FMPs. The parameters used for calculating reduced χ^2 are same as figure 5.21.

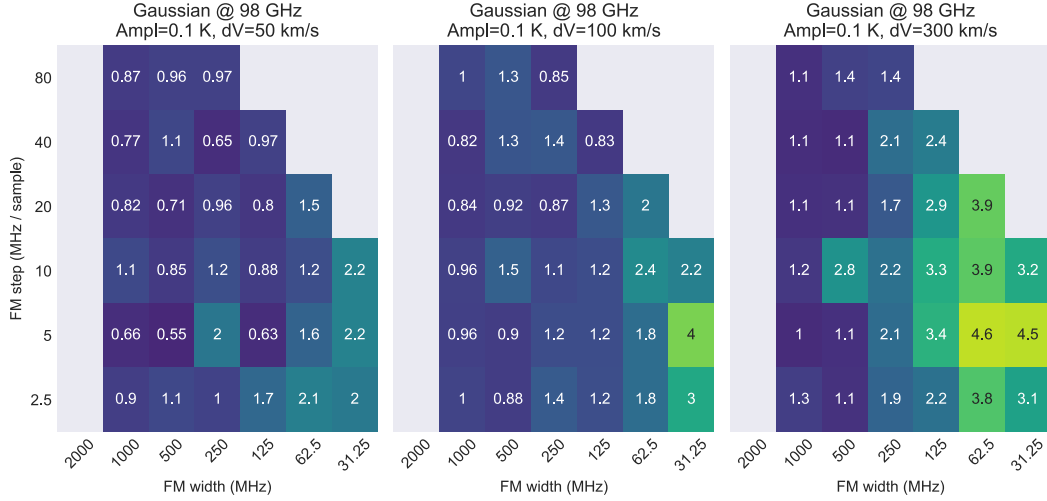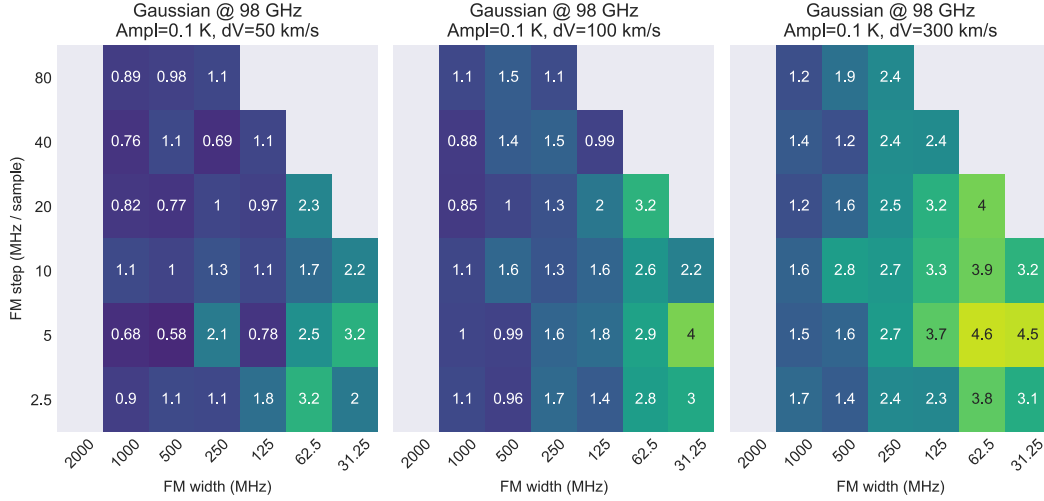**Figure 5.24:** Heatmaps of reduced χ^2 after subtracting correlated components *at the first iteration* between reproduced and model spectra of Gaussian models ($\delta v = 50, 100, 300$ km/s from left to right, $T_{\mathrm{peak}} = 0.1$ K at 98.0 GHz) calculated for various FMPs. The parameters used for calculating reduced χ^2 are same as figure 5.22.

No.	w1[†]	w2	w3	w4	w5	w6	w7
FM width (MHz)	2000	1000	500	250	125	62.5	31.25
FM width (km/s)	6120	3060	1530	765	382	191	96
Observed width (MHz)	4000	3000	2500	2250	2125	2062.5	2031.25
Observed width (km/s)	12200	9180	7650	6880	6500	6310	6210

Table 5.4: The frequency modulation (FM) widths and corresponding total observed frequency width of the spectrometer (SAM45) of Nobeyama 45 m used for the simulations. The corresponding widths in velocity, Δv, $(\simeq c\,\Delta\nu/\nu_{\mathrm{obs}})$ are also listed, where c is the speed of light in vacuum, $\Delta\nu$ is FM width in frequency, and ν_{obs} is observed frequency (98.0 GHz).

No.	s1	s2	s3	s4	s5	s6
FM step (MHz/sample)	80	40	20	10	5	2.5
FM step (km/s/sample)	245	122	61	31	15	7.6

Table 5.5: The frequency modulation (FM) steps used for the simulations. The corresponding steps in velocity, Δv, $(\simeq c\,\Delta\nu/\nu_{\mathrm{obs}})$ are also listed, where c is the speed of light in vacuum, $\Delta\nu$ is FM width in frequency, and ν_{obs} is observed frequency (98.0 GHz).

*There should be one – and preferably only one –
obvious way to do it. Although that way may not
be obvious at first unless you're Dutch.*

From the Zen of Python, by Tim Peters

6
Science Demonstration

This chapter describes the results of spectral and mapping observations with the FMLO method of astronomical targets which have bright ($T_A^* \sim 10^{-1} - 10^1$ K at peak) line emission in (sub)millimeter wavelength and thus usually observed for the science demonstration of a new instruments. Unlike the FMLO observations described in chapter 4, all the data of this chapter contain astronomical signals observed with the optimal frequency modulation pattern, and the resulting spctra and/or map should be compared with those observed with the conventional position switching (PSW) method for the consistencies in intensity, spectral shape, and spatial distribution (in the case of mapping). There exists, however, some pointing errors between the PSW and FMLO observations of the same target due to variations of wind speed and/or direction, and deformation of telescope dish. These error cannot be corrected because we cannot observe it simultaneously with both methods, which may result in an intensity fluctuation of spectral line emission between two observations. In the following sections, we therefore discuss the consintency of an FMLO observation with that of PSW one taking intensity fluctuation into consideration. The parameters and conditions of the both FMLO and PSW observations are summarized in table 5.1 and 5.2.

During the commissioning of the FMLO method, we carried out spectral line

observations toward three galactic targets: IRC +10216, Orion KL region, and IRAS 16293–2422 which are usually observed as "standard sources" for absolute intensity calibration of a spectral line observation. We also carried out mapping observations, but we only targeted Orion KL region because of time limitation in the commissioning periods. These targets are briefly summarized as follows:

IRC +10216 The IRC +10216 is a thick dusty envelope (stellar ejecta) of CW Leonis, a well-known carbon rich asymptotic giant branch (AGB) star closest to the Sun ($\simeq 130$ pc). Thanks to its proximity (apparent size of ~ 6 arcmin) and thus brightness, half of the known molecular species are detected in its envelope (Cernicharo et al., 2010), some of which have characteristic spectral shape reflecting expanding shell structure of the envelope. With the Nobeyama 45 m, the telescope beam size ($\sim$12 arcsec at 110 GHz) fully covers the overall structure of IRC +10216 and the observed molecular rotational lines of CS J=2–1 and ^{13}CO J=1–0 (hereafter we express them like ^{13}CO (1–0)) are expected to have that shape. The coordinates we observed in a spectral observation are $\alpha_{2000} = $ 9h47m57.406s, $\delta_{2000} = $ 13d16m43.56, which are listed in the 2MASS All Sky Catalog of point sources.

Orion KL region The Orion KL region is the central part of the H$_{\text{II}}$ region M42, which is located in the northern part of the Orion-A giant molecular cloud (GMC) at a distance of 400 pc (Menten et al., 2007). It contains the Orion KL (Kleinmann–Low) infrared nebula and the Trapezium stars ionizing the nebula, and the Orion Bar, one of photo-dissociation regions (PDRs) associated with the Trapezium. With both the Nobeyama 45 m and ASTE 10 m, the wide field ($\gtrsim$1 degree) spectral mapping observations were carried out including ^{12}CO (1–0), ^{13}CO (1–0), ^{18}CO (1–0), and neutral carbon, C$_\text{I}$ (Shimajiri et al. (2011), Shimajiri et al. (2013), Shimajiri et al. (2014), also see figure 6.1), thus it is suitable region for both spectral and mapping observations with the FMLO method. The coorinates we observed in a spectral observation are $\alpha_{2000} = $ 5h35m20, $\delta_{2000} = $ -5d23m50, which are $\sim$2 arcmin southeast of the Orion KL ($\alpha_{2000} = $ 5h35m14.50, $\delta_{2000} = $ -5d22m30.40; hereafter we call the point "Orion donut"). This is because the

region within $r < 1$ arcmin of the coorinates has a homogeneous distribution of CO line intensity and it is thus expected that the difference of the observed intensity between the PSW and FMLO observations is minimized due to the pointing errors. The mapping region for both OTF and FMLO observations is a 10×10 arcmin^2 square including both the Orion KL and Orion Bar structures. The position of Orion donut, Orion KL, and the mapping region are illustrated in figure 6.1.

IRAS 16293–2422 The IRAS 16293–2422 (hereafter IRAS 16293) is a protostellar (Class 0) binary system at a distance of 120 pc surrounded by an envelope. Several unbiased line surveys were carried out, one of which covered a range of around 200 GHz and detected more than 4000 lines (Caux et al., 2011). With the ASTE 10 m, the telescope beam size ($\sim$18 arcsec at 345 GHz) fully covers the overall structure of IRAS 16293. The coordinates we observed in a spectral observation are α_{2000} = 16h32m22.60s, δ_{2000} = -24d28m33.0s, which are listed in a webpage of the APEX calibration sources*.

---

*http://www.apex-telescope.org/heterodyne/shfi/calibration/apexSHeFICalPlan
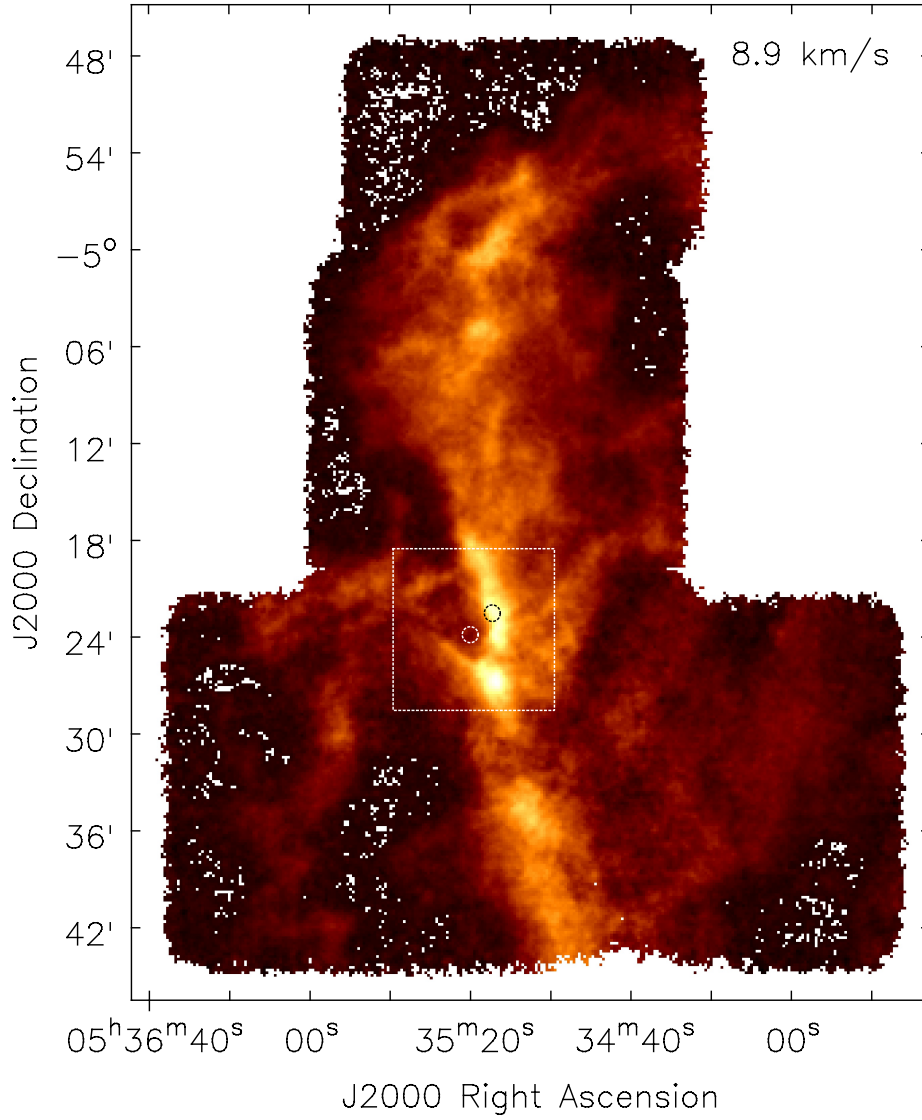
Figure 6.1: Overview of the Orion KL region. We plot the integrated intensity map of ^{13}CO (1–0) observed with Nobeyema 45 m (not our data but part of Shimajiri et al. (2014)). The FITS data is available at the Nobeyama 45 m Database (http://www.nro.nao.ac.jp/~nro45mrt/html/results/data.html). We indicate three regions: 10×10 arcmin^2 mapping region used for science demonstration (dashed white square), $r < 30$ arcsec region centered to Orion KL (dashed black circle), $r < 30$ arcsec region centered to Orion donut (dashed white circle).

Figure 6.2: The obtained CS (2–1) spectra of IRC +10216 observed with PSW (green line) and FMLO (blue one) methods at Nobeyama 45 m. We also plot various PSW spectra obtained around 60 minutes before and after the FMLO observation (gray lines) for monitoring typical pointing errors.

6.1   Spectral line observations

Here we present the result of spectral line observations of the FMLO and PSW method observed with both the Nobeyama 45 m ($\lambda \sim 3$ mm) and ASTE 10 m ($\lambda \sim 0.87$ mm). The the following resulting spectra were obtained with the FMLO observations using the optimal frequency modulation pattern (FMP) as is suggested in § 5.3.4 and with the conventional PSW observations which were carried out several times before and after each FMLO observation for checking intensity fluctuation due to the pointing errors. The output timestream data of ON-point, $\boldsymbol{P}^{\mathrm{ON}}$, were recorded at a rate of 10 Hz by the OTF mode. The obtained output timestream data, frequency modulation log files, and antenna log files (although no antenna driving during an observation) were offline-merged into FITS files by the `FMFlow`, the data analysis package for the FMLO method. Using FITS files, we reduced the data according to the end-to-end pipeline algorithm described in § 4.5 to make an FMLO spectra as final products. The program code for the pipeline is written in Python and functions of each signal processing (the EM-PCA, for example) are provided by `FMFlow` (see appendix C). Other observation conditions are same as described in § 5.1.3 and § 5.1.3.
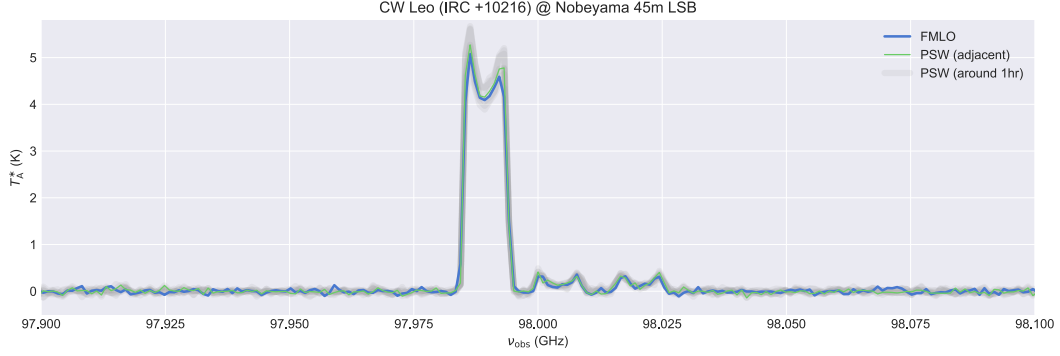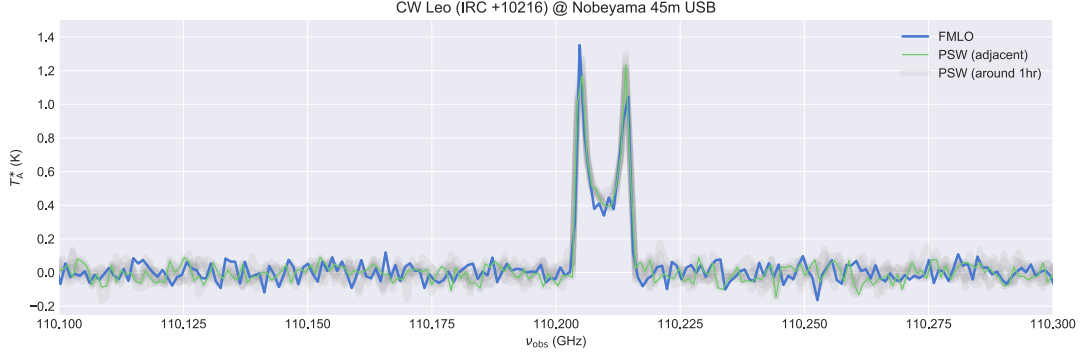
Figure 6.3: The obtained ^{13}CO (1–0) spectra of IRC +10216 observed with PSW (green line) and FMLO (blue one) methods at Nobeyama 45 m. We also plot various PSW spectra obtained around 60 minutes before and after the FMLO observation (gray lines) for monitoring typical pointing errors.

6.1.1 NOBEYAMA 45 M

We observed CS (2–1) ($\nu_{\text{rest}} = 97.980953$ GHz; in LSB) and ^{13}CO (1–0) ($\nu_{\text{rest}} = 110.20135$ GHz; in USB) of IRC +10216 with the FMP whose FM width is 250 MHz and FM step is 80 MHz/sample with Nobeyama 45 m. The FMP fulfills the conditions of the optimal FMP because the line width (FWZI) of IRC +10216 is expected to be $\sim$ 40 km/s (13 MHz) from the past PSW observation. The ON-source time was 40 seconds (400 samples) and the achieved noise levels of the FMLO observation per spectral channel were 0.04 K (LSB) and 0.05 K (USB), respectively. Around 1 hour before and after the FMLO observation, we carried out 8 times of PSW observation with the same observation conditions as the FMLO one. Within each observation, we obtained 10 seconds of ON and OFF-point observations 4 times by turns to achieve the ON-source time of 40 seconds. The coordinates of OFF-point is 6 minutes west from the ON-point.

Figure 6.2 and 6.3 are the result spectra of the FMLO observation of CS (2–1) and ^{13}CO (1–0), and PSW ones. As the result of comparison between the FMLO and PSW spectra, both intensity and line shape of the FMLO spectra are consistent of those of PSW which were observed adjacent to the FMLO observation. We also confirm that the FMLO spectra of both LSB and USB are within peak-to-peak of the around-1-hour PSW observations (light gray lines). These results suggest that the intensity can be easily changed within a hour beyond the noise

Figure 6.4: The obtained CO (3–2) spectra of Orion donut observed with PSW (green line) and FMLO (blue one) methods at ASTE 10 m. The region is indicated as dashed white circle in figure 6.1. We also plot various PSW spectra obtained around 30 minutes before and after the FMLO observation (gray lines) for monitoring typical pointing errors. The slight difference between two spectra is due to line contamination from OFF-point in the spectrum of PSW method.

level (more clearly seen in CS (2–1)) when we see a point-like source, and it is thus necessary to confirm the consistency of the FMLO method with "time series" spectra of PSW ones if we demonstrate the FMLO method in deeper spectral observation (mK order of noise level) or in other telescope in the future.

6.1.2 ASTE 10 M

We observed CO (3–2) ($\nu_{\rm rest}$ = 345.79599 GHz; in LSB) of the Orion donut and IRAS 16293 with the FMP whose FM width is 256 MHz and FM step is 64 MHz/sample with ASTE 10 m. The FMP fulfills the conditions of the optimal FMP because the line widths (FWZI) of the Orion donut and IRAS 16293 are expected to be $\sim$ 20 km/s (23 MHz) and $\sim$ 40 km/s (46 MHz), respectively from the past PSW observations. The ON-source times were 51 seconds (510 samples) and the achieved noise levels of the FMLO observation per spectral channel were 0.03 K. Around 30 minutes before and after the FMLO observation, we carried out 6 times of PSW observation with the same observation conditions as the FMLO one. Within each observation, we obtained 10 seconds of ON and OFF-point observations 5 times by turns to achieve the ON-source time of 50 seconds. The coordinates of OFF-point are 30 minutes east from the ON-point in
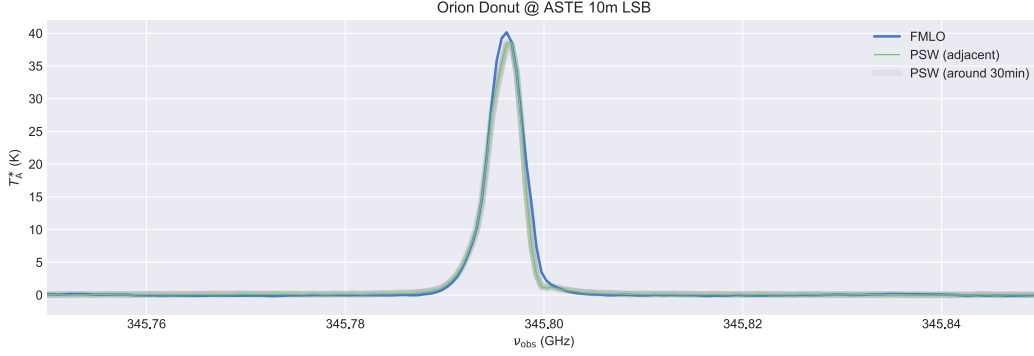
101

Figure 6.5: The obtained CO (3–2) spectra of Orion donut observed with PSW (green line) and FMLO (blue one) methods at ASTE 10 m. The region is indicated as dashed white circle in figure 6.1. We also plot various PSW spectra obtained around 30 minutes before and after the FMLO observation (gray lines) for monitoring typical pointing errors. Unlike figure 6.4, we show the PSW spectrum with line contamination subtracted from OFF-point by masking line region and linear interpolation to re-difine the baseline of OFF-point data.

the case of Orion donut, and 30 minutes west in the case of IRAS 16293. Note that we find that we mistook to use improper coorinates of OFF-point for Orion donut. An OFF-point (line-free position) of Orion-A GMC should be placed more than 2 degree away from the mapping area because of extent emission of it. This misplacement causes decreasing of intensity of PSW spectra. We also note that there exists the atmospheric CO (3–2) line located within the frequency range of CO (3–2) of Orion donut, which may also change the intensity. With these caveats, however, we try to correct line contamination from OFF-point by identifying and subtracting these lines in the OFF-point spectrum before intensity calibration.

Figure 6.4 and 6.5 are the result spectra of the FMLO observation of CO (3–2) and PSW ones before and after correcting the line contamination. As the result of comparison between the FMLO and PSW spectra in figure 6.4, intensity of the FMLO spectrum seems to be consistent with that of PSW in the most of frequency range, but is not consistent at around the peak and right skirt where CO (3–2) emission of OFF-point exists. After correcting the contamination by masking line region and linear interpolation to re-difine the baseline of OFF-point data (figure 6.5), both intensity and line shape are now almost consistent with
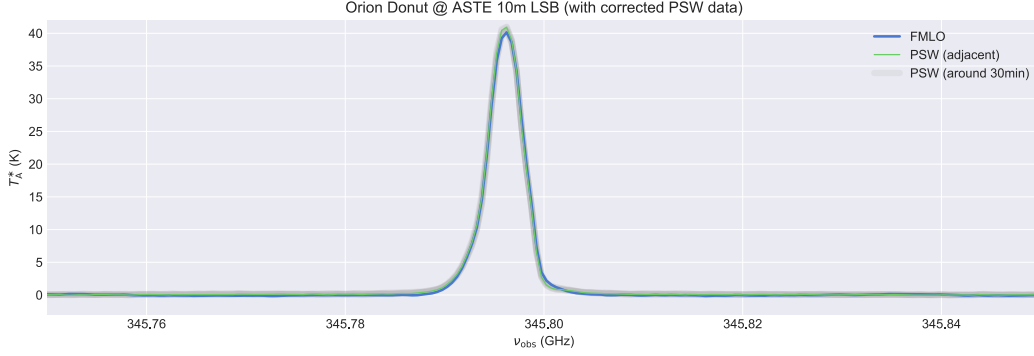
102
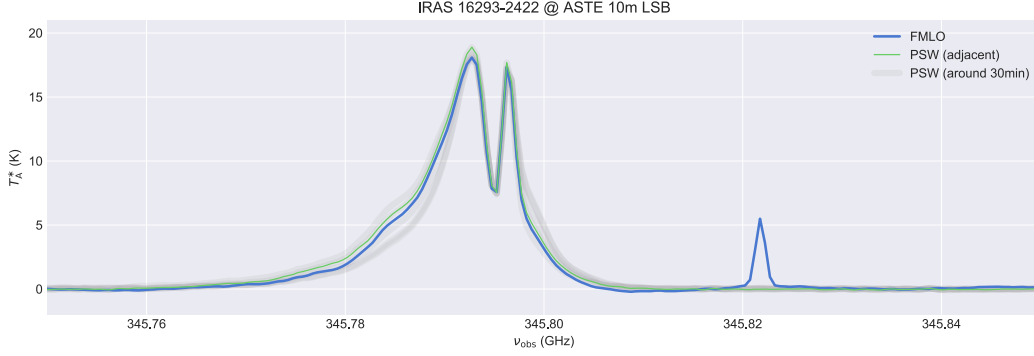
Figure 6.6: The obtained CO (3–2) spectra of IRAS 16293 observed with PSW (green line) and FMLO (blue one) methods at ASTE 10 m. We also plot various PSW spectra obtained around 30 minutes before and after the FMLO observation (gray lines) for monitoring typical pointing errors. Atmospheric CO (3–2) is detected only in the FMLO spectrum at 345.82 GHz.

that of adjacent PSW one. We also confirm that the FMLO spectrum is within peak-to-peak of the around-30-minute PSW observations (light gray lines).

We note that the obtained FMLO and (corrected) PSW spectra are composed of both CO (3–2) from Orion donut and atmosphere, which may slightly change the intrinsic intensity of CO (3–2) from Orion donut. Although modeling such totally overlapping atmospheric line is difficult, we can solve this by observing the target in another season or time where radial velocity of the target is different. This is demonstrated in figure 6.6, the result spectra of the FMLO observation of CO (3–2) and PSW ones of IRAS 16293. In the same manner as descrived above, we confirm that both intensity and line shape of the FMLO spectrum is consistent with the PSW ones (adjacent spectrum and 30-minute fluctuation). In this case, however, the atmospheric CO (3–2) is detected in the FMLO spectrum at $\nu_{\mathrm{obs}} = 345.82$ GHz outside of CO (3–2) spectrum of IRAS 16293. This is because the coordinates of azimuth and elevation, and observed time was different from those of Orion donut, which changes frequency of atmospheric CO (3–2) in the observed frequency frame. These results suggest that observer should consider carefully a possibility of atmospheric line contamination by aranging observed time or season to avoid it. Such issue may not be a problem, though, in the case of FMLO mapping observation where atmospheric line emission is expected to be
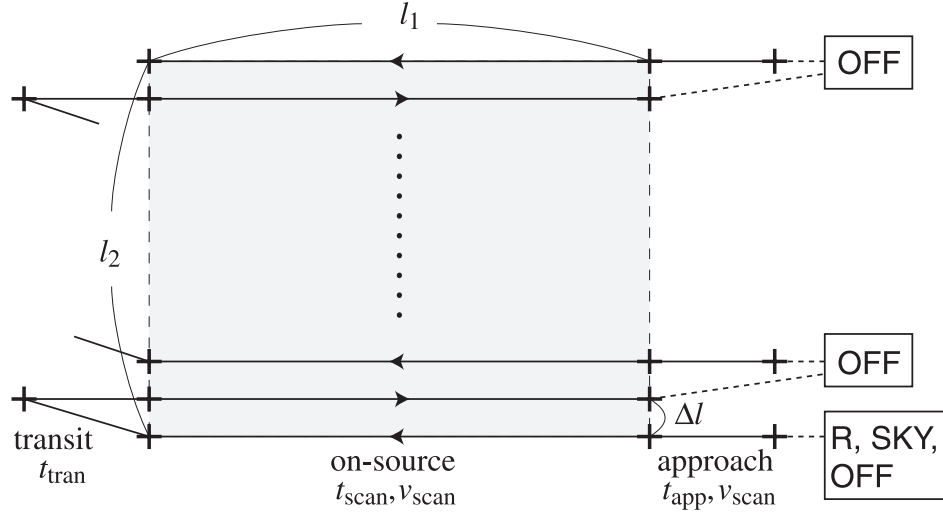
Figure 6.7: The schematic diagram of an OTF observation taken from Sawada et al. (2008). An OTF mapping is composed of (1) ON-source scans where the telescope sweep the mapping area of $l_1 \times l_2$ along with x or y-direction, (2) transits and approacies which are nessary to be inserted between ON-point scans in order to keep constant scan speed, v_{scan}, (3) OFF-point observations and transitions from/to the OFF-point. With an FMLO mapping, observing efficiency is expected to be improved because (3) is no longer necessary.

homogeneous within the mapping area while that of astronomical is not. This will be discussed in the following section.

6.2   MAPPING OBSERVATIONS

Here we present the result of mapping observations of the FMLO and on-the-fly (OTF) method observed with Nobeyama 45 m ($\lambda \sim 3$ mm). As described in § 2.5.2, we obtain a timestream data of 10 Hz with both OTF and FMLO method according to a scan pattern which controls how to sweep a mapping region as a function of time. In this commissioning, we use a raster scan pattern with which the telescope sweeps several times along with right ascension (RA) or declination (Dec) directions of equatorial coordinates. Figure 6.7 is an illustration of a raster scan pattern of RA direction (taken from Sawada et al. (2008)), where a mapping region is $l_1 \times l_2$ rectangle shape and several scans are carried out with declination

interval of Δl. In addition to these scans, transit and approach run (running times of $t_{\mathrm{tran}}, t_{\mathrm{app}}$) are inserted between two scans. This is because the antenna moving speed within a scan is expect to constant in order to achieve constant ON-point integration time per unit area, and such heavy structure of the telescope antenna (~ 700 tons of Nobeyama 45 m, for example) requires a runway before a scan. In an OTF observation, we take an OFF-point observation per several scans while in a FMLO observation we don't, which is only the difference of scan pattern between OTF and FMLO method, and it contributes to an improvement of observation efficiency ($\eta_{\mathrm{obs}} = t_{\mathrm{ON}}/t_{\mathrm{Total}}$). This will be further discussed using the actual data of Nobeyama 45 m in the following subsection. With both OTF and FMLO method, we carried out two mapping observations with raster scan patterns along with RA and Dec directions for each method (also see figure 6.8). This is because two maps should be combined to minimize the so called "scanning effect" using the basket-weaving method (Emerson & Graeve, 1988) after data reduction.

After OTF observations of Nobeyama 45 m, we use the data reduction software `NOSTAR`[†]. Each timestream dataset was corrected their spectral baseline with the `Base (Batch)` tool and then converted to a map (3D cube) with the `Make Map` tool with a Bessel-Gauss gridding convolution function (GCF) of default parameter of $a = 1.55, b = 2.52$ (Sawada et al., 2008) and a spacial grid size of $d = 10$ arcsec. On the other hand, after FMLO observations of Nobeyama 45 m, the obtained output timestream data, frequency modulation log files, and antenna log files were offline merged into FITS files by the `FMFlow`, the data analysis package for the FMLO method. Using FITS files, we reduced the data according to the end-to-end pipeline algorithm described in § 4.5 to make an FMLO maps as final products with the same GCF and spatial grid size as OTF observations. We note that a differences of the data reduction of FMLO mapping observations from that of spectral line observations is the length of total observation time: While spectral line observations demonstrated above are less than 1 minute, a mapping observation takes more than 30 minutes for observing 10×10 arcmin^2 region with both OTF and FMLO methods. We thus conduct a time-chunk process

[†]http://www.nro.nao.ac.jp/~nro45mrt/html/obs/otf/export.html

of correlated component removal and modeling atmosphric line emission every 1 minute (600 samples in each chunk) as described in § 4.5.3. Other observation conditions are same as described in § 5.1.3 and § 5.1.3.

6.2.1 Nobeyama 45 m

We observed CS (2–1) ($\nu_{\mathrm{rest}} = 97.980953$ GHz; in LSB) and ^{13}CO (1–0) ($\nu_{\mathrm{rest}} = 110.20135$ GHz; in USB) of Orion KL 10×10 arcsec^2 region with raster scan patterns of RA and Dec directions and with the FMP whose FM width is 120 MHz and FM step is 40 MHz/sample with Nobeyama 45 m. The FMP fulfills the conditions of the optimal FMP because the these lines' width (FWZI) of Orion KL are expected to be ~ 40 km/s (15 MHz) from the past PSW observation. The parameters of raster scan patterns of both RA and Dec directions are summarized in table 6.1. The typical system noise temperatures, T_{sys}, during these observations are 230 K (LSB) and 320 K (USB), which are larger than those of OTF observations. As will be further described, the ON-source time per spatial grid was 2.66 seconds (a factor of 92 % is included) and the achieved noise levels of the FMLO observation per spectral channel were 0.18 K (LSB) and 0.23 K (USB), respectively, after applying map making and basket-weaving methods. Before and after two FMLO mapping observations, conventional OTF observations were carried out (that of RA direction before, and that of Dec direction after two FMLO observations). The typical T_{sys} during these observations are 210 K (LSB) and 270 K (USB). The ON-source time per spatial grid was 2.90 seconds and the achieved noise levels of the FMLO observation per spectral channel were 0.15 K (LSB) and 0.17 K (USB), respectively, after applying map making and basket-weaving methods. The coordinates of OFF-point is 30 minutes east from the center of the mapping region. This distance is same as the CO (3–2) spectral line observation with ASTE, which might raise the same issue about line contamination from OFF-point. This will be discussed later in figure 6.12, the pixel-to-pixel correlation between OTF and FMLO maps.

Before combining two FMLO maps of RA and Dec raster scans, we must model and subtract line emission from the atmosphere because each map was obtained

106
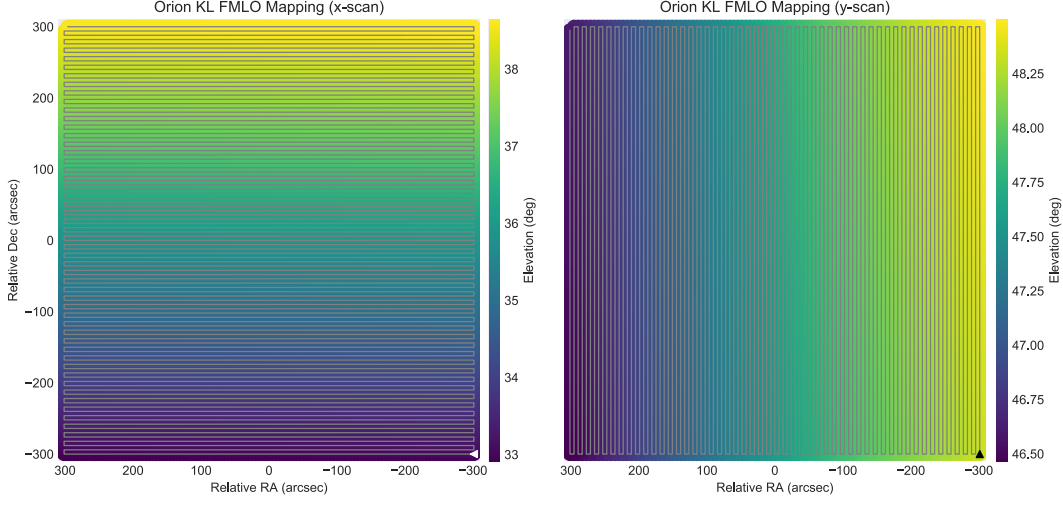
Figure 6.8: The scan patterns and the telescope elevations at the observed time of 10×10 arcmin^2 Orion region of both x-scan (RA direction) and y-scan (Dec direction), respecively. The scan patterns are plotted as solid lines of 101 raster scans (those of transition, approach, and OFF-point are not plotted), which start at the points of white and black triangle marker, respecively. The telescope elevation are expressed as color maps, which change by about 6 deg in x-scan and 2 deg in y-scan after the observations, respecively.

with different telescope's elevation, and thus elevation dependency of line intensity is expected (see also § 4.5.3). Figure 6.8 and 6.9 show how the telescope elevation changes during an observation and the spatial ditribution of peak intensity of ozone spectrum at $\sim$ 111 GHz. As is shown more remarkably in the raster scan of RA direction (x-scan), the peak intensity of the line decreases as telescope elevation gets higher. On the other hand, the peak intensity doesn't change largely in the raster scan of Dec direction (y-scan) because telescope elevation is higher and peak-to-peak elevation change is three times smaller than those of x-scan. These results also demonstrate that modeling atmospheric line emission in the pipeline works properly in these FMLO observations.

After subtracting atmosphric line emission and applying basket-weaving, we now obtain a final map (3D cube) of FMLO which is expected to be consistent with that of OTF method (and also T_A^*). Figure 6.10 and 6.11 show the obtained LSB and USB spectra of OTF and FMLO method avaraged within $r < 30$ arcsec
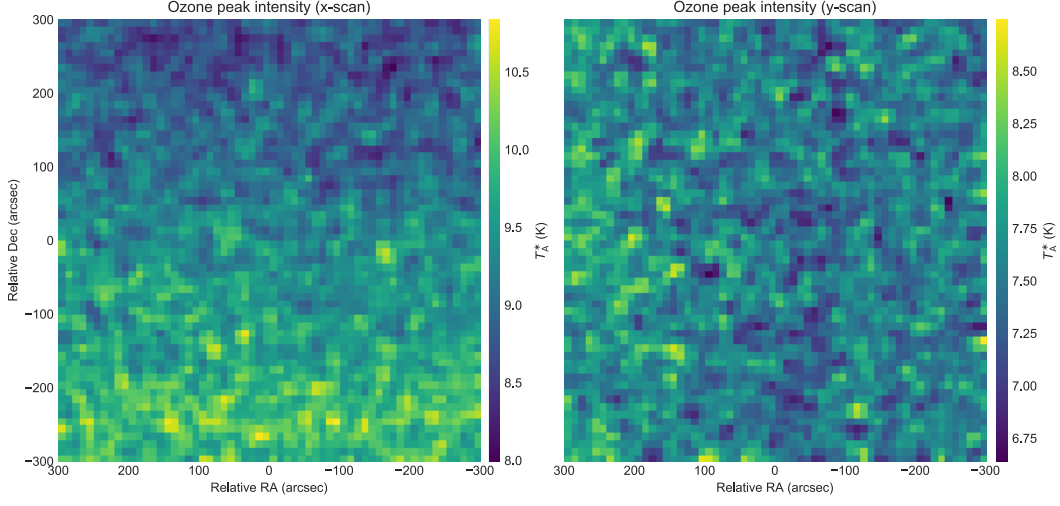
Figure 6.9: The peak intensity maps of ozone spectrum at $\nu_{\mathrm{obs}} = 110.85$ GHz (see also figure 6.11) which are iteratively reproduced by modeling atmospheric line emission by `am`. We demonstrate that the value of instensity increases as the telescope elevation decreases as shown in figure 6.8.

region centered with Orion KL. Comparing spectra between OTF and FMLO, we demonstrate that the obtained FMLO spectra of both LSB and USB is almost consistent with that of OTF. We also demonstrate that the subtraction of atmospheric line emission (atmospheric ozone in this case) works properly and no line emission remains in the basket-weaved spectrum. Figure 6.13 and 6.14 show integrated intensity maps of CS (2–1) and ^{13}CO (1–0) created from x-scan, y-scan, and basket-weaved 3D cubes. With comparisons between OTF and FMLO maps of each row, overall spatial distribution and intensity of the FMLO maps is almost consistent with that of the OTF maps in both ^{13}CO (1–0) and CS (2–1), respectively. Moreover, we demonstrate that scanning effect (one of "correlated" components) seems to be removed in each raster scan of single direction, while the large scanning effect ramains in x and y-scan of OTF maps along with their scan patterns before basket-weaving method (as is seen more remarkably in USB). After basket-weaving, both strong and weak structures seem to be now consistent with each other. We note that the overall structures seem to be slightly shifted between four maps of OTF/FMLO x/y-scans, respectively, which indicates that

Figure 6.10: The mean spectra of USB derived within $r < 30$ arcsec circle centered to Orion KL (the dashed circle in figure 6.1) of the OTF (green line) and FMLO (blue one) observation, respectively.

there exist pointing errors between them. We estimate the maximum pointing error by comparing the pixel coordinates of maximum intensity values, which result in at most 10 arcsec (1 pixel) of distances are possible to be shifted each other. If we observe a point-like source in 110 GHz (FWHM beam size of 15 arcsec, assuming Gaussian shape) with pointing 10 arcsec away from the source, the intensity will be about 30 % of the intrinsic value ($\sim$ 3 times change). In the following analysis, we thus use 3σ noise level as a standard deviation value.

To confirm the consistency between OTF and FMLO mapping observation within several uncertainties (noise level, pointing errors, and intensity calibration), we create pixel-to-pixel correlation plots between them of both sidebands as is also demonstrated in Sawada et al. (2008) for the confirmation of consistency between OTF and PSW method. In the same manner as Sawada et al. (2008), we aim to confirm the consistency within the accuracy of a relative intensity calibration of 5%, which is a reproducibility of the intensity of the standard source. Figure 6.12 shows the pixel-to-pixel scatter plots of both sidebands and a line fit of $T_{\mathrm{A}}^*(\mathrm{FMLO}) = a\, T_{\mathrm{A}}^*(\mathrm{OTF}) + b$ to data points. The frequency range of pixels selected is the same as one used for creating integrated intensity maps of basket-weaved data ($-6.25 < v_{\mathrm{LSR}} < 24.25$ km/s). The 3σ noise levels of OTF and FMLO is used for calculating uncertainties of (a, b) in line fittings. As results of both LSB and USB, correlation coefficients (a) are 0.986 ± 0.005 (LSB) and 0.982 ± 0.005 (USB), which suggests that OTF and FMLO maps are consistent within 5%. We
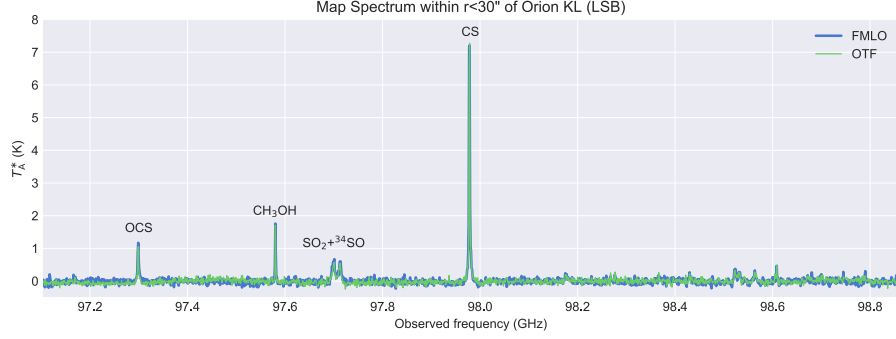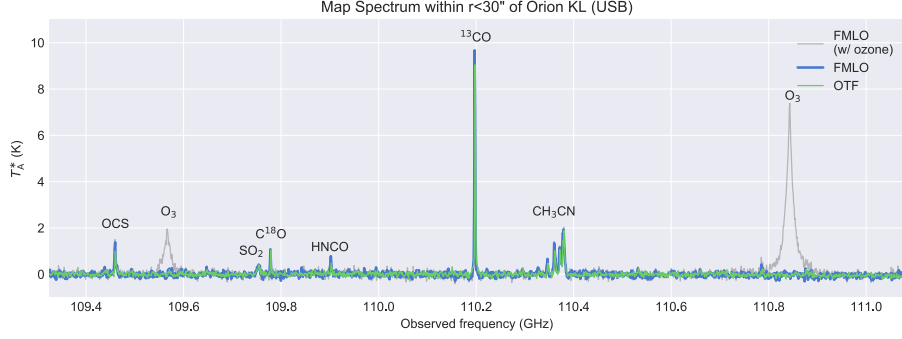
Figure 6.11: The mean spectra of USB derived within $r < 30$ arcsec circle centered to Orion KL (the dashed circle in figure 6.1) of the OTF (green line) and FMLO (blue one) observation, respectively. We also plot the FMLO spectrum of y-scan before subtracting atmospheric line emission of ozone. They demonstrate that there are no such line emission remaining in the final spectrum after the subtraction.

note that there exists relatively large vertical offset (b) in USB (0.373 ± 0.016) K. Although this values is smaller than 3σ noise level of the FMLO map, it is possible that a line contamination of ^{13}CO (1-0) from OFF-point decreases the intensity of OTF map while it is not the case with LSB because CS molecule traces denser region than CO (e.g., Nishimura et al. (2017) and reference therein). With the caveat, however, we confirm that the FMLO mapping method has an enough consistency of intensity *scaling* with the conventional OTF method.

Finally we demonstrate sensitivity improvements of the FMLO mapping compared to that of OTF in the same manner described in § 5.3.3. Again we introduce the sensitivity improvement, ι:

$$\iota = \frac{\alpha_{\text{OTF}}}{\alpha_{\text{FMLO}}} \left(\frac{\eta_{\text{obs,OTF}}}{\eta_{\text{obs,FMLO}}} \right)^{-1/2} \tag{6.1}$$

where η_{obs} is an observation efficiency of ON-source time over a total observation time, and α is a factor of noise contribution from OFF-point, which is related to an equation of achieved noise level:

$$\Delta T = \frac{\alpha \, T_{\text{sys}}}{\sqrt{\Delta\nu \, t_{\text{ON}}}} \tag{6.2}$$
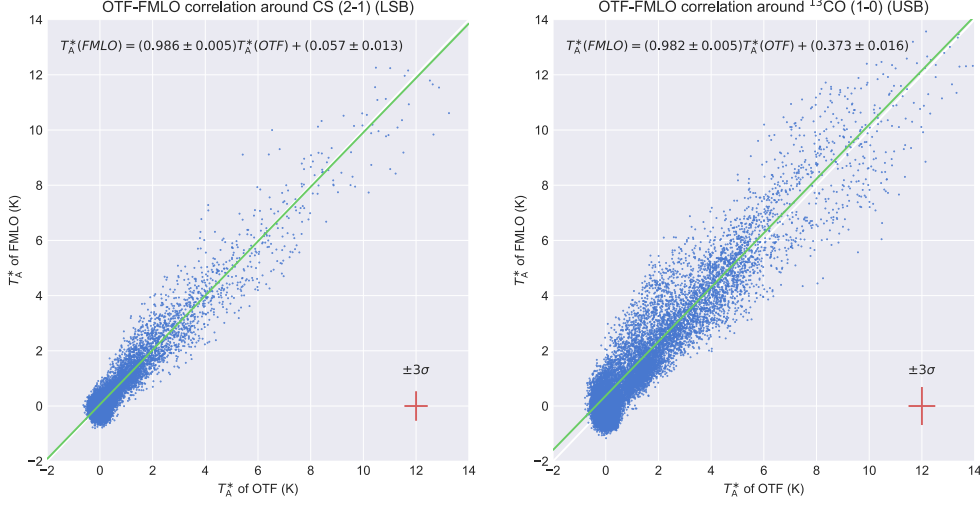
Figure 6.12: The pixel-to-pixel correlation plots between the OTF and FMLO mappings of both LSB and USB. Pixels are $d \times d \times \Delta\nu$ elements of a 3D cube with $d = 10$ arcsec, $\Delta\nu = 0.977$ GHz, and we plot pixels with velocity range of $v_{\mathrm{LSR}} = [-6.25, +24.25]$ km/s around CS (2–1) and ^{13}CO (1–0), respectively. Linear fits of $(y = ax + b)$ are conducted using orthogonal distance regression package in SciPy Jones et al. (01) with x and y errors of 3σ noise level derived from 3D cubes (see also table 6.2). The results of fits are displayed at the top of each panel.

For an FMLO mapping observation, we use $\alpha_{\mathrm{FMLO}} \simeq 1.1$ which is estimated from the comparison of achieved noise level and that calculated from T_{sys} in § 5.3.3. For a convetional ON-OFF observation, α_{OTF} is expressed as $\alpha_{\mathrm{OTF}} = (1 + t_{\mathrm{ON}}/t_{\mathrm{OFF}})^{1/2}$. We derive it by estimating achieved ON and OFF integration times per a spatial grid, $t_{\mathrm{cell}}^{\mathrm{ON}}$, $t_{\mathrm{cell}}^{\mathrm{OFF}}$ using equations introduced by Sawada et al. (2008)[‡]:

$$t_{\mathrm{cell}}^{\mathrm{ON}} = \frac{\eta d^2}{l_1 l_2} t_{\mathrm{tot}}^{\mathrm{ON}} \tag{6.3}$$

$$t_{\mathrm{cell}}^{\mathrm{OFF}} \simeq \frac{d}{\Delta l} t_{\mathrm{OFF}} \tag{6.4}$$

where $t_{\mathrm{tot}}^{\mathrm{ON}}$ is a total ON-source integration time of a mapping observation, t_{OFF} is an single integration time of a OFF-point, and η (not an observation efficiency)

[‡]mathematical expressions summarized in table 6.1 have same meanings used in it

is a factor determined by the extent of the used GCF. $t_{\text{tot}}^{\text{ON}}$ is a product of the number of scans, N_{row} $(= l_2/\Delta l + 1)$ and an observed time of a scan, t_{scan}. The value of η for a Bessel-Guass GCF with default parameters is 4.3 (Sawada et al., 2008). The values of $t_{\text{cell}}^{\text{ON}}$ and $t_{\text{cell}}^{\text{OFF}}$ are summarized in table 6.1, which yields $\alpha_{\text{OTF}} = 1.04$. As is summarized in table 6.2, we confirm that the calculated noise levels per spatial grid per frequency channel using equation 6.2 are almost consistent with those of actual values derived from 3D cubes themselves. We then derive observation efficiencies, $\eta_{\text{OBS}}^{\text{ON}}$ $(= t_{\text{tot}}^{\text{ON}}/t_{\text{tot}}^{\text{OBS}})$, of OTF and FMLO maps. Unlike spectral line observations (single-point), we need to take several overhead time such as transition and approach times into account. From Sawada et al. (2008), a total ON-source time, $t_{\text{tot}}^{\text{ON}}$, and total observation time, $t_{\text{tot}}^{\text{OBS}}$, can be expressed as follows:

$$t_{\text{tot}}^{\text{ON}} = N_{\text{row}} t_{\text{scan}} \tag{6.5}$$

$$t_{\text{tot}}^{\text{OBS}} = N_{\text{row}} \left(t_{\text{scan}} + t_{\text{OH}} + \frac{t_{\text{OFF}}}{N_{\text{scan}}^{\text{SEQ}}} \right) f_{\text{cal}} \tag{6.6}$$

where t_{OH} is an overhead time per a scan, $N_{\text{scan}}^{\text{SEQ}}$ is the number of scans taken between a pair of OFF-points, and f_{cal} is an overhead of chopper wheel calibration. t_{OH} can be expressed as the sum of several overhead terms:

$$t_{\text{OH}} = \frac{2t_{\text{tran}}^{\text{OFF}}}{N_{\text{scan}}^{\text{SEQ}}} + t_{\text{app}} + \frac{N_{\text{scan}}^{\text{SEQ}} - 1}{N_{\text{scan}}^{\text{SEQ}}} t_{\text{tran}} \tag{6.7}$$

First, second and third terms correspond to antenna slew times of OFF-point observation, approach, and transition per a scan. The values of these parameters are summarized in table 6.1. These yield $\eta_{\text{OBS}}^{\text{ON}} = 0.50$ with the FMLO map and 0.39 with that of OTF. Together with noise contribution, α, we achieve the sensitivity improvement of $\iota = 1.07$ and that for observation time of $\iota^2 = 1.15$ from these calculations. Moreover these values from actual $t_{\text{tot}}^{\text{ON}}$ and $t_{\text{tot}}^{\text{OBS}}$ are $\iota_{\text{real}} = 1.11, \iota_{\text{real}}^2 = 1.23$, which demonstrates that an FMLO mapping is 23% more efficient than that of OTF compared to unit noise level, even an OTF observation is more efficient than PSW observations to obtain each grid one after another.

We note that the mapping region we used for the commisioning (100 arcsec^2) is much smaller than the known typical mapping surveys by an order of magnitude (Shimajiri et al. (2014) conducted an observation of 1440 arcsec^2, for example). We will discuss what the value of ι will be achieved in such larger mapping observations in chapter 7.
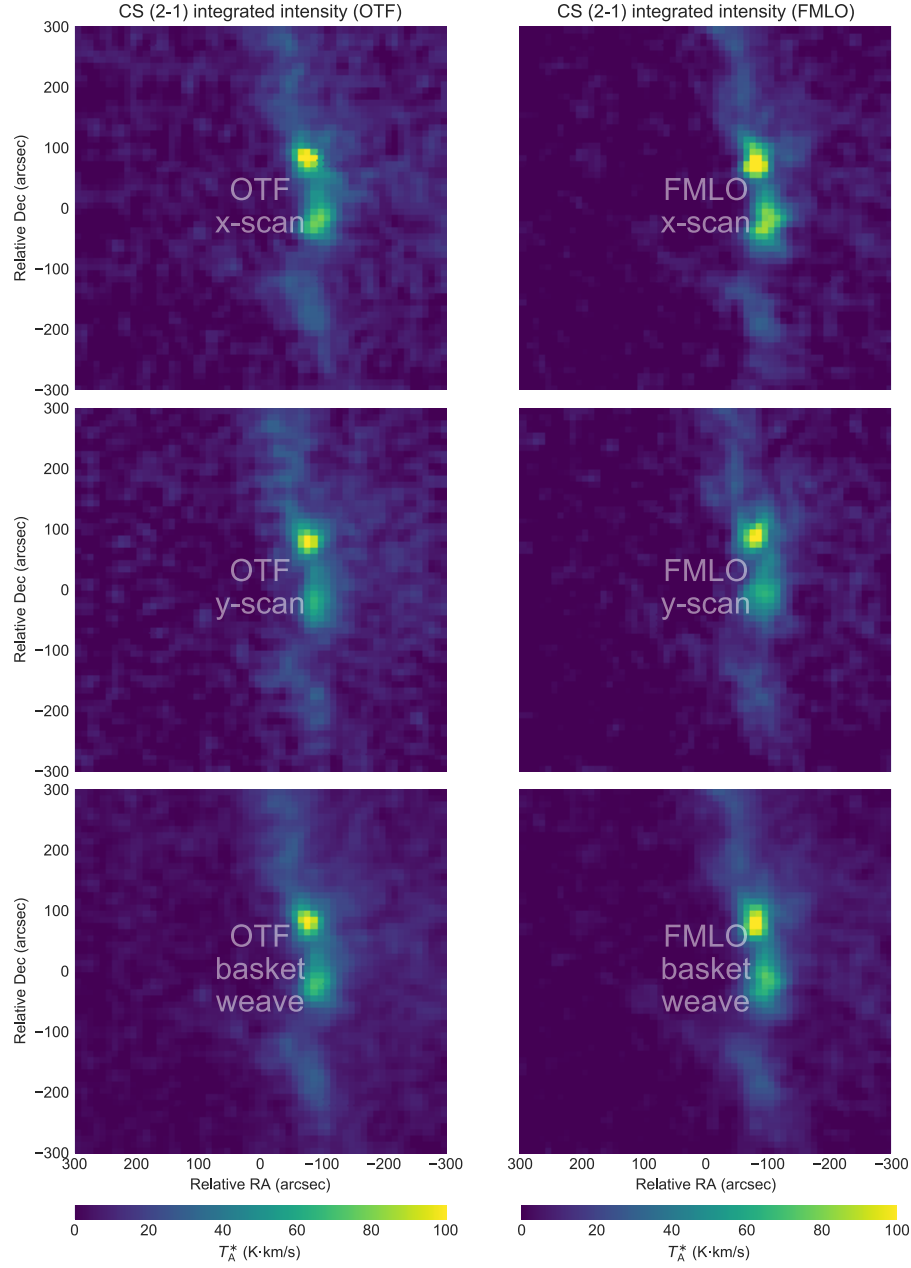
Figure 6.13: The integrated intensity maps of CS (2–1) of 10×10 arcmin^2 Orion region. The upper four panels are maps of single direction's scan with both OTF and FMLO methods integrated with velocity range of $v_{\mathrm{LSR}} = [-16.25, +34.25]$ km/s which contains both line and line-free regions. The bottom two panels are those after basket-weaving method to minimize the scanning effect, integrated with velocity range of $v_{\mathrm{LSR}} = [-6.25, +24.25]$ km/s.

114
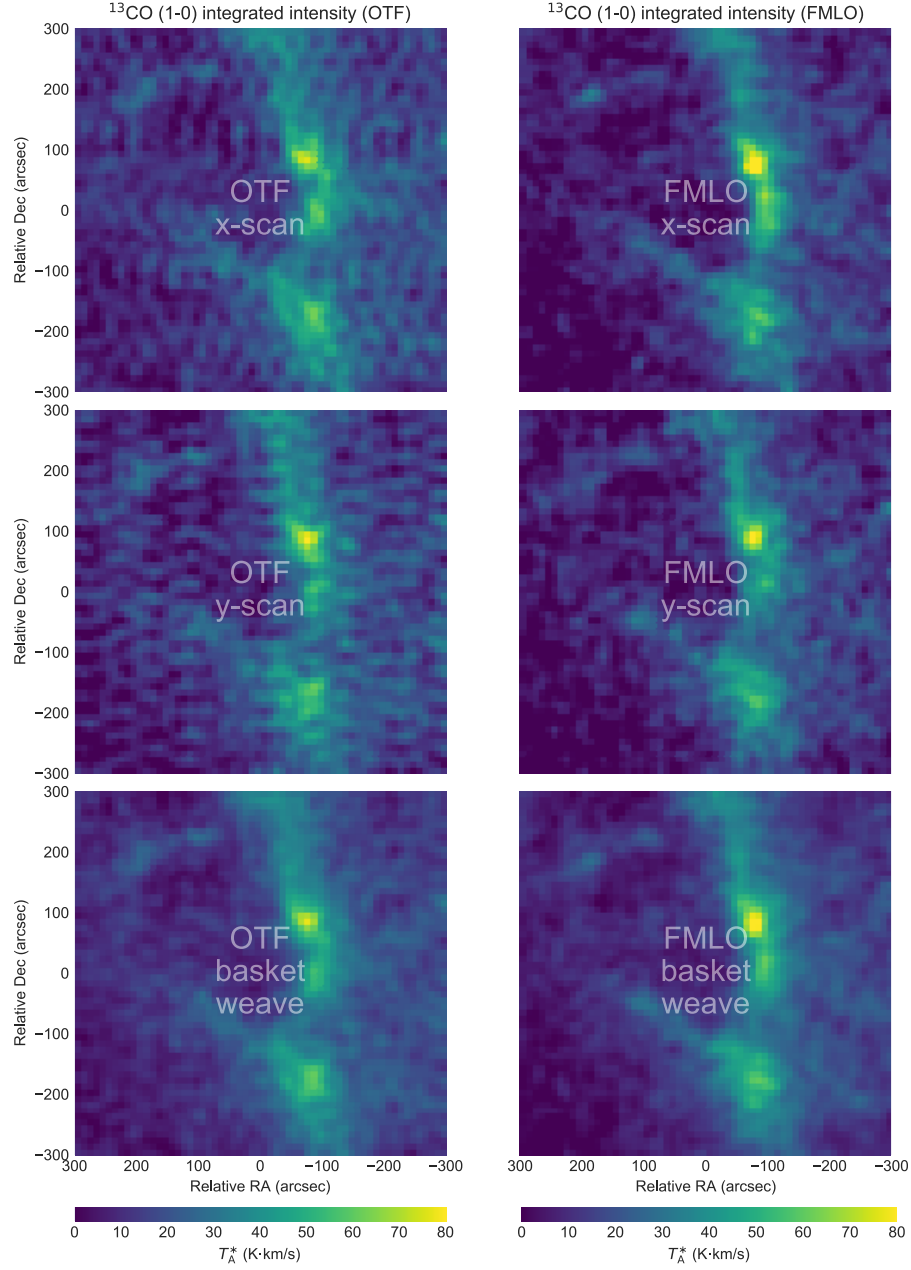
Figure 6.14: The integrated intensity maps of ^{13}CO (1–0) of 10×10 arcmin^2 Orion region. The upper four panels are maps of single direction's scan with both OTF and FMLO methods integrated with velocity range of $v_{\mathrm{LSR}} = [-16.25, +34.25]$ km/s which contains both line and line-free regions. The bottom two panels are those after basket-weaving method to minimize the scanning effect, integrated with velocity range of $v_{\mathrm{LSR}} = [-6.25, +24.25]$ km/s.

115

	OTF	FMLO
l_1 (arcsec)	600	600
l_2 (arcsec)	600	600
Δl (arcsec)	6	6
t_{scan} (second)	12	12
t_{tran} (second)	5	5
t_{OFF} (second)	12	**0**
$t_{\mathrm{tran}}^{\mathrm{OFF}}$ (second)	10	**0**
t_{app} (second)	5	5
$N_{\mathrm{scan}}^{\mathrm{SEQ}}$	3	**0**
f_{cal}	$\simeq 1$	$\simeq 1$
d (arcsec)	10	10
η	4.3	4.3
t_{OH} (second)	15.0	**10.0**
$t_{\mathrm{cell}}^{\mathrm{ON}}$ (second)	**1.45**	1.33
$t_{\mathrm{cell}}^{\mathrm{OFF}}$ (second)	20.0	**0**
$t_{\mathrm{tot}}^{\mathrm{ON}}$ (minutes)	**20.2**	18.6
$t_{\mathrm{tot}}^{\mathrm{OBS}}$ (minutes)	52.2 (58)	**37.0** (39)
$\eta_{\mathrm{OBS}}^{\mathrm{ON}}$	0.39 (0.35)	**0.50** (0.48)

**Table 6.1:** (top) the parameters of both OTF and FMLO mapping observations of 10×10 arcmin^2 Orion region. If the values are different between OTF and FMLO, the better one is displayed as bold symbol. (middle) the parameters of map making after obtaining mapping timestream data. η (not a observation efficiency) is a factor determined by the extent of the used GCF ($\eta = 4.3$ for Bessel-Gauss GCF with default parameters). (bottom) the derived values used for calculating observation efficiency. The values without parentheses are estimated ones, and with parentheses are actual ones from timestream data and observing log.

	OTF	FMLO
ΔT_{A}^* (LSB) (K)	0.13 (0.15)	0.16 (0.18)
ΔT_{A}^* (USB) (K)	0.17 (0.17)	0.22 (0.23)

Table 6.2: The standard deviation noise levels of OTF and FMLO observations for both LSB and USB. The values without parentheses are the estimated ones from equation 6.2–6.4. The values with parentheses are the ones derived from maps. Other parameters are: $\Delta \nu = 0.977$ MHz, $\alpha_{\mathrm{FMLO}} = 1.1$, and $\alpha_{\mathrm{OTF}} = (1 + t_{\mathrm{cell}}^{\mathrm{ON}}/t_{\mathrm{cell}}^{\mathrm{OFF}})^{1/2} = 1.04$.

Now is better than never.
Although never is often better than *right* now.

From the Zen of Python, by Tim Peters

7
Discussion

Here we summarize and discuss issues raised so far, and future prospects of the FMLO method. We discuss advantages and limitations of the FMLO method by referring the obtained results in the previous chapters (§ 7.1). Then we discuss the issues in terms of computation costs of the proposed signal processing, in particular, the correlated component removal by PCA and the EMPCA methods (§ 7.2). Finally we briefly discuss future prospects of both the FMLO method itself and the signal processing for other telescopes and new instruments (§ 7.3).

7.1 Advantages and limitations of the FMLO method

7.1.1 In-situ estimation of OFF-point

First of all, we confirm that the approach of removing correlated noises is applicable to the (sub-)millimeter spectroscopy as the FMLO method: The correlated noises (components) do exist in a timestream data of frequency modulation. In chapter 5, we demonstrate for the first time that correlated components still remain in a timestream after correcting a gain curve, and they are removed by a PCA and/or the EMPCA properly (see also figure 5.13, 5.14, 5.15, and 5.16 even

they are the results of only 5 minutes observation). This suggests that the baseline spectrum of OFF-point can be variable within typical ON–OFF switching interval ($\sim 5 - 10$ seconds) in the position switching (PSW) method, and it is thus necessary to obtain time-series data more than $\gtrsim 1$ Hz if we would like to remove all the contributions from such noises. We also confirm that the intensity and line shape of an astronomical spectral line are not affected by a correlated component removal by a PCA and/or the EMPCA if we could choose an optimal frequency modulation pattern (FMP) according to the guide described in § 5.3.4. In chapter 5 and 6, we denomstrate that the intensity and line shape of both artificial and astrinomical lines are consistent with those obtained with the conventional PSW method. Moreover we see that such in-situ estimation of OFF-point is an effective way to eliminate a "scanning effect" in a mapping observation with only a single direction of scan pattern. Finally we must mention that all these results are obtained without any OFF-point observations, which results in remarkable sensitivity improvements of both spectral and mapping observations of the FMLO methods ($\iota \simeq 1.7$ and 1.1, respectively) per unit observation time and noise level. The approach of spectral baseline subtraction by non-subtraction of OFF-point but modeling it in-situ is therefore necessary for us to beat the correlated noises from the atmosphere and obtain spectra of ideal noise level.

7.1.2 Application for large mapping observations

In chapter 5, we demonstrate that the sensitivity improvement of the FMLO mapping, is $\iota \sim 1.1$ (10 % of improvement) compared to an OTF one, which seems to be smaller amount of improvement in the case of spectral line (pointing) observation of the FMLO method ($\iota \sim 1.7$). This is because while the ON-point observation of the FMLO is 20–30 % more efficient, the noise contribution from OFF-point, α, is 5% worse than the OTF one. If α of FMLO is not getting better, $\alpha_{\mathrm{OTF}}/\alpha_{\mathrm{FMLO}}$ is getting worse (less than unity) for wider mapping area such as several square-degree survey. It is, however, expected that we will obtain still better ι for wider mapping area because there exists upper limit of scan length, l_1, observable at an OTF observation due to the upper limit of an observed time per a

scan, t_{scan}, while an FMLO observation has no such limits. According to "How to Determine Parameters"* of Nobeyama 45 m website, t_{scan} should be 10–30 seconds for a mapping observation of Nobeyama 45 m (recommended value of $t_{\text{scan}} = 20$ seconds) because (1) larger time interval between OFF-points causes a baseline wiggle similar to PSW method, and (2) longer t_{scan} (i.e., longer observation time of an entire map) no longer guarantee the uniformity of a map. Also there exists a lower limit of scan speed, v_{scan}, where spatial sampling interval should be 1/3–1/4 of beam size (HPBW). For a 115 GHz observation of Nobeyama 45 m to observe CO (1–0) line (beam size of 15 arcsec), for example, v_{scan} should be 50–60 arcsec/s and this yields an upper limit of l_1 of 1000-1200 arcsec. If we suppose to conduct 1×1 degree^2 mapping observations of both OTF and FMLO methods, OTF is necessary to split the mapping area into 9 different 20×20 arcmin^2 subregions. This yields an observation efficiency of $\eta_{\text{OBS}}^{\text{ON}} = 0.51$ while that of FMLO achieves $\eta_{\text{OBS}}^{\text{ON}} = 0.81$, much higher value if we use parameters described in table 7.1 †. Together with noise contribution factor, sensitivity improvent is $\iota = 1.17$ (17 % of improvement) and efficiency improvement per unit noise level is $\iota^2 = 1.36$ (36 % of improvement). This is because we assume that the FMLO mapping can break the upper limit of t_{scan} and sweep a scan length of 1 deg at a time ($t_{\text{scan}} = 72$ seconds). We note that the derived ι is lower limit: In actual obseration, we expect that the baseline wiggles and/or scanning effects are subtracted by correlated component removal, which will result in much higher ι and thus guarantees the uniformity of a map even wider (longer) scan length of 1 deg, as we partially demonstrate in § 6.2.

7.1.3 Continuum and broader line observations

In chapter 5, we demonstrate that an optimal FMP depends on a line width (FWHM) of a target. This, however, suggests that we need to know the intrinsic line width of a target by any means. Although we can always choose and create an FMP of the largest FM width and step as an optimal one, we should carefully

---

*http://www.nro.nao.ac.jp/~nro45mrt/html/obs/otf/param-e.html

†we can use them without loss of generality because other parameters such as t_{tran}, t_{app} are also related to v_{scan}. See figure 8 of Sawada et al. (2008)
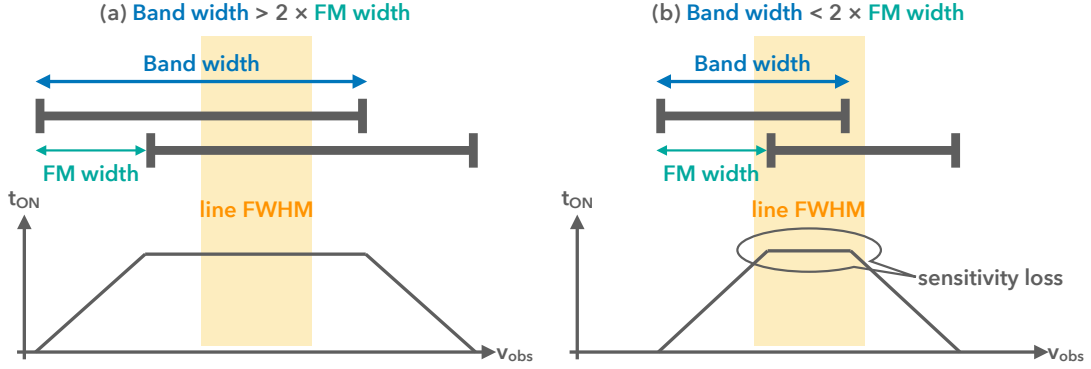
Figure 7.1: Schematic diagram of a requirement of spectrometer's band width for a spectral line observation. The top black bars show the band width of a spectrometer with frequency modulation. The bottom graphs show total ON-source time achieved with zig-zag FMP as a function of observed RF frequency. (a) the case of band width > 2 FM width: all the samples of a timestream fully cover the line width (FWHM) and sensitivity loss dosn't happen. (b) the case of band width < 2 FM width: some samples of a timestream dosn't cover the line witdh (FWHM) and sensitivity loss happens at the edges of the line.

consider the case that the signal of an emission line occupies large amount of a total band width of a spectrometer. For example of a spectral observation of a $\Delta v = 300$ km/s CO line (assuming a massive galaxy), this is equivalent to ~ 0.1 GHz at the Nobeyama 45 m for an observation of CO (1–0) and it is narrow enough (~ 6 %) for the total band width of spectrometer SAM45 (Kamazaki et al. (2012); 2000 MHz). On the other hand, that is equivalent to ~ 0.3 GHz at the ASTE 10 m for an observation of CO (3–2) and it occupies ~ 70 % of the total band width of spectrometer MAC ((Sorai et al., 2000); 512 MHz), which causes sensitivity loss at the outer skirts of line (see figure 7.1). If we would like to avoid causing such loss, the total band width of a spectrometer should be twice as wide as the FM width. Together with the guide for an optimal FMP (§ 5.3.4), the requirements for a spectrometer and FMP to carry out an FMLO spectral line observation is as follows:

$$\frac{1}{2} \, \text{band width} > \text{FM width} > \text{line width} \tag{7.1}$$

We note that this is not the case with a spectral line survey which obtains several GHz over the band width of a spectrometer. In this case, we can set an FM width

120

	OTF[†]	FMLO
l_1 (arcsec)	1200	3600
l_2 (arcsec)	1200	3600
Δl (arcsec)	6	6
t_{scan} (second)	24	72
t_{tran} (second)	5	5
t_{OFF} (second)	24	**0**
$t_{\mathrm{tran}}^{\mathrm{OFF}}$ (second)	10	**0**
t_{app} (second)	5	5
$N_{\mathrm{scan}}^{\mathrm{SEQ}}$	3	**0**
f_{cal}	$\simeq 1$	$\simeq 1$
d (arcsec)	10	10
η	4.3	4.3
t_{OH} (second)	15.0	**10.0**
$t_{\mathrm{cell}}^{\mathrm{ON}}$ (second)	**1.44**	1.32
$t_{\mathrm{cell}}^{\mathrm{OFF}}$ (second)	40.0	**0**
$t_{\mathrm{tot}}^{\mathrm{ON}}$ (minutes)	**724**	664
$t_{\mathrm{tot}}^{\mathrm{OBS}}$ (minutes)	1417	**821**
$\eta_{\mathrm{OBS}}^{\mathrm{ON}}$	0.51	**0.81**

Table 7.1: Comparison of observation efficiency between an OTF and FMLO observations of 1×1 deg^2 mapping area. †: The parameters are for a 20×20 arcmin^2 OTF mapping and we aim to take 9 times of single mapping to make a 1 deg^2 map.

wider than half of band width, and it is expected to be an efficient survey compared to conducting PSW observations several times by changing center frequencies. We also note that from the condition it is unable to obtain continuum emission with an FMLO observation (corresponding line width $\to \infty$). With a multi-pixel heterodyne receiver, however, it may be possible to obtain continuum emission because astronomical signals are modulated not only in frequency but also spatial axis like (sub-)millimeter continuum camera.
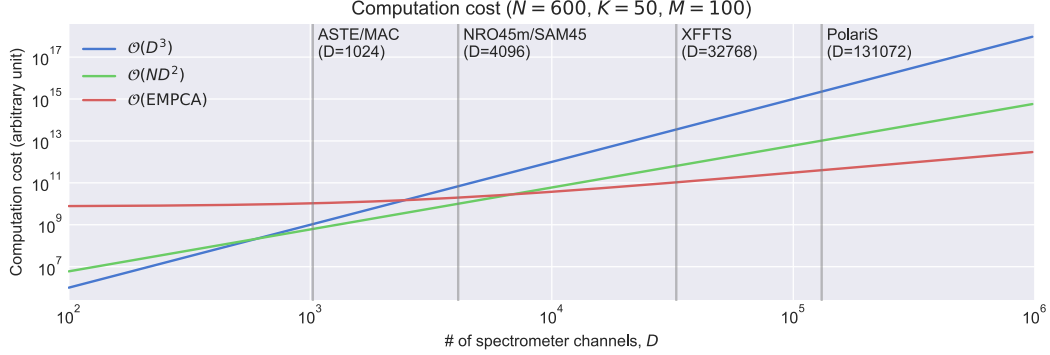
Figure 7.2: Comparison of computation costs between PCA and the EMPCA. The three lines show the number of operations as a function of the number of spectrometer channels, D. Unless D exceeds 10^4, the classical PCA and one calculating only first K principal components are better solutions. Otherwise the EMPCA is better by a order of magnitude or more. The other parameters are: the number of data, $N = 600$ (assuming time-chunk process of 1 minute), the number of principal components of interest, $K = 50$, the typical number of iterations looped in the EMPCA, $M = 100$.

7.2 COMPUTATION COST OF SIGNAL PROCESSING

As is discussed in Bailey (2012), one of the advantages to use the EMPCA is computation cost. The classical PCA requires a computation cost of $\mathcal{O}(D^3)$ ($\mathcal{O}$ is Landau symbol) for calculating a covariance matrix to derive eigenvectors, $\boldsymbol{P}$. If one would like to obtain only the first K eigenvectors, then the cost will be reduced to $\mathcal{O}(ND^2)$, but it still costs a lot when $N \ll D$, and it is the case with an FMLO observation where $N = 600$ (in time-chunk process) and $D \gtrsim 10^3$. On the other hand, the EMPCA requires only $\mathcal{O}(NK^3)$ to solve $\boldsymbol{C}$ in a E-step and $\mathcal{O}(NKD)$ to solve $\boldsymbol{P}$ in a M-step, respectively. Considering the number of iteration, M, it turns out that the EMPCA is more efficient if the following condition is fulfilled:

$$M(NK^3 + NKD) < ND^2 \tag{7.2}$$

In the case of signal processing of the thesis, these parameters are roughly: $M = 100$, $N = 600$, $K = 50$, and $D = 2000$. This yields $M(NK^3 + NKD)/(ND^2) \sim 6$, which indicates that the EMPCA is less efficient than the classical PCA. We note that the actual computation time is still reasonable: For example, the pipeline reduction takes total reduction time of 25 minutes including 16 EMPCA and 8

PCA iterative processes over an FMLO mapping observation of 39 minutes toward Orion region (Using Mac Pro Late 2013 with 3.5 GHz 6 Core Intel Xeon E5; see also § 6.2).

We also note that this result is finally reversed if D is more than 10^4 as illustrated in figure 7.2. In particular, some of digital spectrometers for (sub-)millimeter wavelength have already equipped with such number of spectroscopic channels (for example, XFFTS (Klein et al., 2012); PolariS (Mizuno et al., 2014)), and an FMLO system using XFFTS spectrometer is going to be used as a back-end of 2 mm receiver installed to the Large Millimeter Telescope (LMT; see also § 7.3.4). It is therefore valuable to use the EMPCA not only for estimating atmopheric line emission but also for reducing computation cost in the future spectroscopic instruments.

7.3 Future prospects of signal processing

7.3.1 Gain correction

As described in § 4.2, we plan to estimate FM gain from a frequency modulation load‡ measurement. Because there exists no signal from atmospheric and astronomical line emission, this will be better and secure estimation than that using a timestream of ON-point itself. In particular, this would be essential when we conduct an FMLO observation with a double sideband (DSB) mixer because equivalent contribution from LSB and USB of a DSB mixer will change the baseline of timestream more drastically than that of single sideband (SSB). Also it would be essential if we conduct an FMLO observation with a multi-pixel heterodyne receiver such as FOREST (Minamidani et al., 2016) because a gain curve is possible to be different between each receiver pixel, and it is thus necessary to correct FM gain before we conduct a map making. Although an measurement of a load with frequecy modulation requires a different observation table (a script which controls the telescope system), we have already tried such measurements and partially obtained the timestream (unable to use for the signal processing

---

‡an absorber of (sub-)millimeter wave signal at room temperature (see chapter 2)
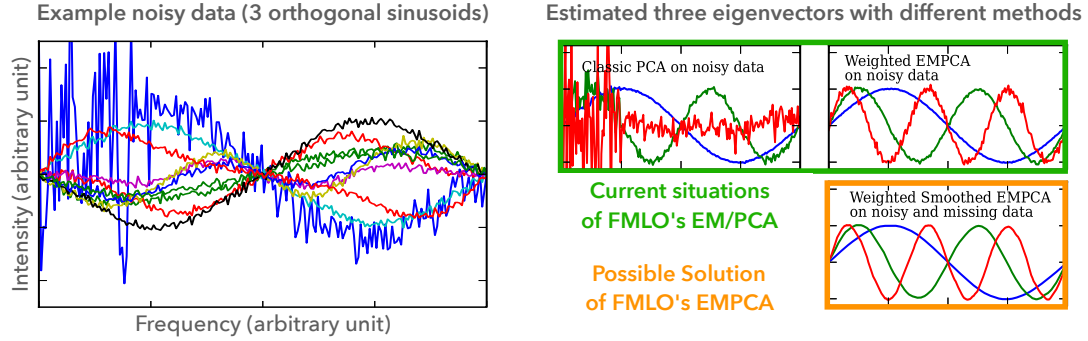
123

Figure 7.3: Demonstration of the EMPCA taken from Bailey (2012): (left) Example of noisy data created by three different period (orthogonal) of sinusoids plus noises (right) three eigenvectors constructed by different PCA-like methods. The top two panels show the result by classical PCA and weighted EMPCA on noisy data, which are the cases of current methods used in the pipeline algorithm, and the reconstructed eigenvectors contain noises. On the other hand, if we smooth eigenvectors during iterative steps of the EMPCA, one would obtain noiseless eigenvectors as shown in the bottom right panel.

above, though) in Nobeyama 45 m, which demonstrates the possibility of such measurements.

7.3.2 CORRELATED COMPONENT REMOVAL

In chapter 5 and 6, we demonstrate that PCA and the EMPCA properly estimate correlated components and thus cleaned timestream after such components are subtracted. There exists, however, an important issue about the contribution of noise from correlated components themselves, which is expressed as a factor, $\alpha \simeq 1.1$. Although it is smaller than the factor of position switching ($\alpha = \sqrt{2}$), it would be better if we could minimize such contribution (i.e., $\alpha_{\text{FMLO}} \to 1$). One possibility is smoothing of correlated components in each iteration of the EM-PCA. Bailey (2012) discuss the possibility of "smoothed EMPCA", where they demonstrate that smoothing of the eiven vectors at each M-step will result in optimal smooth eigenvectors rather than by smoothing noisy eigenvectors afterward like figure 7.3. This, however, requires a condition that the length scale of the intrinsic correlated components is larger than that of the noises, i.e., correlated component has not random but regular spectral shape during an observation and

we must know window length used for smoothing such as Savitzky-Golay filter. For such approach, we should obtain timestream of different frequency ranges and/or observation time or seasons to monitor the robustness of modes of correlated components. Also we should know an optimal window length for smoothing using the strategy of smoothed bandpass calibration (Yamaki et al., 2012).

7.3.3 Modeling atmospheric line emission

In chapter 6, we demonstrate that the strong line emission of ozone is detected and removed properly in both spectral and mapping FMLO observations. This approach, however, requires that spectral line of *all* molecular species detectable at the noise level. If we conduct much deeper FMLO observations ($\Delta T_A^* \sim \mathrm{mK}$) of a blind redshift search for a distant galaxy[§], it is necessary to distinguish a line of the target from ones from the atmosphere, for example, minor species such as CO, CO_2, NO_x, and rare transitions of major species (at least one mK-order line of ozone exists in 1 GHz band width). Therefore we may need to construct new models for such minor species at an observation site by collaboration with researchers of Earth atmosphere.

7.3.4 Application for other instruments

We mention ongoing and future possible application of the FMLO method and correlated component removal to the new instruments.

First of all, we will implement the FMLO method on the FOREST in early 2018 and carry out an on-site commissioning because the TZ receiver equipped with an FMLO is now decommissioned and FOREST is used as an alternative receiver at the observed frequency of 80–116 GHz. In the comissioning, we aim to demonstrate that all the results in the thesis are reproduced with FOREST, and also demonstrate the FM gain correction by a measurement of a jload with frequency modulation as well as multi-pixel FMLO method. We expect that

---

[§]an observation of a bright spectral line such as CO or ionized carbon to determine the spectroscopic redshift of a target which is roughly pre-estimated by another observations as a photometric redshift
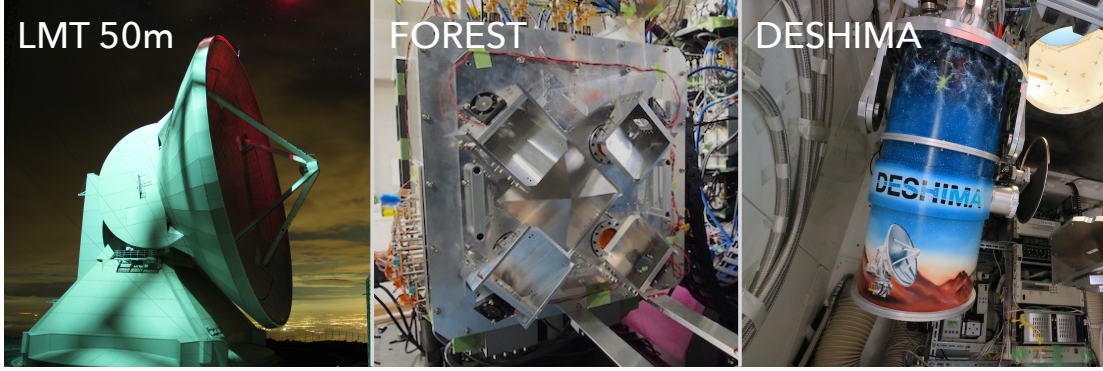
Figure 7.4: (left) Large Millimeter Telescope (LMT; © Large Millimeter Telescope Alfonso Serrano), (center) FOur-beam REceiver System on the 45-m Telescope (FOREST; © NAOJ), (right) Deep Spectroscopic High-redshift Mapper (DESHIMA; ©Endo Lab)

simultaneous timestreams by four beams will add spatial information for modeling astronomical line emission in a mapping observation.

As briefly mentioned above, we also plan to implement the FMLO method on the Band 4 receiver for the LMT 50 m, which has the largest aperture area among all single-dish telescopes at $\lambda \sim 2$ mm. We will use the XFFTS digital spectrometer as a backend, which would be a good demonstration of the iterative nature of the EMPCA. Moreover, the XFFTS has an advantage that its reference output signal synchronized with the start time of sampling can directly trigger the frequency modulation (list sweep) of the 1st LO signal generator (Agilent E8257D), which will achieve the time synchronization between frequency modulation and spectrometer's sampling without measuring spectral line observations such as SiO masers (see also § 5.2.2).

As a new application of correlated component removal to instruments other than heterodyne receivers, we are now verifying correlated noise removal on the data of DESHIMA (Deep Spectroscopic High-redshift Mapper; Endo et al. (2012)), an on-chip filterbank spectrometer with microwave kinetic inductance detectors (MKIDs) which will cover an ultra-wide frequency range of 240–720 GHz. Because DESHIMA is not a heterodyne receiver, the approach of correlated noise removal with the FMLO method is not applicable. On the other hand, the output of DESHIMA is a timestream data containing successive ON and OFF-point by

Figure 7.5: Atacama Large Millimeter/submillimeter Array (NAOJ, ESO, NRAO).

turns with a sampling rate of ~ 160 Hz. This means that we can model correlated components from a timestream of OFF-point by PCA: Once we get eigenvectors from OFF-point (expected to be no spectral line emission in them), then we can conduct linear fit of eigenvectors to a timestream of ON-point to achieve in-situ estimation of OFF-point. This approach of "timestream-based position switching" is originally proposed for thermal background subtraction in an infrared camera (Hunziker et al., 2017). It will be a useful method in the future telescopes and/or instruments for spectroscopy where the FMLO method is not applicable but one would like to subtract correlated components to obtain a spectrum with an expected sensitivity (i.e., not suffered from baseline wiggles).

Finally we would like to start discussing the application of the FMLO method to the ALMA Total Power Array, which is composed of four 12 m antenna as a part of Atacama Compact Array (Iguchi et al., 2009), and is also suffered from the low observing efficiency because of its high sensitivity. The FMLO method would be helpful to improve the observing efficiency as well as reduce baseline wiggles of such situations. Alghough we must solve the issues above to implement the FMLO to such an "ultimate" (sub-)millimeter telescope, it would be great opportunities to verify the FMLO method further using FOREST of Nobeyama 45 m, ASTE 10 m, and Band 4 receiver of LMT 50 m.

If the implementation is hard to explain, it's a bad idea. If the implementation is easy to explain, it may be a good idea.

From the Zen of Python, by Tim Peters

8
Conclusions

In this thesis, we aim to achieve a new spectroscopy based on correlated noise removal for high observation efficiency and less baseline repples realized by in-situ estimation of OFF-point without observing it, and thus develop a new method of timestream-based observation with frequency modulation of a local oscillator (FMLO) to which correlated noise removal is applicable. Together with all results, our conclusions of this thesis are as follows:

CORRELATED NOISE REMOVAL IN (SUB-)MILLIMETER SPECTROSCOPY

We demonstrate for the first time that correlated noises exist in a timestream data of an FMLO observation, and they are in-situ estimated and then subtracted with correlated noise removal realized by PCA and the EMPCA. This achieves obtaining a spectrum with no OFF-point observaions and thus high observation efficiency of $\eta_{obs} = 0.92$ in an FMLO observation of a spectral line. Compared to conventional PSW method on a spectral line observation, we demonstrate that the achieved sensitivity of the FMLO method per unit total observation time is ~ 1.7 times better than that of PSW, in other words, the achieved efficiency per unit noise level is ~ 3 times better. Also compared to conventional OTF method on a

mapping observation, we demonstrate that the achieved sensitivity of the FMLO method per unit total observation time is ∼1.1 times better than that of PSW, in other words, the achieved efficiency per unit noise level is ∼ 1.2 times better. Although, we consider these values as lower limit: There exists noise contribution from correlated component removal itself as a factor of $\alpha \simeq 1.1$. Another reason is the observations to which these values are derived are relatively small-scale: with longer pointing or wider mapping observations, the achieved sensitivity and efficiency will be much better than PSW ones because the FMLO method is free from various overhead such as OFF-point observation and telescope slew time between ON and OFF, which increases more in a longer (thus intending deeper) observation where observer should switch ON and OFF more quickly for the better spectal baseline flattness.

Formulation and signal processing for modulated timestreams

We express the observation equations of the FMLO method as an extension of ones for conventional PSW method with chopper-wheel calibration to modulated timestreams. From point of view of signal processing, we point out that the gain of ON-point observation is possible to be variable depending on frequency modulation (FM gain) suggested as the observation equation of the FMLO method. We thus propose a signal processing to estimate and correct for the FM gain before an intensity calibration and demonstrate that such FM gain has much amount of contribution to spectral baseline change, and is estimated and corrected by our proposed signal processing of smoothing ON-point timestream data after sorting by FM channels. We also propose a new correlated component removal method under strong and broader spectral line emission of the atmosphere such as ozone molecule. We introduce weighted PCA realized by the EMPCA, whose iterative steps take account of deweighting of atmospheric line existing elements over a timestream. We demonstrate that atmospheric ozone lines at 110 GHz and correlated components can be modeled separately by the EMPCA and ozone lines are finally removed from a final spectrum.

We verify the consistency between a spectrum of PSW method and one observed from FMLO method and then reduced with the signal processing proposed above, by simulation of observation and reduction with an artificial spectral line model embedded to timestream of blank sky. We demonstrate that Gaussian and rectangular models with several line widths and intensities are reproduced by simulations with the best frequency modulation pattern (FMP). We simultaneously obtain the guide for an optimal FMPs that the total FM width of an FMP should be wider than the line FWHM width. We also demonstrate that the obtained spectra of several astronomical target with FMLO and PSW or OTF mapping are consistent with each other with using an optimal FMP selected according to that guide.

From all the results, we finally demonstrate (sub-)millimeter spectroscopy based on correlated noise removal by a development of the FMLO method.

A

Supplementary Figures

Here we list supplementary figures related to § 5.3.4 (Optimization of freuquency modulation pattern). A mini summary of figures is as follows:

Figure A.1–A.6: Grid view of all the results of spectral line simulations with a Gaussian model ($\Delta v = [50, 100, 300]$ km/s, $T_{\mathrm{peak}} = [0.1, 0.5]$ K at 98.0 GHz) embedded to timestreams of blank sky observed with various FMPs.

Figure A.7–A.12: Grid view of all the results of spectral line simulations with a rectangular model ($\Delta v = [50, 100, 300]$ km/s, $T_{\mathrm{peak}} = [0.1, 0.5]$ K at 98.0 GHz) embedded to timestreams of blank sky observed with various FMPs.

Figure A.13–A.14: Heatmaps of reduced χ^2 between reproduced and model spectra of rectangular models ($\Delta v = [50, 100, 300]$ km/s from left to right, $T_{\mathrm{peak}} = [0.1, 0.5]$ K at 98.0 GHz) calculated for various FMPs.

Figure A.15–A.16: Heatmaps of reduced χ^2 after subtracting correlated components *at the first iteration* between reproduced and model spectra of rectangular models ($\Delta v = [50, 100, 300]$ km/s from left to right, $T_{\mathrm{peak}} = [0.1, 0.5]$ K at 98.0 GHz) calculated for various FMPs.
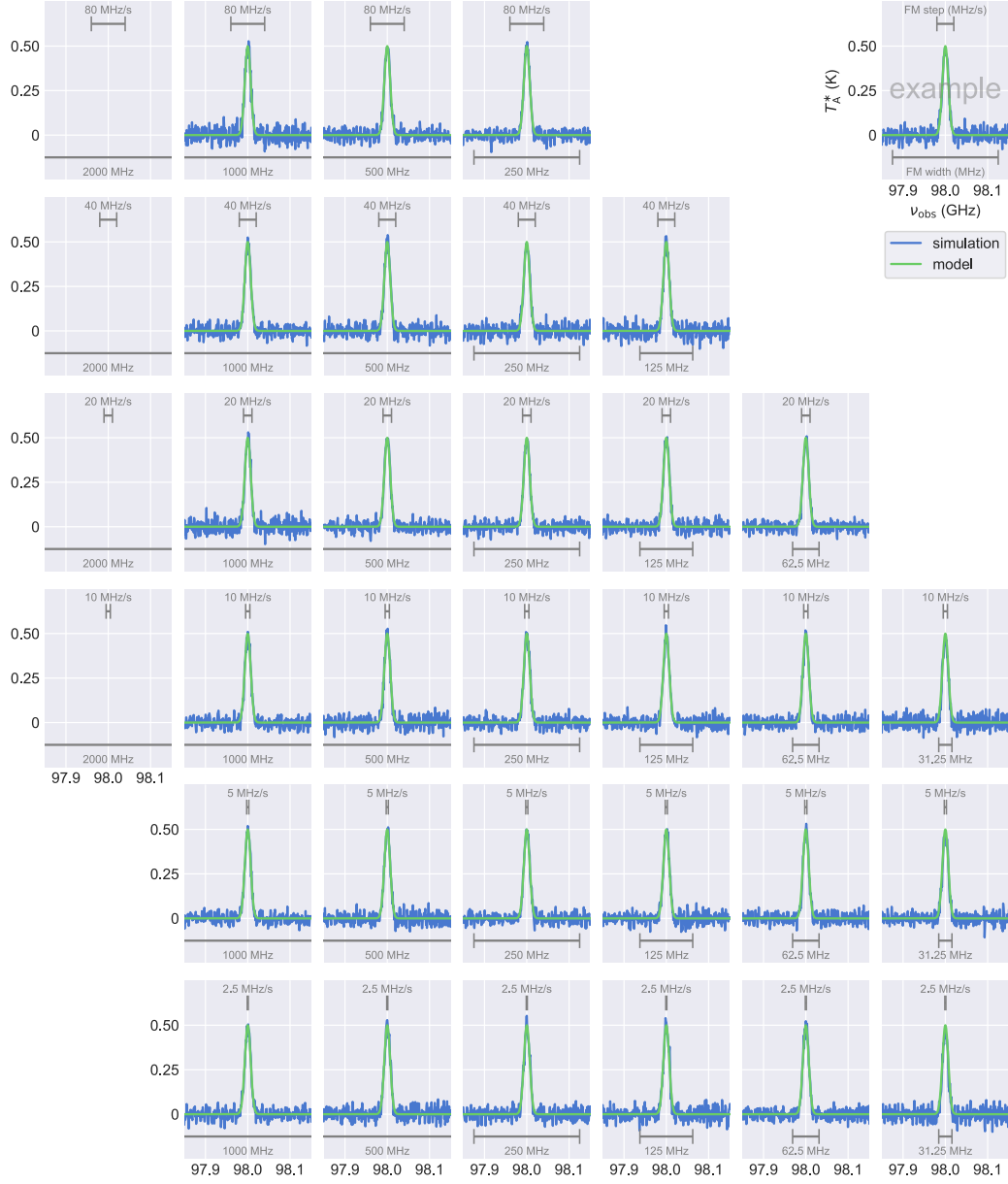
Figure A.1: Grid view of all the results of spectral line simulations with a Gaussian model ($\Delta v = 50$ km/s, $T_{\text{peak}} = 0.5$ K at 98.0 GHz) embedded to timestreams of blank sky observed with various FMPs. Blue and green lines show the reproduced spectrum after signal processing and the model spectrum itself, respectively. Gray bars at top and bottom of a panel indicate an FM step (MHz/sample; printed as MHz/s) and FM width (MHz) of an FMP used for an FMLO observation.

Figure A.2: Grid view of all the results of spectral line simulations with a Gaussian model ($\Delta v = 100$ km/s, $T_{\mathrm{peak}} = 0.5$ K at 98.0 GHz) embedded to timestreams of blank sky observed with various FMPs. Blue and green lines show the reproduced spectrum after signal processing and the model spectrum itself, respectively. Gray bars at top and bottom of a panel indicate an FM step (MHz/sample; printed as MHz/s) and FM width (MHz) of an FMP used for an FMLO observation.
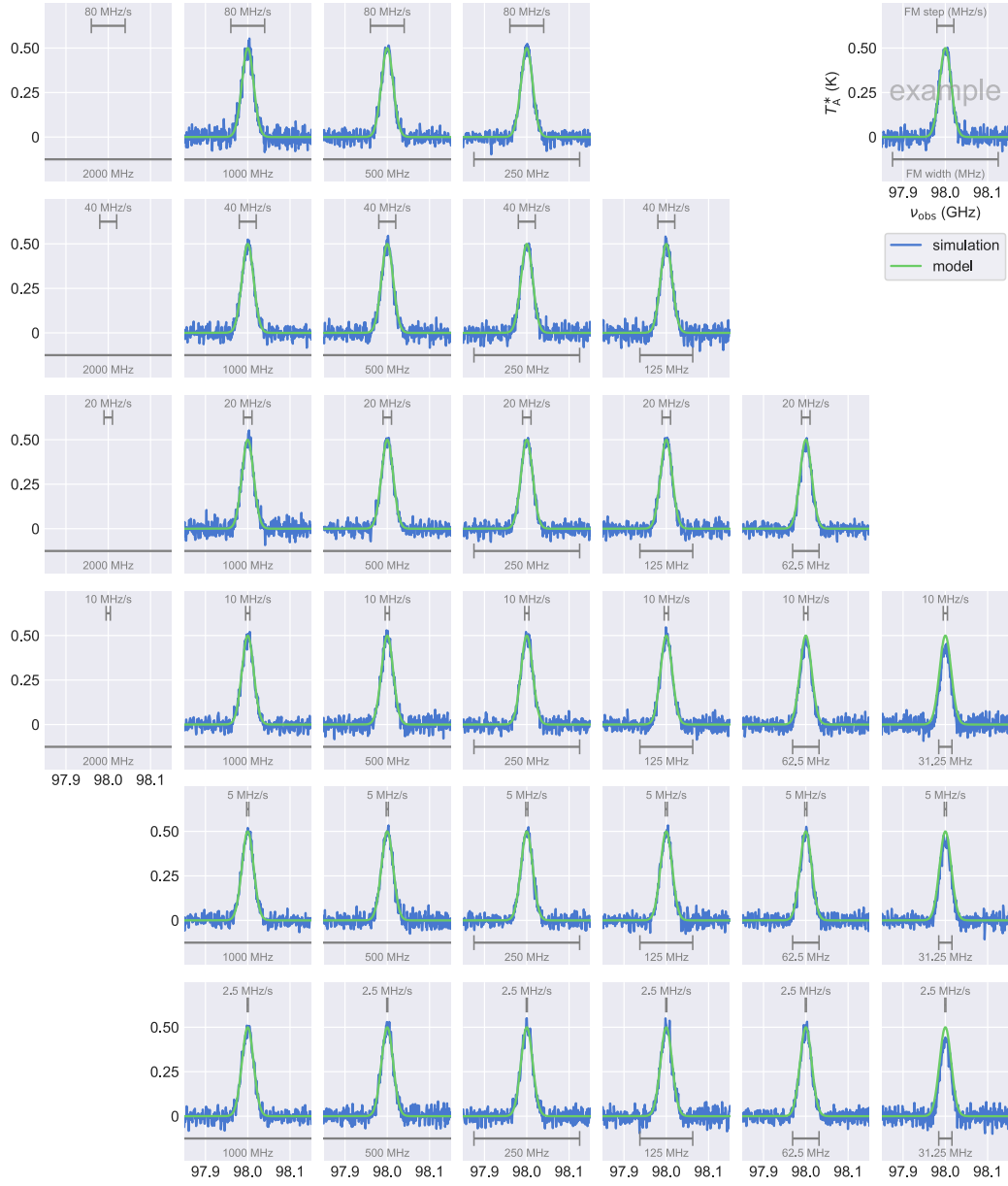
Figure A.3: Grid view of all the results of spectral line simulations with a Gaussian model ($\Delta v = 300$ km/s, $T_{\mathrm{peak}} = 0.5$ K at 98.0 GHz) embedded to timestreams of blank sky observed with various FMPs. Blue and green lines show the reproduced spectrum after signal processing and the model spectrum itself, respectively. Gray bars at top and bottom of a panel indicate an FM step (MHz/sample; printed as MHz/s) and FM width (MHz) of an FMP used for an FMLO observation.
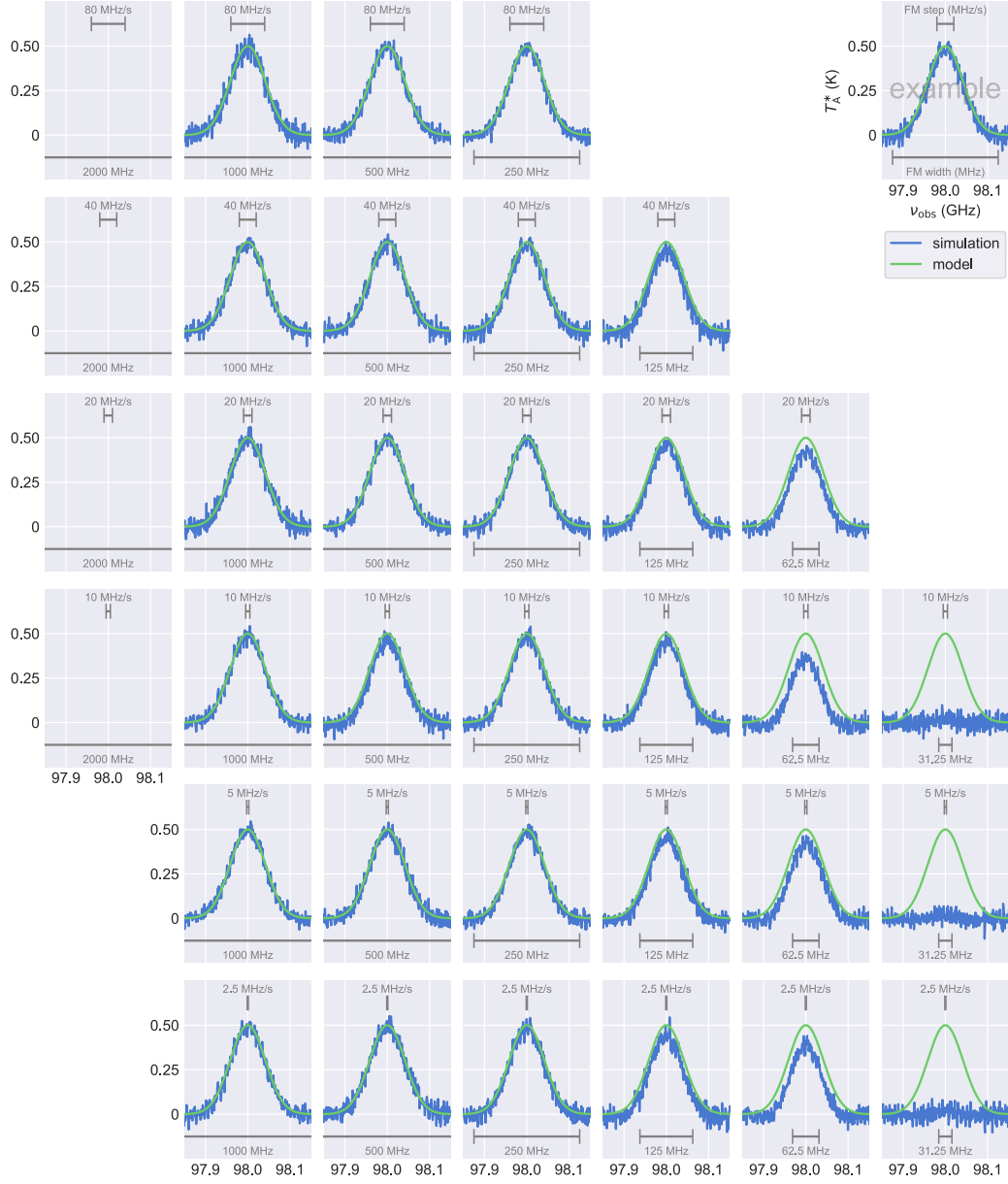
134

Figure A.4: Grid view of all the results of spectral line simulations with a Gaussian model ($\Delta v = 50$ km/s, $T_{\mathrm{peak}} = 0.1$ K at 98.0 GHz) embedded to timestreams of blank sky observed with various FMPs. Blue and green lines show the reproduced spectrum after signal processing and the model spectrum itself, respectively. Gray bars at top and bottom of a panel indicate an FM step (MHz/sample; printed as MHz/s) and FM width (MHz) of an FMP used for an FMLO observation.

Figure A.5: Grid view of all the results of spectral line simulations with a Gaussian model ($\Delta v = 100$ km/s, $T_{\mathrm{peak}} = 0.1$ K at 98.0 GHz) embedded to timestreams of blank sky observed with various FMPs. Blue and green lines show the reproduced spectrum after signal processing and the model spectrum itself, respectively. Gray bars at top and bottom of a panel indicate an FM step (MHz/sample; printed as MHz/s) and FM width (MHz) of an FMP used for an FMLO observation.

136

Figure A.6: Grid view of all the results of spectral line simulations with a Gaussian model ($\Delta v = 300$ km/s, $T_{\mathrm{peak}} = 0.1$ K at 98.0 GHz) embedded to timestreams of blank sky observed with various FMPs. Blue and green lines show the reproduced spectrum after signal processing and the model spectrum itself, respectively. Gray bars at top and bottom of a panel indicate an FM step (MHz/sample; printed as MHz/s) and FM width (MHz) of an FMP used for an FMLO observation.
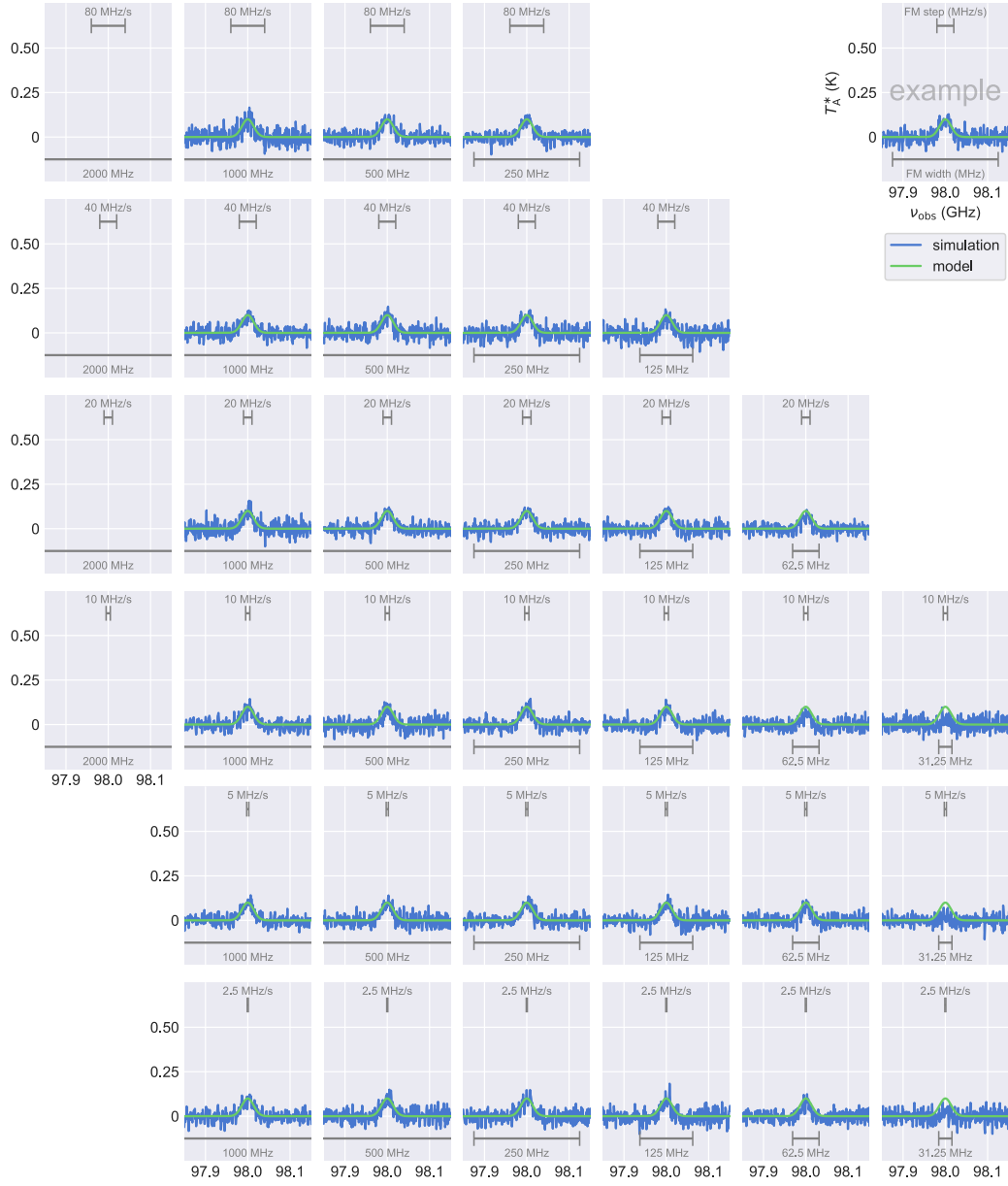
137

Figure A.7: Grid view of all the results of spectral line simulations with a rectangular model ($\Delta v = 50$ km/s, $T_{\mathrm{peak}} = 0.5$ K at 98.0 GHz) embedded to timestreams of blank sky observed with various FMPs. Blue and green lines show the reproduced spectrum after signal processing and the model spectrum itself, respectively. Gray bars at top and bottom of a panel indicate an FM step (MHz/sample; printed as MHz/s) and FM width (MHz) of an FMP used for an FMLO observation.
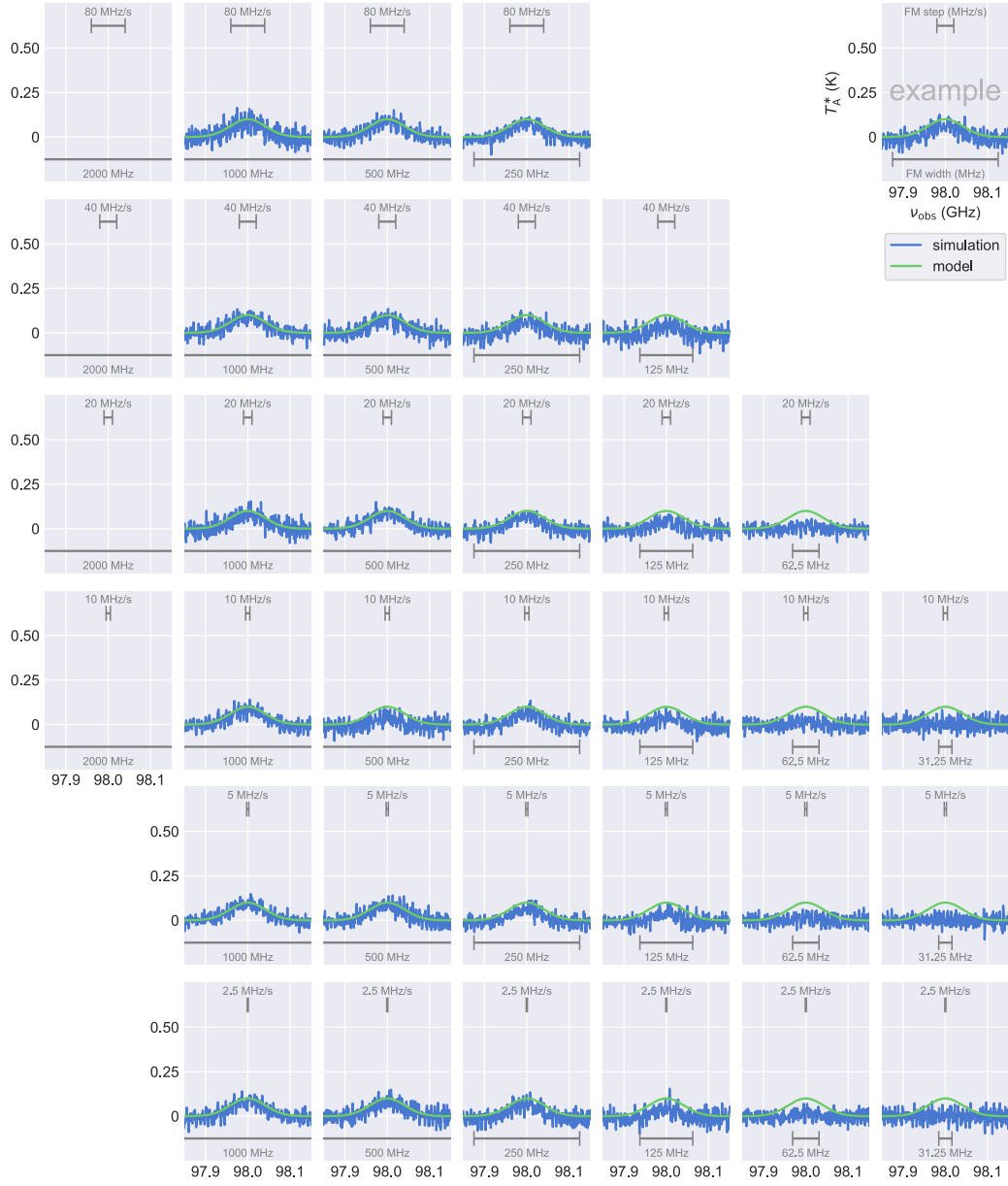
138

Figure A.8: Grid view of all the results of spectral line simulations with a rectangular model ($\Delta v = 100$ km/s, $T_{\mathrm{peak}} = 0.5$ K at 98.0 GHz) embedded to timestreams of blank sky observed with various FMPs. Blue and green lines show the reproduced spectrum after signal processing and the model spectrum itself, respectively. Gray bars at top and bottom of a panel indicate an FM step (MHz/sample; printed as MHz/s) and FM width (MHz) of an FMP used for an FMLO observation.
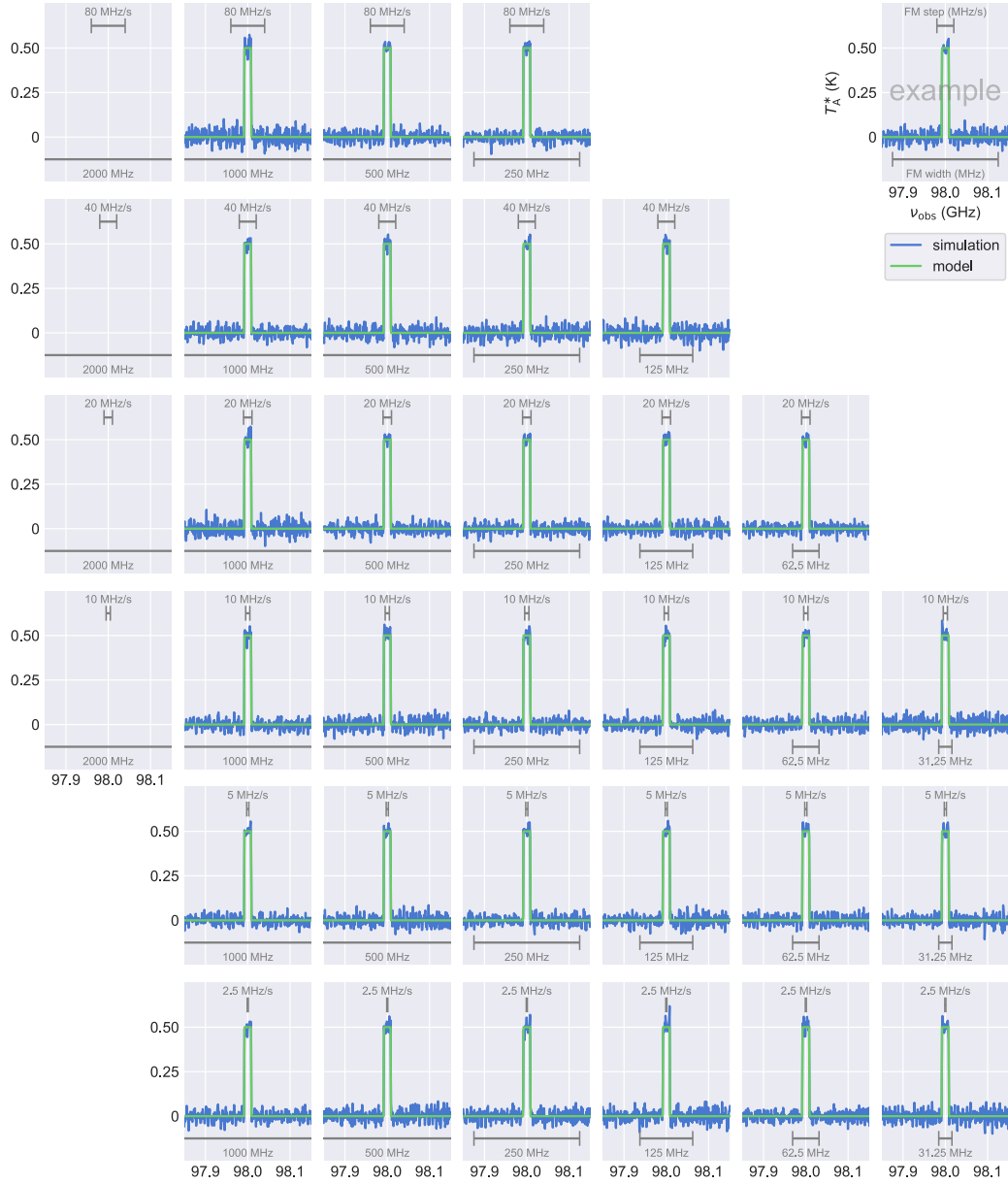
Figure A.9: Grid view of all the results of spectral line simulations with a rectangular model ($\Delta v = 300$ km/s, $T_{\mathrm{peak}} = 0.5$ K at 98.0 GHz) embedded to timestreams of blank sky observed with various FMPs. Blue and green lines show the reproduced spectrum after signal processing and the model spectrum itself, respectively. Gray bars at top and bottom of a panel indicate an FM step (MHz/sample; printed as MHz/s) and FM width (MHz) of an FMP used for an FMLO observation.
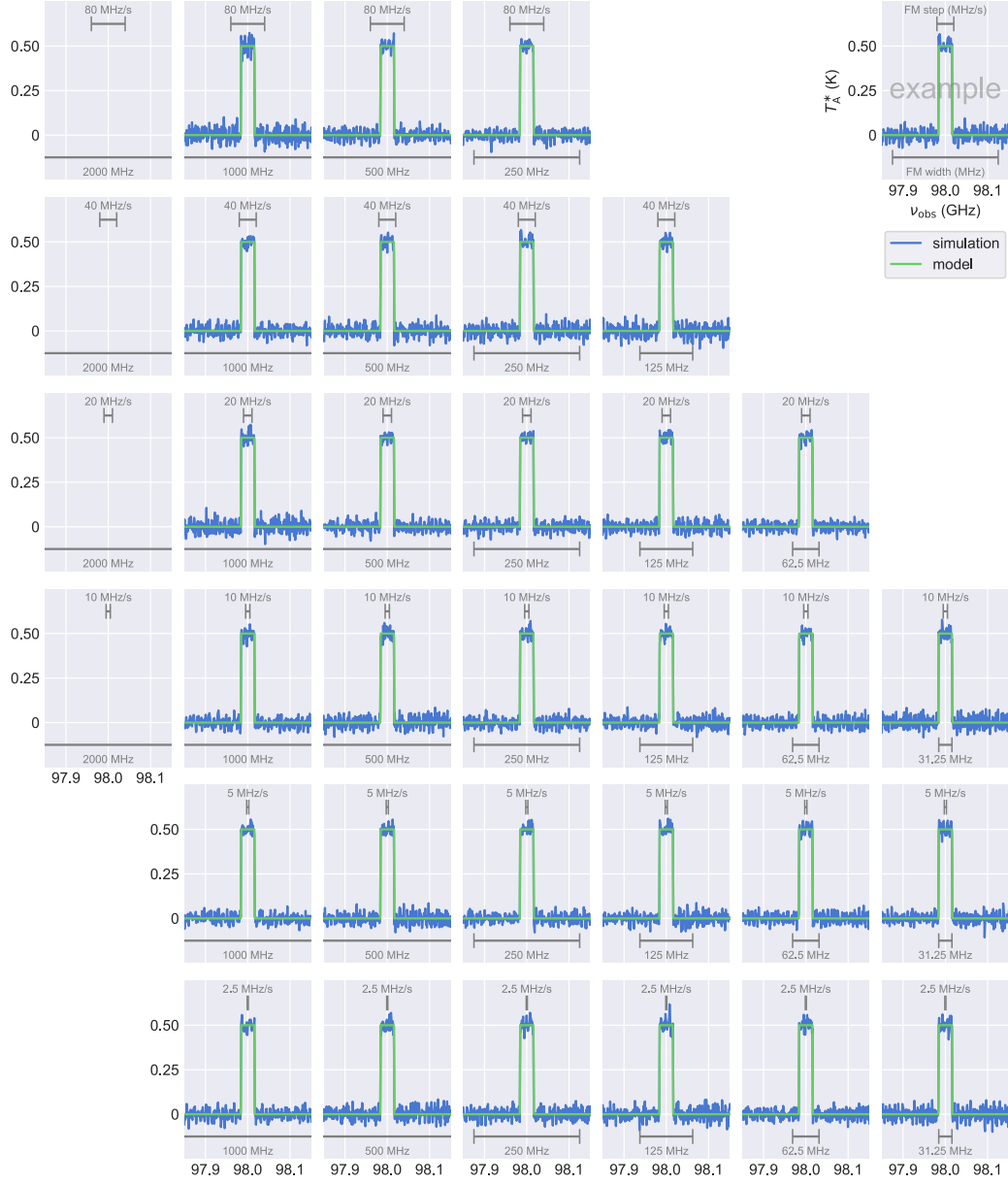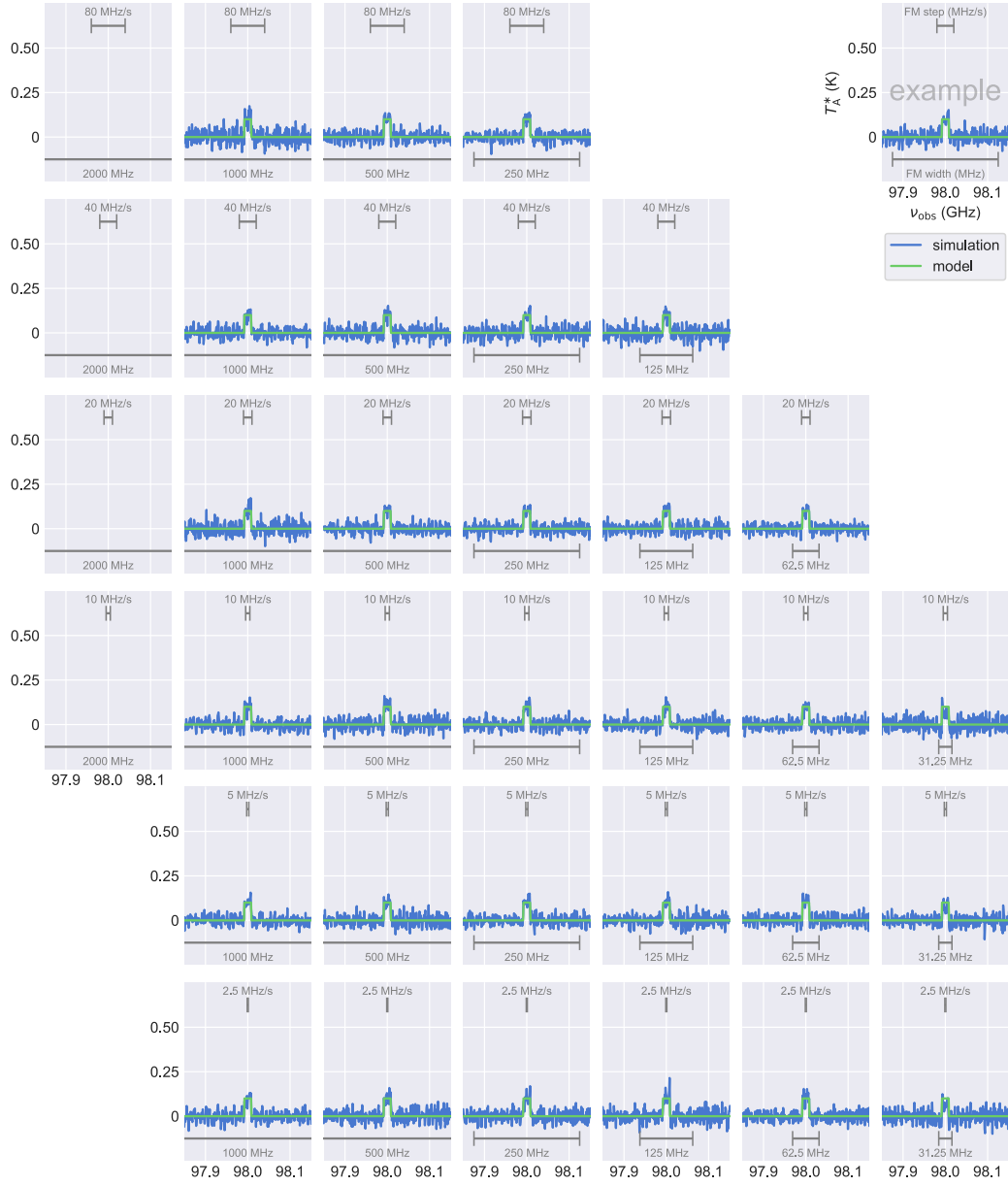
Figure A.10: Grid view of all the results of spectral line simulations with a rectangular model ($\Delta v = 50$ km/s, $T_{\mathrm{peak}} = 0.1$ K at 98.0 GHz) embedded to timestreams of blank sky observed with various FMPs. Blue and green lines show the reproduced spectrum after signal processing and the model spectrum itself, respectively. Gray bars at top and bottom of a panel indicate an FM step (MHz/sample; printed as MHz/s) and FM width (MHz) of an FMP used for an FMLO observation.
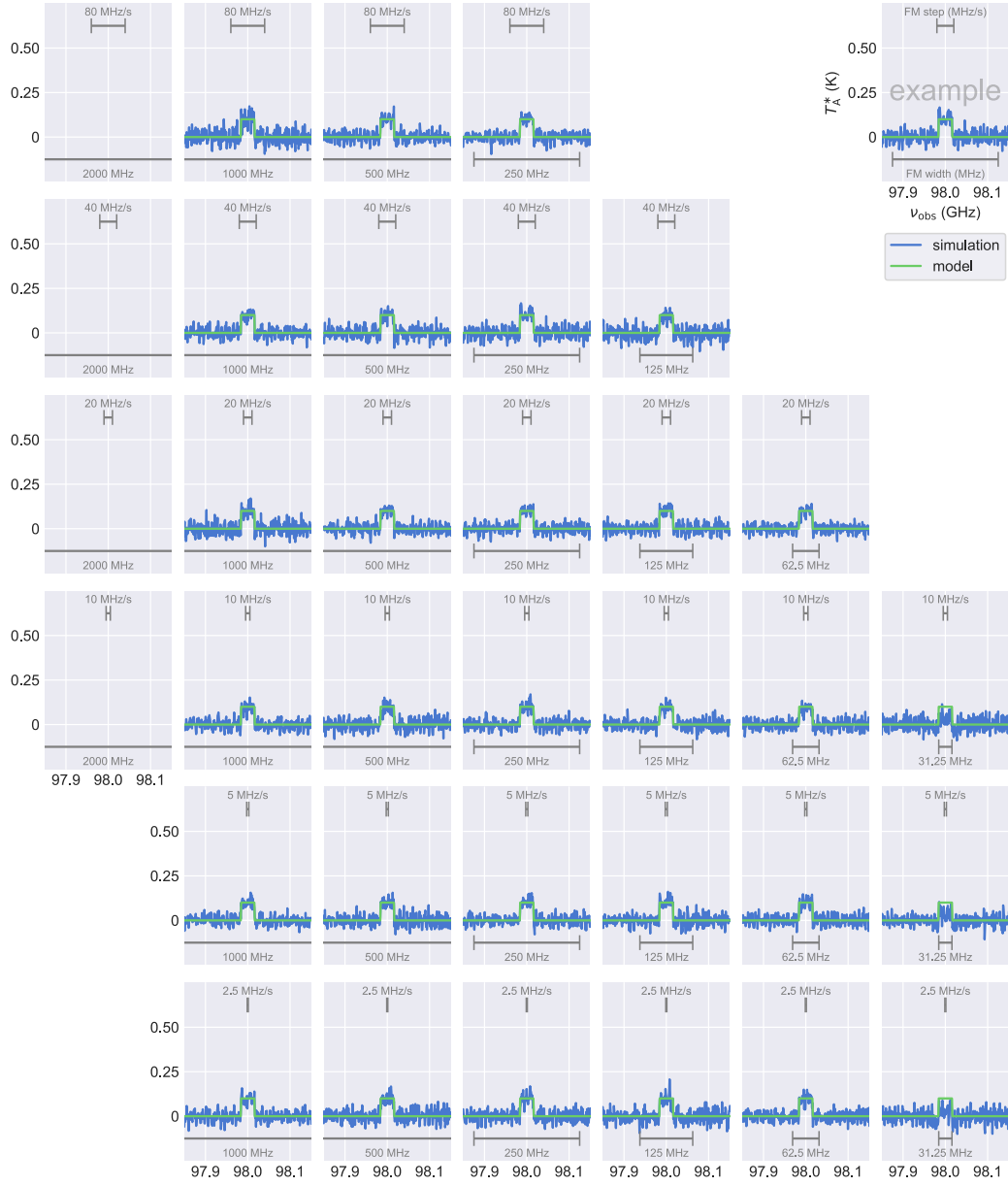
Figure A.11: Grid view of all the results of spectral line simulations with a rectangular model ($\Delta v = 100$ km/s, $T_{\text{peak}} = 0.1$ K at 98.0 GHz) embedded to timestreams of blank sky observed with various FMPs. Blue and green lines show the reproduced spectrum after signal processing and the model spectrum itself, respectively. Gray bars at top and bottom of a panel indicate an FM step (MHz/sample; printed as MHz/s) and FM width (MHz) of an FMP used for an FMLO observation.
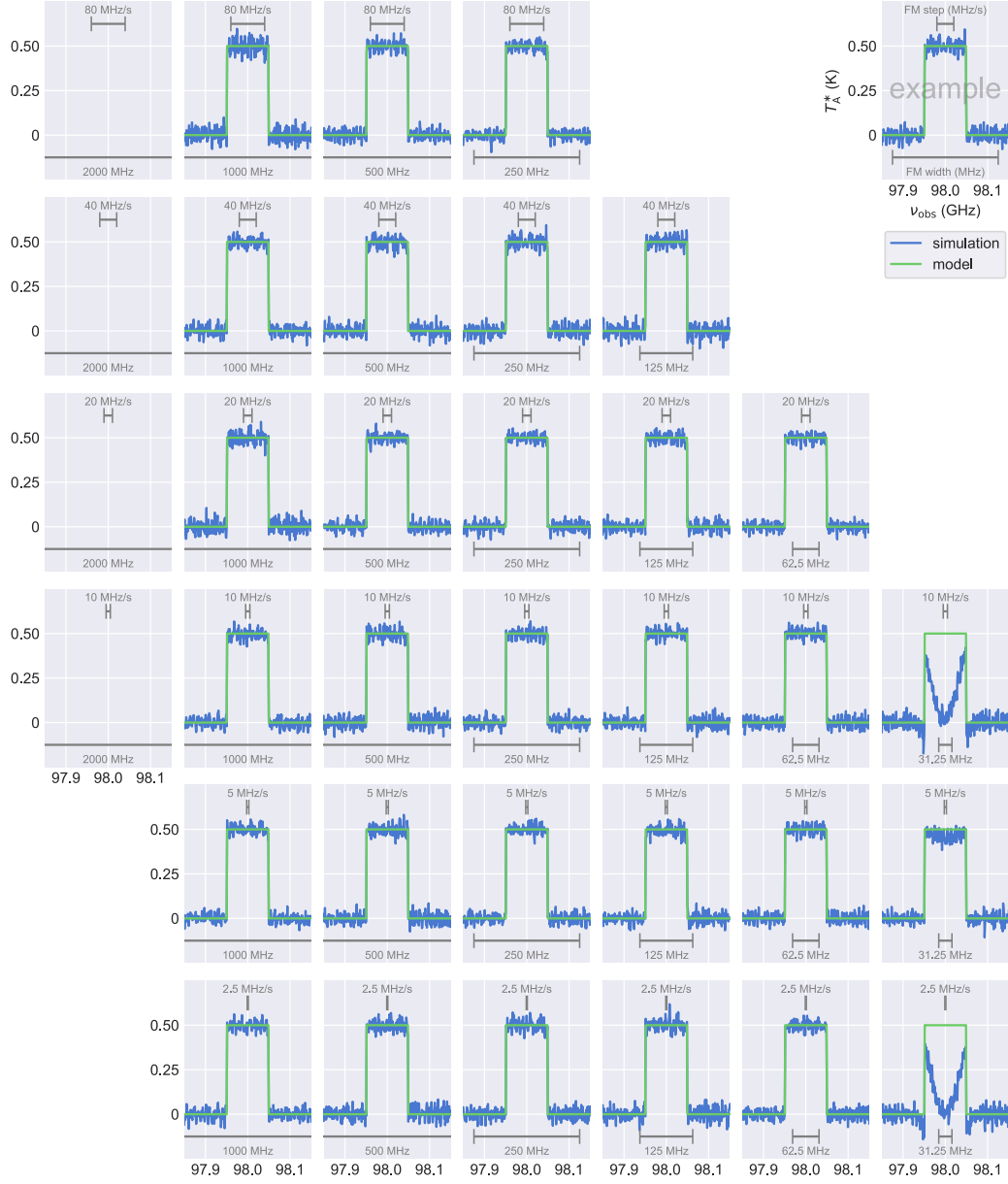
142
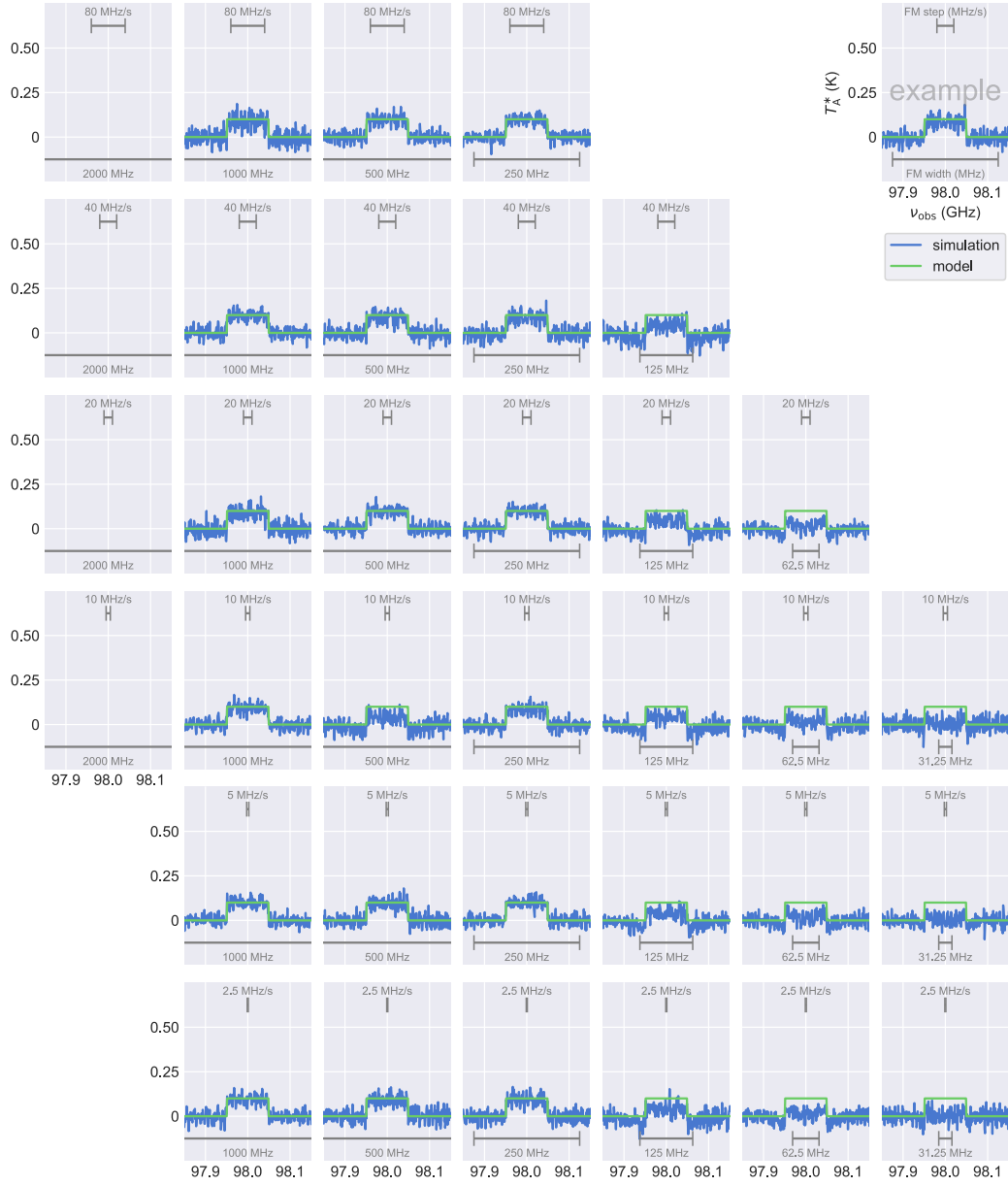
Figure A.12: Grid view of all the results of spectral line simulations with a rectangular model ($\Delta v = 300$ km/s, $T_{\mathrm{peak}} = 0.1$ K at 98.0 GHz) embedded to timestreams of blank sky observed with various FMPs. Blue and green lines show the reproduced spectrum after signal processing and the model spectrum itself, respectively. Gray bars at top and bottom of a panel indicate an FM step (MHz/sample; printed as MHz/s) and FM width (MHz) of an FMP used for an FMLO observation.

143
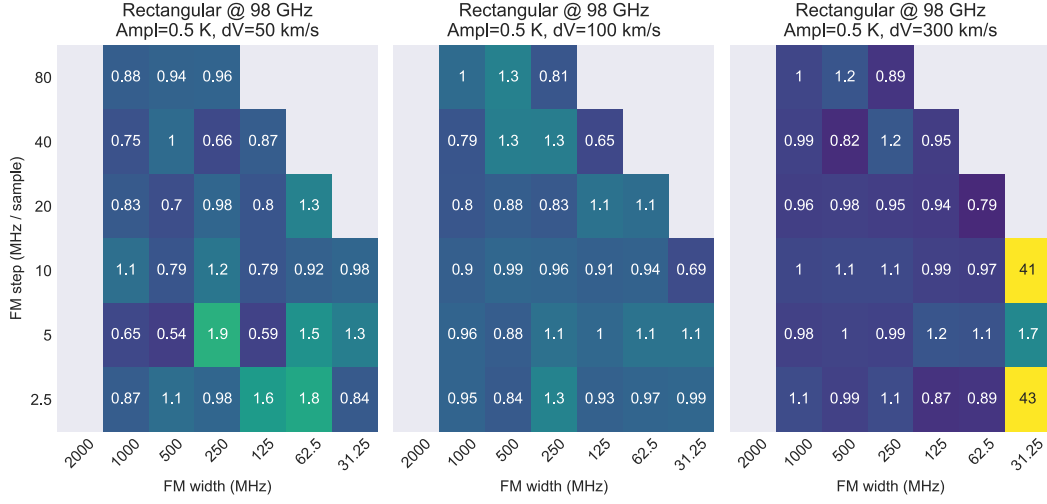
Figure A.13: Heatmaps of reduced χ^2 between reproduced and model spectra of rectangular models ($\Delta v = 50, 100, 300$ km/s from left to right, $T_{\mathrm{peak}} = 0.5$ K at 98.0 GHz) calculated for various FMPs. The numbers in each cell are the values of reduced χ^2 which are derived using $\pm 3\Delta v$ frequency range as line region and $\pm[3\Delta v, 6\Delta v]$ as line-free regions for calculating noise level.

Figure A.14: Heatmaps of reduced χ^2 between reproduced and model spectra of rectangular models ($\Delta v = 50, 100, 300$ km/s from left to right, $T_{\mathrm{peak}} = 0.1$ K at 98.0 GHz) calculated for various FMPs. The numbers in each cell are the values of reduced χ^2 which are derived using $\pm 3\Delta v$ frequency range as line region and $\pm[3\Delta v, 6\Delta v]$ as line-free regions for calculating noise level.

Figure A.15: Heatmaps of reduced χ^2 after subtracting correlated components *at the first iteration* between reproduced and model spectra of rectangular models ($\Delta v = 50, 100, 300$ km/s from left to right, $T_{\mathrm{peak}} = 0.5$ K at 98.0 GHz) calculated for various FMPs. The parameters used for calculating reduced χ^2 are same as figure A.13.

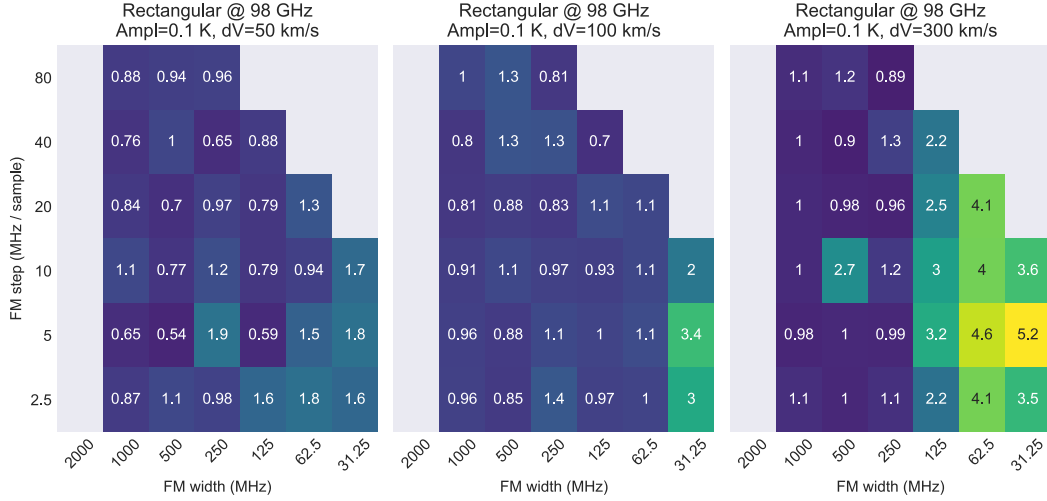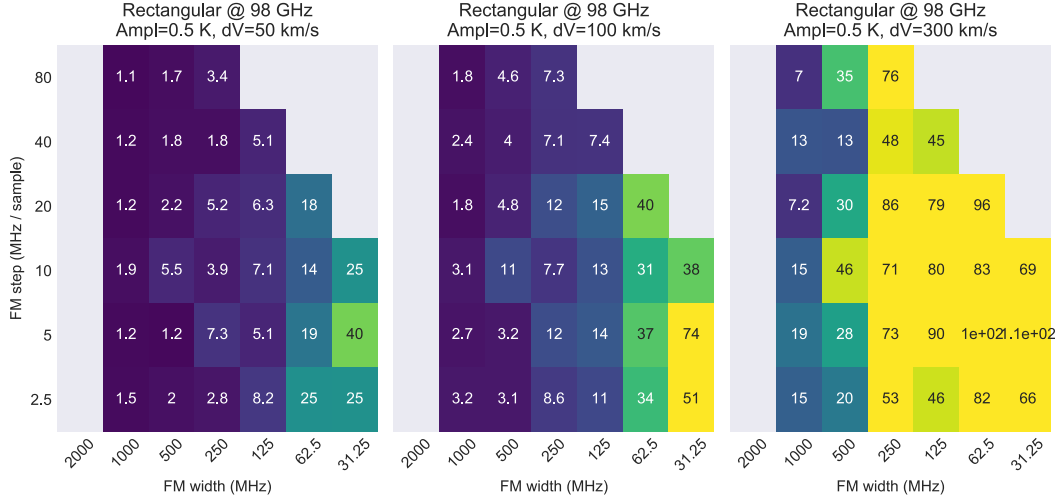**Figure A.16:** Heatmaps of reduced χ^2 after subtracting correlated components *at the first iteration* between reproduced and model spectra of rectangular models ($\Delta v = 50, 100, 300$ km/s from left to right, $T_{\mathrm{peak}} = 0.1$ K at 98.0 GHz) calculated for various FMPs. The parameters used for calculating reduced χ^2 are same as figure A.14.

145

B

Supplementary Equations

Here we describe the detailed deformation from equation 4.8 to 4.10. We note that the terms from image sideband are not described in the following equations for the simplicity without loss of generality. We start the deformation from the observation equations of ON and Load after gain correction:

$$\boldsymbol{P}^{\text{ON,corr}} = \boldsymbol{G}^0 k_{\text{B}} \left\{ \eta \left[\boldsymbol{T}^{\text{Ast}} \boldsymbol{e}^{-\boldsymbol{\tau}} + T^{\text{Atm}}(1 - \boldsymbol{e}^{-\boldsymbol{\tau}}) \right] + (\boldsymbol{1} - \eta)T^{\text{Room}} + T^{\text{RX}} \right\} \quad \text{(B.1)}$$

$$\boldsymbol{P}^{\text{Load,corr}} = \boldsymbol{G}^0 k_{\text{B}} \left\{ T^{\text{Room}} + T^{\text{RX}} \right\} \quad \text{(B.2)}$$

They are same as equation 4.6 and 4.7. The equivalent OFF-point timestream is calculated by median of $\boldsymbol{P}^{\text{ON,corr}}$ along time axis:

$$\boldsymbol{P}^{\text{OFF}} \equiv \text{med}_n(\boldsymbol{P}^{\text{ON,corr}})$$

$$= \boldsymbol{G}^0 k_{\text{B}} \left\{ \eta \left[\boldsymbol{T}^{\text{C}} \boldsymbol{e}^{-\text{med}_n(\boldsymbol{\tau})} + T^{\text{Atm}}(\boldsymbol{1} - \boldsymbol{e}^{-\text{med}_n(\boldsymbol{\tau})}) \right] + (1 - \eta)T^{\text{Room}} + T^{\text{RX}} \right\} \quad \text{(B.3)}$$

Then we describe the operations of ON–OFF and Load–OFF, which are enumerator and demominator of one-load chopper wheel calibration's equation:

$$\boldsymbol{P}^{\mathrm{ON,corr}} - \boldsymbol{P}^{\mathrm{OFF}}$$
$$= G^0 k_{\mathrm{B}} \eta \left\{ \boldsymbol{T}^{\mathrm{Ast}} e^{-\boldsymbol{\tau}} - \boldsymbol{T}^{\mathrm{C}} e^{-\mathrm{med}_n(\boldsymbol{\tau})} - T^{\mathrm{Atm}} (e^{-\boldsymbol{\tau}} - e^{-\mathrm{med}_n(\boldsymbol{\tau})}) \right\}$$
$$= G^0 k_{\mathrm{B}} \eta e^{-\mathrm{med}_n(\boldsymbol{\tau})} \left\{ \boldsymbol{T}^{\mathrm{Ast}} e^{-\bar{\boldsymbol{\tau}}} - \boldsymbol{T}^{\mathrm{C}} + T^{\mathrm{Atm}} (1 - e^{-\bar{\boldsymbol{\tau}}}) \right\} \tag{B.4}$$

$$\boldsymbol{P}^{\mathrm{Load,corr}} - \boldsymbol{P}^{\mathrm{OFF}}$$
$$= G^0 k_{\mathrm{B}} \eta e^{-\mathrm{med}_n(\boldsymbol{\tau})} \left\{ \boldsymbol{T}^{\mathrm{Atm}} - \boldsymbol{T}^{\mathrm{C}} \right\} \tag{B.5}$$

where $\bar{\boldsymbol{\tau}} \equiv \boldsymbol{\tau} - \mathrm{med}_n(\boldsymbol{\tau})$ is the median-subtracted opacity of the atmosphere. Finally we obtain $\boldsymbol{T}^{\mathrm{Calib}}$ by substituting them in the equation B.6:

$$\boldsymbol{T}^{\mathrm{Calib}} = T^{\mathrm{Atm}} \frac{\boldsymbol{P}^{\mathrm{ON,corr}} - \boldsymbol{P}^{\mathrm{OFF}}}{\boldsymbol{P}^{\mathrm{Load,corr}} - \boldsymbol{P}^{\mathrm{OFF}}} \tag{B.6}$$

$$= \frac{T^{\mathrm{Atm}}}{\boldsymbol{T}^{\mathrm{Atm}} - \boldsymbol{T}^{\mathrm{C}}} \left[\boldsymbol{T}^{\mathrm{Ast}} e^{-\bar{\boldsymbol{\tau}}} - \boldsymbol{T}^{\mathrm{C}} + T^{\mathrm{Atm}} (1 - e^{-\bar{\boldsymbol{\tau}}}) \right]$$

$$= \frac{T^{\mathrm{Atm}}}{\boldsymbol{T}^{\mathrm{Atm}} - \boldsymbol{T}^{\mathrm{C}}} \left[\boldsymbol{T}^{\mathrm{C}} e^{-\bar{\boldsymbol{\tau}}} + \boldsymbol{T}^{\mathrm{NC}} e^{-\bar{\boldsymbol{\tau}}} - \boldsymbol{T}^{\mathrm{C}} + T^{\mathrm{Atm}} (1 - e^{-\bar{\boldsymbol{\tau}}}) \right]$$

$$= \frac{T^{\mathrm{Atm}}}{\boldsymbol{T}^{\mathrm{Atm}} - \boldsymbol{T}^{\mathrm{C}}} \left[\boldsymbol{T}^{\mathrm{NC}} e^{-\bar{\boldsymbol{\tau}}} + (\boldsymbol{T}^{\mathrm{Atm}} - \boldsymbol{T}^{\mathrm{C}})(1 - e^{-\bar{\boldsymbol{\tau}}}) \right]$$

$$= \frac{\boldsymbol{T}^{\mathrm{NC}}}{1 - \boldsymbol{\varepsilon}} e^{-\bar{\boldsymbol{\tau}}} + T^{\mathrm{Atm}} (1 - e^{-\bar{\boldsymbol{\tau}}}) \tag{B.7}$$

where $\boldsymbol{\varepsilon} \equiv \boldsymbol{T}^{\mathrm{C}}/T^{\mathrm{Atm}}$ is the intensity ratio between astronomical continuum and atmosphere (~ 293 K). Under an assumption of $\boldsymbol{\varepsilon} \ll 1$ (and this is applicable for the most case of an astronomical observations), equation B.7 can be simply expressed as the following:

$$\boldsymbol{T}^{\mathrm{Calib}} \simeq \boldsymbol{T}^{\mathrm{NC}} e^{-\bar{\boldsymbol{\tau}}} + T^{\mathrm{Atm}} (1 - e^{-\bar{\boldsymbol{\tau}}}) \tag{B.8}$$

This is what we use as equation 4.10 (without explicitly expressing image sideband).

Namespaces are one honking great idea
– let's do more of those!

From the Zen of Python, by Tim Peters

C

FMFlow – Data Analysis Package

Here we briefly introduce `FMFlow`, a Python data analysis package for the FMLO method, which are developed and mainteined by the FMLO software team[*]. We also show a Python script using `FMFlow` used for reducing data of the science demonstration of Nobeyama 45 m.

C.1 Current status of FMFlow

Currently `FMFlow` has been developed for providing three different functionalities: (1) merging a raw timestream (binary data), several log files of an FMLO observation into a single FITS file according to a telescope/instrument-independent specifications called FMFITS[†], (2) loading a FMFITS file in Python and create an object of timestream as xarray[‡] format, and (3) providing various functions which operate an xarray of timestream such as de/modulation, integration/projection, EM/PCA, and various modeling methods described in chapter 4. We don't describe usages of each function here because we provide an online documentation

---

[*] https://github.com/fmlo-dev/fmflow
[†] https://github.com/fmlo-dev/fmflow/wiki/FMFITS
[‡] http://xarray.pydata.org

available at https://fmlo-dev.github.io/fmflow, and also because `FMFlow` is beta version at Dec 2017: We will release stable versions as soon as possible after the results of FMLO method is published.

C.2 How to obtain and use

The easiest way to install `FMFlow` is to use `pip`:

```
$ pip install fmflow
```

We require the Python version of 3.5 or higher, and installation of several essential packages of `NumPy`, `SciPy`, `AstroPy`, `PyYAML`, and `xarray`. The recommended way to prepare such Python environment is to install Python by an latest Anaconda distribution[§]. The all source code can be directly downloaded from the GitHub repository[¶]

C.3 Typical Python script for reduction

Here we show a Python script using `FMFlow` used for reducing data of the science demonstration of Nobeyama 45 m.

```python
1  import fmflow as fm
2  import numpy as np
3  import matplotlib.pyplot as plt
4
5  # module constants
6  Tamb = 293.0 # K
7  timechunk = 600 # ch
8
9  # function of calculating weight for EMPCA
10 def empca_weight(Tmodel, Tresidual, snr_halfweight=10):
```

[§]https://www.anaconda.com
[¶]https://github.com/fmlo-dev/fmflow/fmflow

```
11      noise = fm.tospectrum(Tresidual).noise
12      Tnoise = fm.fromspectrum(noise, Tresidual)
13      snr_abs = np.abs(Tmodel / Tnoise)
14      return 2.0**-(snr_abs / snr_halfweight)
15
16  # objects for check convergence
17  cv_gain = fm.utils.Convergence(1e-2)
18  cv_atm  = fm.utils.Convergence(1e-2)
19  cv_ast  = fm.utils.Convergence(1e-2)
20
21  # load timestreams of ON and R (load)
22  fitsname = 'fmlodata.fits'
23  arrayid  = 'A5' # USB, SAM45
24  Pon0 = fm.fits.getarray(fitsname, arrayid, 'ON')
25  Pr   = fm.fits.getarray(fitsname, arrayid, 'R')
26
27  # pipeline starts
28  Gfm = fm.ones_like(Pon0)
29  while not cv_gain(Gfm):
30      # intensity calibration
31      Pon  = Pon0 / Gfm
32      Poff = Pon.median('t')
33      Tcal = Tamb * (Pon-Poff) / (Pr-Poff)
34
35      # modeling atmospheric lines
36      Tatm = fm.zeros_like(Tcal)
37      W    = fm.ones_like(Tcal)
38      while not cv_atm(Tatm):
39          Tc    = fm.models.empca(Tcal-Tatm, W, n_components=50)
40          Tnc   = Tcal - Tc
41          Tatm_ = fm.models.atmoslines(Tnc)
```

```
42          W     = empca_weight(Tatm-Tatm_, Tnc-Tatm)
43          Tatm  = Tatm_
44
45      # modeling astronomical lines
46      Tast = fm.zeros_like(Tcal)
47      while not cv_ast(Tast):
48          Tc   = fm.models.pca(Tcal-Tatm-Tast, n_components=50)
49          Tnc  = Tcal - Tc
50          Tast = fm.models.astrolines(Tnc-Tatm)
51
52      # estimating FM gain
53      Tres = Tcal - Tatm - Tast
54      Pres = Gfm * ((Tres/Tamb)*Pr + (1-Tres/Tamb)*Poff)
55      Gfm  = fmgain(Pres, window_length=51, polyorder=3)
56
57  # make and plot a spectrum
58  Ta = Tcal - Tc - Tatm # Ta*
59  spec = fm.tospectrum(Ta) # K
60  freq = 1e-9 * spec.freq # GHz
61  plt.plot(freq, spec)
62  plt.show()
```

D
Photos

Here we show photos of Kohno laboratory members and coffee time members.
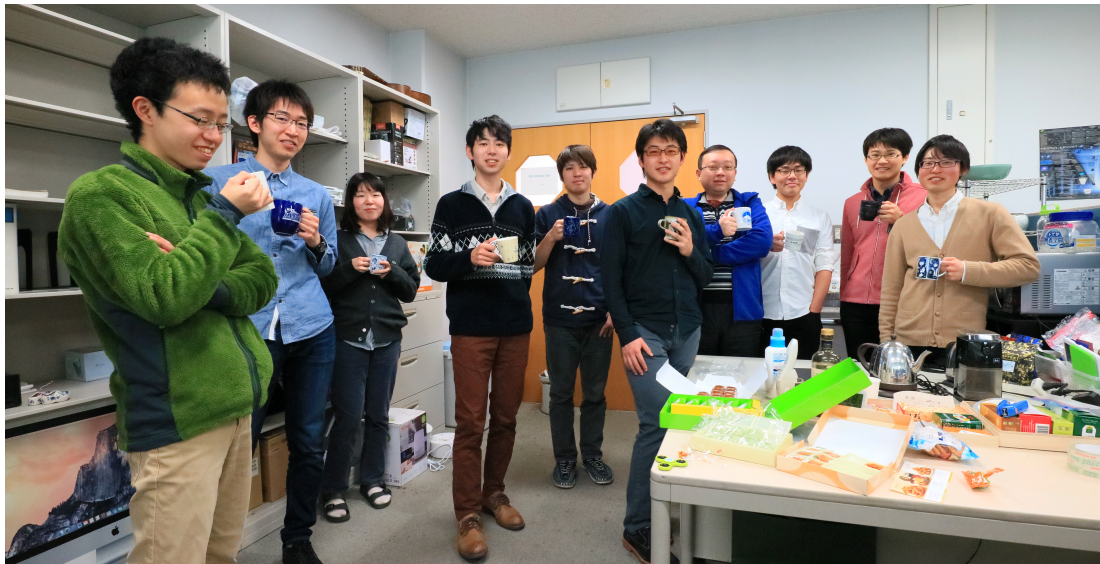

Figure D.1: Group photo of coffee time members in the Institute of Astronomy, the University of Tokyo taken on February 13th 2018.
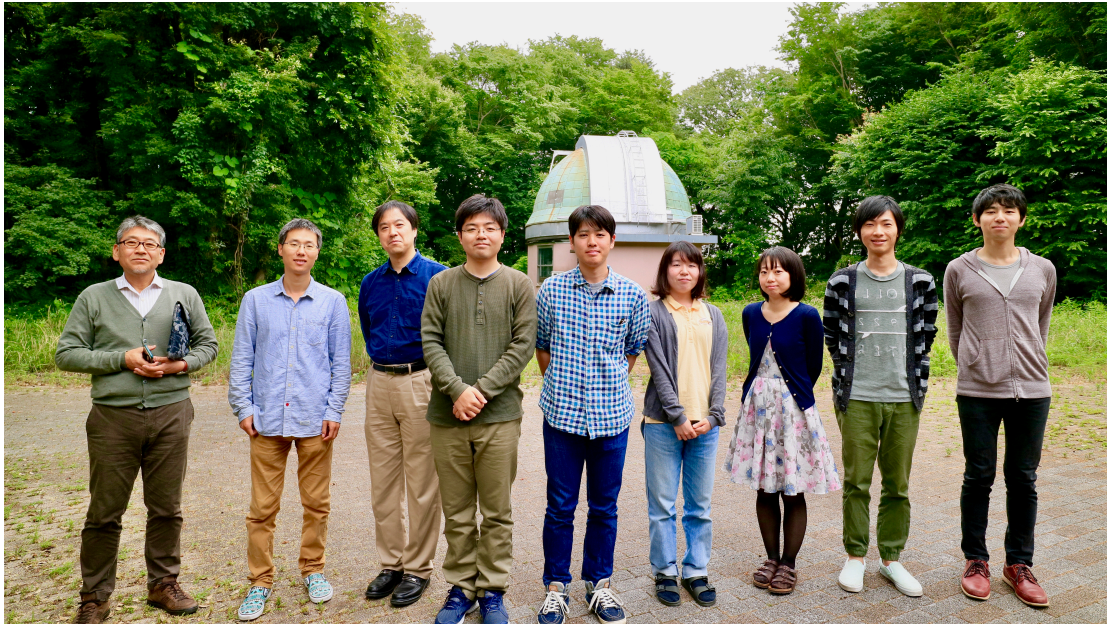
Figure D.2: Group photo of Kohno laboratory members taken on June 9th 2017.

Figure D.3: Group photo of Kohno laboratory members taken on February 18th 2018.

References

Bailey, S. (2012). Principal Component Analysis with Noisy and/or Missing Data. *Publications of the Astronomical Society of Pacific*, 124(9), 1015–.

Bishop, C. M. (2006). *Pattern Recognition and Machine Learning.* Springer.

Blain, A. W., Smail, I., Ivison, R., Kneib, J.-P., & Frayer, D. T. (2002). Submillimeter galaxies. *Physics Reports*, 369(2), 111 – 176.

Caux, E., Kahane, C., Castets, A., Coutens, A., Ceccarelli, C., Bacmann, A., Bisschop, S., Bottinelli, S., Comito, C., Helmich, F. P., Lefloch, B., Parise, B., Schilke, P., Tielens, A. G. G. M., van Dishoeck, E., Vastel, C., Wakelam, V., & Walters, A. (2011). TIMASSS: the IRAS 16293-2422 millimeter and submillimeter spectral survey. *Astronomy & Astrophysics*, 532, A23–41.

Cernicharo, J., Waters, L. B. F. M., Decin, L., Encrenaz, P., Tielens, A. G. G. M., Agúndez, M., De Beck, E., Müller, H. S. P., Goicoechea, J. R., Barlow, M. J., Benz, A., Crimier, N., Daniel, F., Di Giorgio, A. M., Fich, M., Gaier, T., García-Lario, P., de Koter, A., Khouri, T., Liseau, R., Lombaert, R., Erickson, N., Pardo, J. R., Pearson, J. C., Shipman, R., Sánchez Contreras, C., & Teyssier, D. (2010). A high-resolution line survey of IRC +10216 with Herschel/HIFI. *Astronomy & Astrophysics*, 521, L8–7.

Chapin, E. L., Berry, D. S., & Gibb, A. G. (2013). SCUBA-2: iterative mapmaking with the Sub-Millimetre User Reduction Facility. *Monthly Notices of ...*, 430(4), 2545–2573.

Emerson, D. T. & Graeve, R. (1988). The reduction of scanning noise in raster scanned data. *Astronomy and Astrophysics (ISSN 0004-6361)*, 190, 353–358.

Endo, A., vanÂ der Werf, P., Janssen, R. M. J., de Visser, P. J., Klapwijk, T. M., Baselmans, J. J. A., Ferrari, L., Baryshev, A. M., & Yates, S. J. C. (2012). Design of an integrated filterbank for deshima: On-chip submillimeter imaging spectrograph based on superconducting resonators. *Journal of Low Temperature Physics*, 167(3), 341–346.

Ezawa, H., Kawabe, R., Kohno, K., & Yamamoto, S. (2004). The Atacama Submillimeter Telescope Experiment (ASTE). In J. M. Oschmann, Jr. (Ed.), *Ground-based Telescopes*, volume 5489 of *SPIE Proceedings* (pp. 763–772).

Ezawa, H., Kohno, K., Kawabe, R., Yamamoto, S., Inoue, H., Iwashita, H., Matsuo, H., Okuda, T., Oshima, T., Sakai, T., Tanaka, K., Yamaguchi, N., Wilson, G. W., Yun, M. S., Aretxaga, I., Hughes, D., Austermann, J., Perera, T. A., Scott, K. S., Bronfman, L., & Cortes, J. R. (2008). New achievements of ASTE: the Atacama Submillimeter Telescope Experiment. In *Ground-based and Airborne Telescopes II*, volume 7012 of *SPIE Proceedings* (pp. 701208).

Heiles, C. (2007). A New Technique for Heterodyne Spectroscopy: Least-Squares Frequency Switching (LSFS). *The Publications of the Astronomical Society of the Pacific*, 119(8), 643–660.

Hunziker, S., Quanz, S. P., Amara, A., & Meyer, M. R. (2017). A PCA-based approach for subtracting thermal background emission in high-contrast imaging data.

Iguchi, S., Morita, K.-I., Sugimoto, M., Vilaró, B. V., Saito, M., Hasegawa, T., Kawabe, R., Tatematsu, K., Sakamoto, S., Kiuchi, H., Okumura, S. K., Kosugi, G., Inatani, J., Takakuwa, S., Iono, D., Kamazaki, T., Ogasawara, R., & Ishiguro, M. (2009). The Atacama Compact Array (ACA). *Publications of the Astronomical Society of Japan*, 61(1), 1–12.

Iono, D., Hatsukade, B., Kohno, K., Kawabe, R., Ikarashi, S., Ichikawa, K., Kodama, T., Motohara, K., Nakajima, T., Nakanishi, K., Ohta, K., Ota, K., Saito, T., Suzuki, K., Tadaki, K.-i., Tamura, Y., Ueda, J., Umehata, H., Yabe, K., Yoshida, T., Yuma, S., Kuno, N., Takano, S., Iwashita, H., Handa, K., Higuchi,

A., Hirota, A., Ishikawa, S., Kimura, K., Maekawa, J., Mikoshiba, H., Miyazawa, C., Miyazawa, K., Muraoka, K., Ogawa, H., Onodera, S., Saito, Y., Sakai, T., Takahashi, S., & Yun, M. S. (2012). Initial Results from Nobeyama Molecular Gas Observations of Distant Bright Galaxies. *Publications of the Astronomical Society of Japan*, 64.

Jolliffe, I. (2002). *Principal component analysis*. New York: Springer Verlag.

Jones, E., Oliphant, T., Peterson, P., et al. (2001–). SciPy: Open source scientific tools for Python. [Online; accessed <today>].

Kamazaki, T., Ezawa, H., XIV, K. T., Systems, & 2005 (2005). 2005ASPC..347..533K Page 533. *adsabs.harvard.edu*.

Kamazaki, T., Okumura, S. K., Chikada, Y., Okuda, T., Kurono, Y., Iguchi, S., Mitsuishi, S., Murakami, Y., Nishimura, N., Mita, H., & Sano, R. (2012). Digital Spectro-Correlator System for the Atacama Compact Array of the Atacama Large Millimeter/submillimeter Array. *Publications of the Astronomical Society of Japan*, 64(2), 29.

Klein, B., Hochgürtel, S., Krämer, I., Bell, A., Meyer, K., & Güsten, R. (2012). High-resolution wide-band fast Fourier transform spectrometers. *Astronomy & Astrophysics*, 542, L3.

Kovács, Attila (2008). CRUSH: fast and scalable data reduction for imaging arrays. *Millimeter and Submillimeter Detectors and Instrumentation for Astronomy IV. Edited by Duncan*, 7020, 70201S.

Lam, S. K., Pitrou, A., & Seibert, S. (2015). Numba: A llvm-based python jit compiler. In *Proceedings of the Second Workshop on the LLVM Compiler Infrastructure in HPC*, LLVM '15 (pp. 7:1–7:6). New York, NY, USA: ACM.

Laurent, G. T., Aguirre, J. E., Glenn, J., Ade, P. A. R., Bock, J. J., Edgington, S. F., Goldin, A., Golwala, S. R., Haig, D., Lange, A. E., Maloney, P. R., Mauskopf, P. D., Nguyen, H., Rossinot, P., Sayers, J., & Stover, P. (2005). The

Bolocam Lockman Hole Millimeter-Wave Galaxy Survey: Galaxy Candidates and Number Counts. *The Astrophysical Journal*, 623(2), 742–762.

Menten, K. M., Reid, M. J., Forbrich, J., & Brunthaler, A. (2007). The distance to the Orion Nebula. *Astronomy & Astrophysics*, 474(2), 515–520.

Minamidani, T., Nishimura, A., Miyamoto, Y., Kaneko, H., Iwashita, H., Miyazawa, C., Nishitani, H., Wada, T., Fujii, Y., Takahashi, T., Iizuka, Y., Ogawa, H., Kimura, K., Kozuki, Y., Hasegawa, Y., Matsuo, M., Fujita, S., Ohashi, S., Morokuma-Matsui, K., Maekawa, J., Muraoka, K., Nakajima, T., Umemoto, T., Sorai, K., Nakamura, F., Kuno, N., & Saito, M. (2016). Development of the new multi-beam 100 GHz band SIS receiver FOREST for the Nobeyama 45-m Telescope. In W. S. Holland & J. Zmuidzinas (Eds.), *SPIE Astronomical Telescopes + Instrumentation* (pp. 99141Z–10).: SPIE.

Minka, T. P. (2001). Automatic choice of dimensionality for PCA. *Advances in neural information processing systems*.

Mizuno, I., Kameno, S., Kano, A., Kuroo, M., Nakamura, F., Kawaguchi, N., Shibata, K. M., Kuji, S., & Kuno, N. (2014). Software Polarization Spectrometer "PolariS". *Journal of Astronomical Instrumentation*, 03(03n04), 1450010–16.

Morita, K. I., Nakai, M., Takahashi, T., Miyazawa, K., Ohishi, M., Tsutsumi, T., Takakuwa, S., Ohta, H., & Yanagisawa, K. (2003). COSMOS-3: The Third Generation Telescope Control Software System of Nobeyama Radio Observatory. *Astronomical Data Analysis Software and Systems XII ASP Conference Series*, 295, 166–.

Nakai, N., Tsuboi, M., & Fukui, Y. (2009). *Radio Astronomy.* Number 16 in Modern Astronomy Series. Nippon Hyoron Sha.

Nakajima, T., Kimura, K., Nishimura, A., Iwashita, H., Miyazawa, C., Sakai, T., Iono, D., Kohno, K., Kawabe, R., Kuno, N., Ogawa, H., Asayama, S., Tamura, T., & Noguchi, T. (2013). A New 100-GHz Band Two-Beam Sideband-Separating SIS Receiver for Z-Machine on the NRO 45-m Radio Telescope. *Publications of the Astronomical Society of the Pacific*, 125(925), 252–262.

Nishimura, Y., Watanabe, Y., Harada, N., Shimonishi, T., Sakai, N., Aikawa, Y., Kawamura, A., & Yamamoto, S. (2017). Molecular-cloud-scale Chemical Composition. II. Mapping Spectral Line Survey toward W3(OH) in the 3 mm Band. *The Astrophysical Journal*, 848(1), 0–0.

Paine, S. (2017). The am atmospheric model (v. 9.2).

Penzias, A. A., and, C. B. A. R. o. A., & 1973 (1973). Millimeter-wavelength radio-astronomy techniques. *annualreviews.org*.

Rossum, G. (1995). *Python Reference Manual*. Technical report, Amsterdam, The Netherlands, The Netherlands.

Roweis, S. (1998). Em algorithms for pca and spca. In *Proceedings of the 1997 Conference on Advances in Neural Information Processing Systems 10*, NIPS '97 (pp. 626–632). Cambridge, MA, USA: MIT Press.

Satou, N., Sekimoto, Y., Iizuka, Y., Ito, T., Shan, W.-L., Kamba, T., Kumagai, K., Kamikura, M., Tomimura, Y., Serizawa, Y., Asayama, S., & Sugimoto, M. (2008). A Submillimeter Cartridge-Type Receiver: ALMA Band 8 (385–500 GHz) Qualification Model. *Publications of the Astronomical Society of Japan*, 60(5), 1199–1207.

Savitzky, A. & Golay, M. J. E. (1964). Smoothing and differentiation of data by simplified least squares procedures. *Anal. Chem.*, 36, 1627–1639.

Sawada, T., Sawada, T., Ikeda, N., Ikeda, N., Sunada, K., Sunada, K., Kuno, N., Kamazaki, T., Morita, K.-I., Kurono, Y., Koura, N., Abe, K., Kawase, S., Maekawa, J., Horigome, O., & Yanagisawa, K. (2008). On-the-fly observing system of the nobeyama 45-m and aste 10-m telescopes. *Publications of the Astronomical Society of Japan*, 60(3), 445–455.

Scott, K. S., Austermann, J. E., Perera, T. A., Wilson, G. W., Aretxaga, I., Bock, J. J., Hughes, D. H., Kang, Y., Kim, S., Mauskopf, P. D., Sanders, D. B., Scoville, N., & Yun, M. S. (2008). AzTEC millimetre survey of the COSMOS

field – I. Data reduction and source catalogue. *Monthly Notices of …*, 385(4), 2225–2238.

Scott, K. S., Wilson, G. W., Aretxaga, I., Austermann, J. E., Chapin, E. L., Dunlop, J. S., Ezawa, H., Halpern, M., Hatsukade, B., Hughes, D. H., Kawabe, R., Kim, S., Kohno, K., Lowenthal, J. D., Montaña, A., Nakanishi, K., Oshima, T., Sanders, D., Scott, D., Scoville, N., Tamura, Y., Welch, D., Yun, M. S., & Zeballos, M. (2012). The source counts of submillimetre galaxies detected at $\lambda=$ 1.1 mm. *Monthly Notices of …*, 423(1), 575–589.

Shimajiri, Y., Kawabe, R., Takakuwa, S., Saito, M., Tsukagoshi, T., Momose, M., Ikeda, N., Akiyama, E., Austermann, J. E., Ezawa, H., Fukue, K., Hiramatsu, M., Hughes, D., Kitamura, Y., Kohno, K., Kurono, Y., Scott, K. S., Wilson, G. W., Yoshida, A., & Yun, M. S. (2011). New Panoramic View of 12CO and 1.1mm Continuum Emission in the Orion A Giant Molecular Cloud. I. Survey Overview and Possible External Triggers of Star Formation. *Publications of the Astronomical Society of Japan*, 63, 105–123.

Shimajiri, Y., Kitamura, Y., Saito, M., Momose, M., Nakamura, F., Dobashi, K., Shimoikura, T., Nishitani, H., Yamabi, A., Hara, C., Katakura, S., Tsukagoshi, T., Tanaka, T., & Kawabe, R. (2014). High abundance ratio of 13CO to C18O toward photon-dominated regions in the Orion-A giant molecular cloud. *Astronomy & Astrophysics*, 564, A68.

Shimajiri, Y., Sakai, T., Tsukagoshi, T., Kitamura, Y., Momose, M., Saito, M., Oshima, T., Kohno, K., & Kawabe, R. (2013). Extensive [C I] Mapping toward the Orion-A Giant Molecular Cloud. *The Astrophysical Journal Letters*, 774(2), L20.

Sorai, K., Sunada, K., Okumura, S. K., Tetsuro, I., Tanaka, A., Natori, K., & Onuki, H. (2000). Digital spectrometers for the Nobeyama 45-m telescope. *Proc. SPIE Vol. 4015*, 4015, 86–95.

Tamura, Y., Tatamitani, Y., Takahashi, S., Horigome, O., Maekawa, J., Kohno, K., Sakai, T., & Taniguchi, A. (2013). A New "Off-point-less" Method for

Mm/submm Spectroscopy with a Frequency-Modulating Local Oscillator. In *New Trends in Radio Astronomy in the ALMA Era: The 30th Anniversary of Nobeyama Radio Observatory. Proceedings of a Symposium held in Hakone* (pp. 401–).

Tipping, M. E. & Bishop, C. M. (1999). Probabilistic Principal Component Analysis. *Journal of the Royal Statistical Society: Series B (Statistical Methodology)*, 61(3), 611–622.

van der Walt, S., Colbert, S. C., & Varoquaux, G. (2011). The numpy array: A structure for efficient numerical computation. *Computing in Science & Engineering*, 13(2), 22–30.

Vieira, J. D., Marrone, D. P., Chapman, S. C., De Breuck, C., Hezaveh, Y. D., Weiβ, A., Aguirre, J. E., Aird, K. A., Aravena, M., Ashby, M. L. N., Bayliss, M., Benson, B. A., Biggs, A. D., Bleem, L. E., Bock, J. J., Bothwell, M., Bradford, C. M., Brodwin, M., Carlstrom, J. E., Chang, C. L., Crawford, T. M., Crites, A. T., de Haan, T., Dobbs, M. A., Fomalont, E. B., Fassnacht, C. D., George, E. M., Gladders, M. D., Gonzalez, A. H., Greve, T. R., Gullberg, B., Halverson, N. W., High, F. W., Holder, G. P., Holzapfel, W. L., Hoover, S., Hrubes, J. D., Hunter, T. R., Keisler, R., Lee, A. T., Leitch, E. M., Lueker, M., Luong-Van, D., Malkan, M., McIntyre, V., McMahon, J. J., Mehl, J., Menten, K. M., Meyer, S. S., Mocanu, L. M., Murphy, E. J., Natoli, T., Padin, S., Plagge, T., Reichardt, C. L., Rest, A., Ruel, J., Ruhl, J. E., Sharon, K., Schaffer, K. K., Shaw, L., Shirokoff, E., Spilker, J. S., Stalder, B., Staniszewski, Z., Stark, A. A., Story, K., Vanderlinde, K., Welikala, N., & Williamson, R. (2013). Dusty starburst galaxies in the early Universe as revealed by gravitational lensing. *Nature*, 495(7441), 344–347.

Wilson, T. L., Rohlfs, K., & Huttemeister, S. (2012). Tools of Radio Astronomy, 5th edition. *Tools of Radio Astronomy*.

Yamaki, H., Kameno, S., Beppu, H., Mizuno, I., & Imai, H. (2012). Optimization by Smoothed Bandpass Calibration in Radio Spectroscopy. *Publications of the Astronomical Society of Japan*, 64(5), 118.